FAST ANALYSIS AND DESIGN OF LARGE ANTENNA ARRAYS USING THE HYBRID MULTIPLE SWEEP METHOD OF MOMENTS/CONJUGATE GRADIENT WITH THE SPECTRAL ACCELERATION ALGORITHM

SUPAKIT KAWDUNGTA

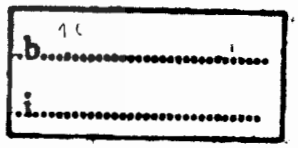

A THESIS SUBMITTED IN PARTIAL FULLFILLMENT
OF THE REQUIREMENT FOR THE DEGREE OF
DOCTOR OF ENGINEERING IN ELECTRICAL ENGINEERING
FACULTY OF ENGINEERING
KING MONGKUT'S INSTITUTE OF TECHNOLOGY LADKRABANG
2011

KMITL-2011-EN-D-018-131

หัวข้อวิทยานิพนธ์	การวิเคราะห์และออกแบบอย่างรวดเร็วของสายอากาศแถวลำดับขนาดใหญ่โดยวิธีร่วมระหว่างวิธีโมเมนต์แบบการกวาดหลายครั้งและเกรเดียนต์สังยุคด้วยกระบวนการเร่งแบบสเปกตรัม
นักศึกษา	นายศุภกิต แก้วดวงตา
รหัสประจำตัว	51060021
ปริญญา	วิศวกรรมศาสตรดุษฎีบัณฑิต
สาขาวิชา	วิศวกรรมไฟฟ้า
พ.ศ.	2554
อาจารย์ที่ปรึกษาวิทยานิพนธ์	รศ. ดร. ชูวงค์ พงศ์เจริญพาณิชย์
อาจารย์ที่ปรึกษาวิทยานิพนธ์ร่วม	รศ. ดร. ดนัย ต.รุ่งเรือง

บทคัดย่อ

วิทยานิพนธ์ฉบับนี้เป็นการนำเสนอการวิเคราะห์และออกแบบอย่างรวดเร็วของสายอากาศแบบแถวลำดับขนาดใหญ่โดยใช้กระบวนการเร่งแบบสเปกตรัม โดยเริ่มจากการพัฒนาวิธีโมเมนต์แบบการกวาดหลายครั้งด้วยวิธีการกวาดแบบฟันเลื่อยเพื่อใช้ในการคำนวณสายอากาศแถวลำดับที่วางตัวแบบระนาบ ซึ่งจะช่วยลดเวลาในการคำนวณและการใช้หน่วยความจำให้น้อยลง จากนั้นได้ทำการปรับปรุงวิธีการดังกล่าวด้วยวิธีการทำงานร่วมกันระหว่างวิธีโมเมนต์แบบการกวาดหลายครั้งและวิธีเกรเดียนต์สังยุคเพื่อให้สามารถลู่เข้าหาคำตอบที่ถูกต้องได้อย่างรวดเร็วยิ่งขึ้น การทำงานดังกล่าวนั้นจะมีลักษณะคือ จะใช้คำตอบของวิธีโมเมนต์แบบการกวาดหลายครั้งมาเป็นค่าเริ่มต้นของวิธีเกรเดียนต์สังยุคซึ่งจะสามารถทำให้วิธีเกรเดียนต์สังยุคลู่เข้าหาคำตอบที่ถูกต้องได้อย่างรวดเร็วเนื่องจากวิธีโมเมนต์แบบการกวาดหลายครั้งนั้นเป็นวิธีการที่ซึ่งรวมเอากลไกการกระจัดกระจายคลื่นและการสะท้อนคลื่นเอาไว้ในวิธีการคำนวณดังกล่าว แต่อย่างไรก็ตามวิธีการดังกล่าวยังคงเป็นลำดับ N^2 เมื่อ N คือจำนวนของตัวแปรที่ไม่ทราบค่าของวิธีโมเมนต์ จึงได้นำกระบวนการเร่งแบบสเปกตรัมเข้ามาเพื่อช่วยลดความซับซ้อนในการคำนวณให้ลดลงเหลือลำดับ N ซึ่งวิธีการนี้จะทำการแบ่งพื้นที่การคำนวณออกเป็นสองส่วนคือส่วนที่มีการเชื่อมต่อมาก และส่วนที่มีการเชื่อมต่อน้อย โดยส่วนพื้นที่ที่มีการเชื่อมต่อมากนั้นจะคำนวณด้วยวิธีการคูณเวกเตอร์เมตริกซ์มาตรฐานและในส่วนพื้นที่ที่มีการเชื่อมต่อน้อยนั้นจะคำนวณด้วยวิธีการเร่งแบบสเปกตรัม จากนั้นได้ทำการศึกษาค่าพารามิเตอร์ของกระบวนการเร่งแบบสเปกตรัมเพื่อทำการปรับค่าพารามิเตอร์การอินทิเกรตให้เหมาะสมกับการคำนวณในแต่ละกรณีด้วยกระบวนการคิดแบบสืบทอดพันธุกรรม จากผลที่ได้พบว่าวิธีการดังกล่าวสามารถที่จะใช้ในการวิเคราะห์สายอากาศแถวลำดับขนาดใหญ่ได้อย่างมีประสิทธิภาพ จึงได้นำวิธีการดังกล่าวมาใช้ในการออกแบบสายอากาศแบบแถวลำดับอย่างอัตโนมัติร่วมกับกระบวนการคิดแบบการสืบทอดพันธุกรรม

Thesis Title	Fast Analysis and Design of Large Antenna Arrays Using the Hybrid Multiple Sweep Method of Moments/Conjugate Gradient with the Spectral Acceleration Algorithm
Student	Mr. Supakit Kawdungta
Student ID.	51060021
Degree	Doctor of Engineering
Program	Electrical Engineering
Year	2011
Thesis Advisor	Assoc.Prof.Dr. Chuwong Phongcharoenpanich
Thesis Co-advisor	Assoc.Prof.Dr. Danai Torrungrueng

ABSTRACT

This thesis presents the analysis and design of large antenna arrays by using the spectral acceleration (SA) algorithm. The multiple sweep method of moments (MSMM) is first developed by the sawtooth sweep to analyze the planar array. It requires less computational time and memory than the conventional MSMM. To reduce the computational time of the MSMM for solving electrically large electromagnetic (EM) problems, an appropriate combination of the MSMM and conjugate gradient (CG) method is newly proposed resulting in faster convergence rate, called hybrid MSMM/CG method. The hybrid MSMM/CG method starts with the MSMM and then is switched to the CG method when the preliminary solution satisfies the first convergence test, which is a preliminary test. One may also think that the MSMM is employed as a good initial guess for the CG method resulting in faster convergence rate since the first few MSMM sweeps include dominant and higher order radiation/scattering mechanisms as pointed out earlier. However, it is an $O(N^2)$, when N is an the total number of unknown. The SA algorithm is proposed to incorporate into the hybrid MSMM/CG method for $O(N)$. In the SA algorithm, the contributions to a receiving element on the antenna arrays are separated into strong and weak source contributions. The former is calculated by the standard matrix vector multiplication, while the latter is computed by using the SA algorithm involving the spectral domain representation of the 3D scalar free-space Green's function. It is found that this technique is efficient to analyze a large antenna array. In addition, the proposed method is employed to automatic design the antenna array with the genetic algorithm (GA). It can be efficiently applied to the antenna arrays in free space.

ACKNOWLEDGEMENTS

This thesis is the final submission to accomplish the Doctor of Engineering of Electrical Engineering at King Mongkut's Institute of Technology Ladkrabang. This work has been supported by the Commission on Higher Education (CHE) in Thailand and the Thailand Research Fund (TRF) through the Royal Golden Jubilee Ph.D. Program under Grant no. PHD/0226/2550. During the time I have been working on my thesis, I have been received good support, assistance and encouragement from many people as below. Therefore, I would like to take this opportunity to express my sincere thanks to those who have contributed directly or indirectly to bring this thesis to the final format.

I would like to express my grateful to my advisor, Assoc. Prof. Dr. Chuwong Phongcharoenpanich, who has always given me for a long-term suggestion. I am especially thankful for the various opportunities that he gave to me including his guidance and kind support. In addition, I would like to express my grateful to Assoc. Prof. Dr. Danai Torrungrueng my co-advisor for his kind discussions, along term suggestion and proof reading of my thesis.

Furthermore, I would like to extend my thankful to Prof. Joel T. Johnson at the Ohio State University to give a good research experience in the area of computational electromagnetics to achieve new performance goals for me in doing my thesis.

Moreover, I would love to thank to all alumnae and present members in Wireless Communication Laboratory for their helpful discussions and friendship. I would love to express my thanks to especially Dr. Suthasinee Lamultree and Mr. Sitthichai Dentri for their helpful discussions.

For my parents including all members in my family (also, my dear grandma who see me in my dream), most importantly, I would never be who I am and what I am without them. I am proud to give a credit to them who are totally the main reason to drive me to be at this point. I would love to express my gratefulness and appreciation to all of them for their support, encouragement, stimulation and enthusiasm.

Finally, it is my wish that this thesis will be a valuable source of data for those who are interested in this field.

Supakit Kawdungta

TABLE OF CONTENTS

TABLE OF CONTENTS (CONTINUE)

TABLE OF CONTENTS (CONTINUE)

TABLE OF CONTENTS (CONTINUE)

LIST OF TABLES

LIST OF FIGURES

LIST OF FIGURES (CONTINUE)

LIST OF FIGURES (CONTINUE)

LIST OF FIGURES (CONTINUE)

LIST OF FIGURES (CONTINUE)

LIST OF FIGURES (CONTINUE)

LIST OF FIGURES (CONTINUE)

LIST OF FIGURES (CONTINUE)

LIST OF ABBREVIATIONS

BBFB	:	Buffer Block Forward/Backward
BFB	:	Block Forward/Backward
BiCG	:	Bi-Conjugate Gradient
BiCGstab	:	Bi-Conjugate Gradient Stabilize
CFIE	:	Combined Field Integral Equation
CG	:	Conjugate Gradient
DFT	:	Discrete Fourier Transform
EFIE	:	Electrical Field Integral Equation
EM	:	Electromagnetic
FB	:	Forward/Backward
FDTD	:	Finite Difference Time Domain
FEM	:	Finite Element Method
FFT	:	Fast Fourier Transform
FMM	:	Fast Multipole Method
FIT	:	Finite Integration Technique
GA	:	Genetic Algorithm
GFB	:	Generalized Forward/Backward
IE	:	Integral Equation
MFIE	:	Magnetic Field Integral Equation
MLFMM	:	Multilevel Fast Multipole Method
MM	:	Method of Moments
MOMI	:	Method of Order Multiple Interaction
MSMM	:	Multiple Sweep Method of Moments
NEC	:	Numerical Electromagnetic Code
NSA	:	Novel Spectral Acceleration
PO	:	Physical Optics
PEC	:	Perfect Electric Conductor
PWL	:	Piecewise Linear

LIST OF ABBREVIATIONS (CONTINUE)

PWS	:	Piecewise Sinusoid
RCS	:	Radar Cross Section
RMS	:	Root Mean Square
RSS	:	Rough Surface Scattering
SA	:	Spectral Acceleration
SLL	:	Side Lobe Level
SIM	:	Sparse Iterative Method
TEM	:	Transverse Electromagnetic Mode
UTD	:	Uniform Theory of Diffraction

CHAPTER 1
INTRODUCTION

In this chapter, the background of electrically large problem in electromagnetic (EM) problem is remarked and the motivation of problem also shown in Section 1.1. Section 1.2 discusses about the literature reviews of interesting methods. The objective and the scope of the thesis are shown in Section 1.3. Finally, organization of this thesis is discussed in detail in Section 1.4.

1.1 Background and Motivation

In EM analysis, dimension of the objects are considered by comparing with the wavelength of the operating frequency. There are several applications, considered as electrically large problems such as the rough-surface-scattering (RSS) problem. The RSS has played an important role in many EM applications; e.g., remote sensing, wave propagation, radio astronomy and radar system design. For example, the radio communication over the ocean is affected by the surface roughness due to rapidly fluctuating reflection from the ocean surface. In addition, the analysis of radar cross section (RCS) is practically dealed with large structures; e.g., an aircraft or a ship. The analysis of antennas attached on these structures and large antenna array are also considered as electrically large structures. Figure 1.1 shows examples of electrically large EM radiation/scattering problems. The RSS of the 3D ship-like target on a rough sea surface illuminated by an incident EM plane wave is shown in Fig. 1.1 (a) [1]. It is considered as the elongate problem. Figure 1.1 (b) also shows the structure of the aircraft and the ship, which they are considered as the RCS problem [2]. In addition, the real application of the antenna array is illustrated in Fig. 1.1 (c). It is the dipole antenna array [3].

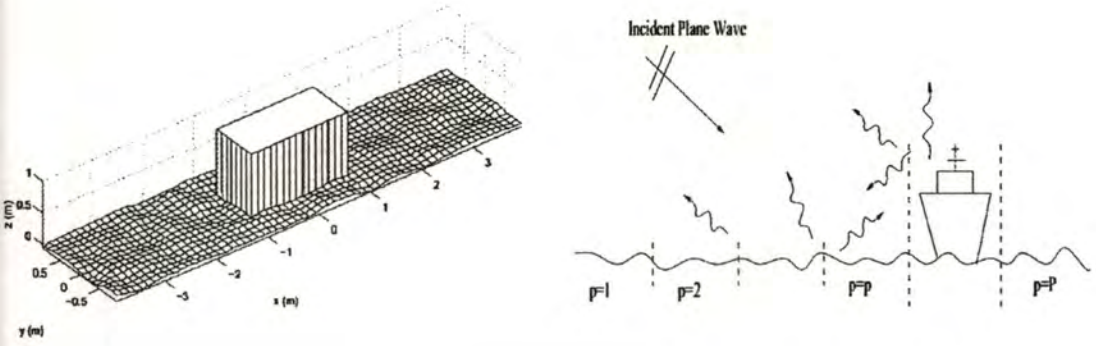

(a)

(b)

(c)

Figure 1.1 Examples of electrically large EM radiation/scattering problems [1]-[3]. (a) RSS applications, (b) RCS applications, and (c) Antenna array applications.

The fast analysis of large EM radiation/scattering problems has been fascinating to research in the past several years due to their highly flexible applications. The problems of dealing with electrically large EM problems are more computational complexity, less computational accuracy, and considerable memory requirements. With the recent growth in computer technology and the development of fast algorithms, they

are used to reduce the computational complexity and memory requirements for solving electrically large structures. However, the development of fast algorithms still continues to accelerate computational times and save computer resources. In the next section, several methods are reviewed.

1.2 Literature Review

In the EM analysis, several methods can be employed to solve practical EM problems such as the physical optics (PO) method, the transmission-line modeling method, the uniform theory of diffraction (UTD) method, the integral equation (IE) method, the finite difference time domain (FDTD) method, the finite element method (FEM), and the finite integration technique (FIT). In this thesis, the IE method with the method of moments (MM) is employed. The MM casts the solution for the induced current in the form of an integral equation, where the unknown current density is a part of the integrand. Usually, the electric field, magnetic field and combined field integral equations (EFIE, MFIE and CFIE) have been used extensively in solving EM problems [4]-[5]. The MM is one of the most popular computational techniques to solve relevant integral equations associated with EM problems, which is a class of high accuracy technique. The MM forms the linear equation and solves an $N \times N$ impedance matrix by using the direct or iterative methods depending on its applications, where N is the total number of unknowns of interest [5].

The solution of linear equations can be classified into two types; i.e., direct and iterative solutions. The direct method is easy to implement and analyze, where its common characteristic is that the original linear equations are transformed into equivalent equations that can be solved more easily; i.e., LU decomposition, Gaussian elimination and Gauss-Jordan elimination [5]-[8]. Note that the direct method requires $O(N^3)$ for computational time and $O(N^2)$ for memory storage. However, theoretical studies find that of the direct method usually has problem with the effect of round-off error for the large linear equation, and a large number of arithmetic manipulations must be used. Thus, this method is not practical in solving large systems of equations. In contrast, iterative methods can rectify the problem of round-off error and more suitable for large problems [7].

Iterative methods can be categorized into stationary and non-stationary methods, which are popular for a large system of linear equations. Over the past several years, several stationary and non-stationary iterative methods have been applied to improve the computational efficiency of the MM and for large EM problems. The stationary iterative method provides fast convergence, and is simple to implement and analyze. However, its convergence rate is limited by a class of matrices. For the stationary method, C. T. Tai proposed the Gauss-Seidel method to solve the linear equation of EM scattering problems, which converges rapidly [8]. One well-known method for large problems is the forward/backward (FB) method, where it is an $O(N^2)$ CPU times and memory storage. It was first proposed by D. Hollyday *et al.* [9]-[10] and has been proposed with many EM problems in the past several years. For example, A. Iodice proposed the FB method for scattering from dielectric rough surfaces, which is very rapidly converged for moderately rough soil and sea surfaces [11]. In addition, C. S. Heng and D. Torrungrueng also proposed the FB method for capacitance extraction problems of planar structures, which provides accurate results compared with the standard MM with less computational times for relatively large problems [12]. Moreover, the FB method has been developed by the technique of block stationary iterative solver, called the block forward/backward (BFB) method. This method was proposed by B. Babu *et al.* for scattering problems from inhomogeneous bodies [13]. However, this method is also improved to the buffer block forward/backward (BBFB) method to circumvent the poor convergence of the FB and BFB methods [14]. Nevertheless, the FB method becomes unstable when some obstacles, like ships or large breaking waves, are included in the original problem. It is also required monotonic variation on array surface in order to step up an FB procedure. Thus, the generalized forward/backward (GFB) method was proposed to overcome these problems [15]-[16]. Other methods were also proposed as the stationary iterative method; i.e., the Method of Ordered Multiple Interactions (MOMI) and the Multiple Sweep Method of Moments (MSMM). The MOMI was originally developed as an iterative method for solving the MFIE encountered in scattering from extended perfect electric conductor (PEC) rough surface in one dimension [17]-[19]. The convergence properties of the MOMI series for this problem were found to be excellent [18]-[19]. The MSMM was proposed by D. Torrungrueng in 1996 for analysis of electrical large bodies [22]. The

MSMM was also presented by D. Colak *et al.* for the analysis of the 3D radiation and scattering from electrically large, perfectly conducting bodies, which provides fast convergence rate [1], [20], [22]-[24].

For the non-stationary methods, they are rather complicated to implement and highly effective, but they based on sequential orthogonal vectors that mainly depend on the iteration coefficients. One of the well-known non-stationary methods is the conjugate gradient (CG) method, which is a highly efficient method for symmetrical positive definite systems [25]-[30]. The method proceeds by generating vector sequences of iterated residuals corresponding to the iteration, and the search directions used in updating the iterations and residuals. The CG method has been proposed for the analysis of the radiation/scattering problem [25]. It shows a good convergence, but its convergence route is very fluctuation. This method requires two inner products to compute for each iteration. Moreover, the Bi-Conjugate Gradient (BiCG) is developed from the CG method by adding one of the orthogonal vectors [31], and the BiCG is improved to the Bi-Conjugate Gradient Stabilize (BiCGstab) to solve non-symmetrical matrix equations [32].

However, the computational time of iterative methods varies according to the number of iterations. It is necessary to reduce the number of iterations for solving very large unknown N without sacrificing accuracy. One way to improve the convergence rate of iterative methods is the combination method presented by A. R. Clark *at el.* as the hybrid iterative method. The method is to employ combines between the Sparse Iterative Method (SIM) and BiCGstab methods. It shows faster than the original method with rapid convergence rate [33]-[35].

These methods present very fast convergence rate, which they provide accurate results within a few iterations. Nevertheless, they are $O(N^2)$ computational requirements. Thus, they can be mandatory to incorporate fast techniques into them to improve the overall efficiency. To reduce computation complexity of iterative method, it is the speed up of matrix vector multiplication by acceleration techniques. Many of the acceleration techniques have been presented in the past such as the Fast Multipole Method (FMM) [36]-[41], the Multilevel Fast Multipole Method (MLFMM) [42]-[45], the Fast Fourier Transform (FFT) [46]-[49], the Discrete Fourier Transform (DFT) [50] and the Spectral

Acceleration (SA) algorithm [51]-[60]. The FMM was presented in 1980s. It has been proved to be a very powerful and efficient scheme for accelerating iterative solutions for integral equations [36]-[38]. It has been employed with the MM, which can reduce the computational complexity of iterative methods from $O(N^2)$ to $O(N^{1.5})$ [36]-[41]. Moreover, it is also improved to be the MLFMM, which reduces the computational complexity to $O(N \log N)$ [42]-[45]. In addition, the FFT and DFT were proposed to reduce the computational complexity to $O(N)$. They have been cooperated with many methods, i.e., FB/DFT, MM/DFT, BiCGstab/FFT and CG/FFT to solve radiation/scattering EM problems [46]-[50]. However, they cannot be employed with non-periodic structures. The SA algorithm is also applied to reduce the computational time of the matrix vector multiplication without sacrificing accuracy. In the SA algorithm, the contributions to a receiving element on large problems are separated into strong and weak source contributions. The former is performed by the standard matrix vector, while the latter is computed using the SA algorithm involving the spectral representation of the free space Green's function. Several numerical results were proposed to show the accuracy and efficiency of the SA algorithm such as the FB/NSA and GFB/NSA [51]-[60]. It shows $O(N)$ in the computational time per iteration, and its memory requirement for very large problems tends to be $O(N)$. In addition, the SA algorithm can be employed with non-periodic structures.

1.3 Objective and the Scope of the Thesis

In the analysis of electrically large EM problems, the considerable amount of computational time and memory are usually required, especially for the MM. In this thesis, the improvement of the MM will be studied by using a hybrid method and an acceleration technique. The objectives and the scope of the thesis are given as follows:

1. To analyze EM problems using the MM.
2. To improve the performance of the MSMM with the sawtooth sweep used to analyze the planar dipole antenna array.
3. To enhance the performance of the MSMM by using an appropriate combination with the CG method for the faster convergence rate.

4. To study the SA algorithm by using the genetic algorithm (GA) optimization to determine the optimum SA integration parameters.
5. To enhance the performance of the hybrid MSMM/CG method by integrating with the SA algorithm to be O(N).
6. To apply the hybrid MSMM/CG/SA method with large dipole antenna arrays.

1.4 Organization of This Thesis

In this thesis, the efficient hybrid method is proposed. The hybrid method appropriately combines the MSMM and the CG method, called the hybrid MSMM/CG method, yielding better convergence rate. Subsequently, the SA algorithm is incorporated with the hybrid MSMM/CG method to improve its efficiency to be $O(N)$ for both computational time and memory requirement. Moreover, uniform and non-uniform dipole antenna arrays are considered as examples.

The remaining portion of this thesis consists of five chapters. They are involving theories and applications of the IE, MM, MSMM, hybrid MSMM/CG methods and the SA algorithm. They are employed for the computation of large dipole antenna arrays.

In Chapter 2, the fundamentals of the IE and the MM are reviewed. The theoretical and numerical study of the MSMM is also discussed. In addition, the improvement of the MSMM by using the sawtooth sweep is presented to analyze the uniform and non-uniform planar dipole antenna arrays. Numerical results are also illustrated the efficiency of the improved MSMM in this chapter.

Chapter 3 presents the hybrid MSMM/CG method to achieve the convergence rate benefits. The hybrid method is employed to analyze both collinear and planar dipole antenna arrays. Numerical results illustrate that the hybrid MSMM/CG method converges faster with good accuracy compared with the MM.

Chapter 4 presents the theory of the SA algorithm and its formulation. The SA's procedure is elucidated with the flow chart. The effects of the SA parameters to accuracy and computational time are shown. In addition, the SA integration parameters are optimized using the GA optimization. With these optimized SA integration parameters, the SA algorithm will be integrated into the hybrid MSMM/CG method to achieve $O(N)$ computational complexity. The implementation of the SA algorithm is also presented for

dipole antenna arrays. Numerical results illustrate the efficiency of the SA algorithm with the optimum SA integration parameters in this chapter.

Chapter 5 shows the MSMM/SA/GA method to automatically design collinear dipole antenna arrays. The non-uniform spacing collinear dipole antenna arrays are considered for minimum side lobe level (SLL). The design procedure of the MSMM/SA/GA method is discussed, and numerical results illustrate its efficiency. It shows very efficient for non-uniform collinear dipole antenna arrays. The conclusions and remarks for future studies are included in Chapter 6.

In the Appendix A, the genetic algorithm (GA) basic theory is discussed, which the procedure of each operator is shown. Moreover, the principle of the pattern multiplication is shown in Appendix B.

CHAPTER 2
DEVELOPMENT OF THE MULTIPLE SWEEP METHOD OF MOMENTS (MSMM)

2.1 Introduction

In this chapter, the IE of the dipole antenna array is discussed, and the MM technique is used to form the linear equation, where it is solved by using two iterative methods; i.e., the MSMM and the CG method. In addition, collinear and planar dipole antenna arrays are solved by using these iterative methods. Section 2.2 presents the basic theory of the IE, and the MM technique is also mentioned in Section 2.3. The MSMM is discussed in detail for collinear and planar dipole antenna arrays in Section 2.4. Moreover, the new MSMM sweeping procedure is presented, called the sawtooth sweep, in Section 2.4. Numerical results are illustrated in Section 2.5, providing faster convergence rate with good accuracy. Finally, conclusions are addressed in Section 2.6.

2.2 Integral Equation (IE)

There are many forms of IEs. Three popular IEs for time harmonics EM are the EFIE, the MFIE and the CFIE. The EFIE enforces the boundary condition on the tangential electric field, the MFIE enforces the boundary condition on the tangential components of the magnetic field, and the CFIE is a well-known linear combination of the EFIE and the MFIE. In this section, only the EFIE will be discussed as it is applied to perfect electric conductor (PEC) wire structures [4].

2.2.1 Electric Field Integral Equation (EFIE)

The EFIE is a statement of the boundary condition that the total tangential electric field on a PEC surface of an antenna/scatterer is vanished as follows [4]

$$\overline{E}_t^t(\overline{r}=\overline{r}_s)=\overline{E}_t^i(\overline{r}=\overline{r}_s)+\overline{E}_t^s(\overline{r}=\overline{r}_s)=0 \qquad \text{on } S, \tag{2.1}$$

or

$$\bar{E}_t^s(\bar{r}=\bar{r}_s) = -\bar{E}_t^i(\bar{r}=\bar{r}_s) \qquad \text{on } S, \tag{2.2}$$

where $\bar{E}_t^t$ is the total tangential component of electric field, $\bar{E}_t^i$ is the tangential component of the incident electric field, $\bar{E}_t^s$ is the tangential component of the scattered electric field, S is the surface of the antenna/scatterer, and $\bar{r}=\bar{r}_s$ is the position vector from the origin to any point on the surface of the antenna/scatterer. When the incident electric field impinges on the surface (S) of the antenna/scatterer, the incident electric field induces on the surface and becomes the electric current density ($\bar{J}_s$). If the $\bar{J}_s$ is known, the scattered electric field at any point due to $\bar{J}_s$ can be determined as

$$\bar{E}^s(r) = -j\omega\bar{A} - j\frac{1}{\omega\mu\varepsilon}\nabla(\nabla\cdot\bar{A}) = -j\frac{1}{\omega\mu\varepsilon}\left[\omega^2\mu\varepsilon\bar{A} + \nabla(\nabla\cdot\bar{A})\right], \tag{2.3}$$

where the magnetic vector potential ($\bar{A}$) is

$$\bar{A}(\bar{r}) = \mu\iint_S \bar{J}_s(\bar{r}')\frac{e^{-jkR}}{4\pi R}ds'. \tag{2.4}$$

(2.3) and (2.4) can also be expressed as

$$\bar{E}^s(\bar{r}) = -j\frac{\eta}{k}\left[k^2\iint_S \bar{J}_s(\bar{r}')G(\bar{r},\bar{r}')ds' + \nabla\iint_S \nabla'\cdot\bar{J}_s(\bar{r}')G(\bar{r},\bar{r}')ds'\right], \tag{2.5}$$

where

$$G(\bar{r},\bar{r}') = \frac{e^{-jkR}}{4\pi R}, \tag{2.6}$$

$$R = |\bar{r}-\bar{r}'| = \sqrt{(x-x')^2+(y-y')^2+(z-z')^2} \tag{2.7}$$

In (2.5), ∇ and ∇' are the gradients with respect to the observation (unprimed) and source (primed) coordinates respectively, and $G(\bar{r},\bar{r}')$ represents the three-dimensional (3D) scalar Green's function in free space. Note that, R in (2.7) is the distance between an observation point ($\bar{r}$) and a source point ($\bar{r}'$), η is the impedance of free space, k is the wave number of medium, ω is the angular frequency, μ is the permeability of medium, and ε is the permittivity of medium. Because the left side of (2.5) can be expressed in terms of the known incident electric field using (2.2), it is referred to as the EFIE. It can be used to find $\bar{J}_s(\bar{r}')$ at any point of $\bar{r}=\bar{r}'$ on the antenna/scatterer. Figure 2.1 shows the coordinate system for computing radiation fields.

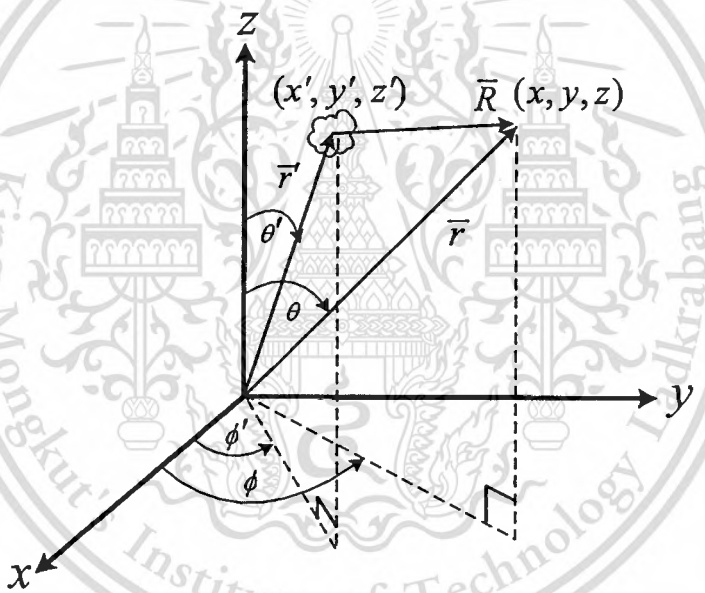

Figure 2.1 Coordinate system for computing radiation fields.

2.2.2 Pocklington's Integral Equation

The classic 3D integral equation, referred to as the Pocklington's integrodifferential equation [4], is described. It can be used most conveniently to find the current distribution on conducting wires. The Pocklington's integral equation is more general, and it is adaptable to many types of feeding sources such as a delta gap and a magnetic frill excitations [4].

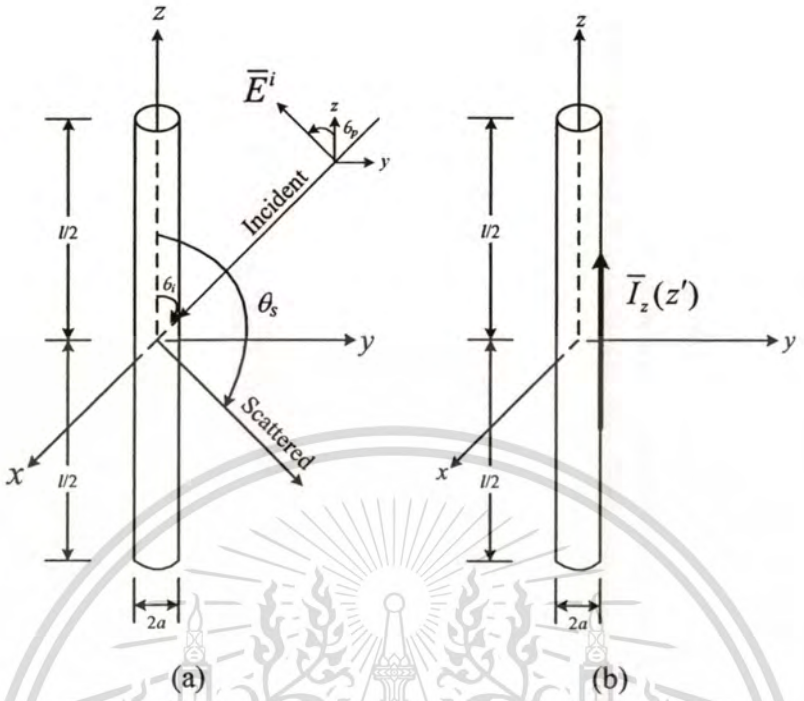

Figure 2.2 Incident field on the conducting wire [4]. (a) Uniform plane wave obliquely incidents on a conducting wire and (b) Equivalent current on a conducting wire.

Let consider on EM scattering problem of a conducting wire. Figure 2.2 assumes that the incident plane wave impinges on the surface of a conducting wire with radius a and length l. The total tangential electric field ($\overline{E}_z^t$) at the surface of the wire is given as in (2.1) and (2.2). The scattered field by the induced current density on the surface of the wire can be computed using (2.3). In this case, the conducting wire is along the z axis, and the observation points are on the wire surface. Thus, only the z component of (2.3) is considered, which can be reduced to

$$\overline{E}_z^s(\overline{r}) = -j\frac{1}{\omega\mu\varepsilon}\left(k^2\overline{A}_z(\overline{r}) + \frac{\partial^2\overline{A}_z(\overline{r})}{\partial z^2}\right). \tag{2.8}$$

According to (2.4) with neglecting edge effects, it becomes

$$\bar{A}_z(\bar{r}) = \frac{\mu}{4\pi}\iint_s \bar{J}_z(\bar{r}')\frac{e^{-jkR}}{R}ds' = \frac{\mu}{4\pi}\int_{-l/2}^{l/2}\int_0^{2\pi}\bar{J}_z(\bar{r}')\frac{e^{-jkR}}{R}ad\phi' dz'. \tag{2.9}$$

When the very thin wire is considered. The current density ($\bar{J}_z(\bar{r}')$) is not a function of the azimuthal angle (ϕ) [4]-[6], and it can be represented as

$$\bar{J}_z(\bar{r}') = \frac{1}{2\pi a}\bar{I}_z(z'), \tag{2.10}$$

where $\bar{I}_z(z')$ represents the equivalent filament line source current located a radial distance from the z axis as shown in Fig. 2.2(b). Thus (2.9) reduces to

$$\bar{A}_z(\bar{r}) = \frac{\mu}{4\pi}\int_{-l/2}^{l/2}\left(\frac{1}{2\pi a}\int_0^{2\pi}\bar{I}_z(z')\frac{e^{-jkR}}{R}ad\phi'\right)dz', \tag{2.11}$$

where

$$R = \sqrt{(x-x')^2 + (y-y')^2 + (z-z')^2}. \tag{2.12}$$

Note that R in (2.12) can be rewritten in the cylindrical coordinate as

$$R = \sqrt{\rho^2 + a^2 - 2\rho a\cos(\phi-\phi') + (z-z')^2}, \tag{2.13}$$

where ρ is the radial distance to the observation point, ϕ is the azimuth angle of the observation point, ϕ' is the azimuth angle of the source point, and a is the radius of conducting wire. Because of the symmetry of the scatterer, the observers are not a function of ϕ. For observations at the surface $\rho = a$ of the scatterer, (2.11) reduces to

$$\bar{A}_z(\rho = a) = \mu\int_{-l/2}^{l/2}\bar{I}_z(z')\left(\frac{1}{2\pi}\int_0^{2\pi}\frac{e^{-jkR}}{4\pi R}d\phi'\right)dz' = \mu\int_{-l/2}^{l/2}\bar{I}_z(z')G(z,z')dz', \tag{2.14}$$

where

$$G(z,z') = \frac{1}{2\pi}\int_0^{2\pi} \frac{e^{-jkR}}{4\pi R} d\phi'. \tag{2.15}$$

Substituting (2.14) into (2.8), the z component of the scattered electric field can be expressed as

$$\bar{E}_z^s(\rho = a) = -j\frac{1}{\omega\varepsilon}\left(k^2 + \frac{\partial^2}{\partial z^2}\right)\int_{-l/2}^{l/2} \bar{I}_z(z')G(z,z')dz'. \tag{2.16}$$

Using (2.2), (2.16) can be expressed as

$$\int_{-l/2}^{l/2} \bar{I}_z(z')\left(\frac{\partial^2}{\partial z^2} + k^2\right)G(z,z')dz' = -j\omega\varepsilon\bar{E}_z^i(\rho = a), \tag{2.17}$$

which is called Pocklington's integrodifferential equation [4]-[6]. It can be used to determine the equivalent filamentary line-source current of the wire and current density on the wire, when the incident field on the surface of the wire is known. It is a simplified form when the wire is very thin $(a << \lambda)$. The $G(z,z')$ can be reduced to

$$G(z,z') = G(R) = \frac{e^{-jkR}}{4\pi R}. \tag{2.18}$$

Using (2.18), (2.17) can also be expressed in a more convenient form as

$$\int_{-l/2}^{l/2} \bar{I}_z(z')\frac{e^{-jkR}}{4\pi R^5}\left[(1+jkR)(2R^2 - 3a^2) + (kaR)^2\right]dz' = -j\omega\varepsilon\bar{E}_z^i(\rho = a). \tag{2.19}$$

Note that $\bar{I}_z(z')$ represents the unknown equivalent filamentary current on the surface of conducting wire, $\bar{E}_z^i$ represents the z component of the incident electric field.

2.2.3 Source Modeling

For the conducting wire in Fig. 2.2, the wire is symmetrically fed by a voltage source, which is a dipole antenna. If the Pocklington's integral equation is used, there are two conventional methods used to model the excitation of the dipole antenna; i.e., the delta-gap excitation and equivalent magnetic ring current (magnetic-frill generator) [4].

2.2.3.1 Delta Gap

The delta-gap source modeling is the simplest and most widely used, but it is the least accurate, especially for the input impedance calculation. It will be more accurate for smaller width gaps. It is assumed that the excitation voltage at the feeding terminals is of a constant V_i value and zero elsewhere as

$$\bar{M}_i = -\hat{n} \times \bar{E}^i = -\hat{a}_\rho \times \hat{a}_z \frac{V_i}{\Delta} = \hat{a}_\phi \frac{V_i}{\Delta}, \qquad -\frac{\Delta}{2} \le z' \le \frac{\Delta}{2}. \tag{2.20}$$

The magnetic current density ($\bar{M}_i$) is sketched in Fig. 2.3(a). Note that $\bar{E}^i$ is the incident electric field and $\hat{n}$ is the normal unit vector [4].

2.2.3.2 Magnetic-Frill Generator

The magnetic-frill generator was introduced to calculate the near and the far zone fields from coaxial apertures [4]. The feeding gap is replaced with a circumferentially directed magnetic current density. It consists of annular aperture with the inner (a) and outer (b) radii as shown in Fig. 2.3(b). The magnetic-frill generator is found using the expression for the characteristic impedance of the transmission line. At the annular aperture of the magnetic-frill, the electric field is represented by the transverse electromagnetic mode (TEM) mode field distribution of a coaxial transmission line, where the field generated on the surface of the wire can be expressed as follows:

$$\bar{E}_z^i(\rho=0,-\frac{l}{2}\le z\le\frac{l}{2})=-\frac{V_i}{2\ln(b/a)}\left[\frac{e^{-jkR_1}}{R_1}-\frac{e^{-jkR_2}}{R_2}\right], \tag{2.21}$$

where $R_1=\sqrt{z^2+a^2}$ and $R_2=\sqrt{z^2+b^2}$.

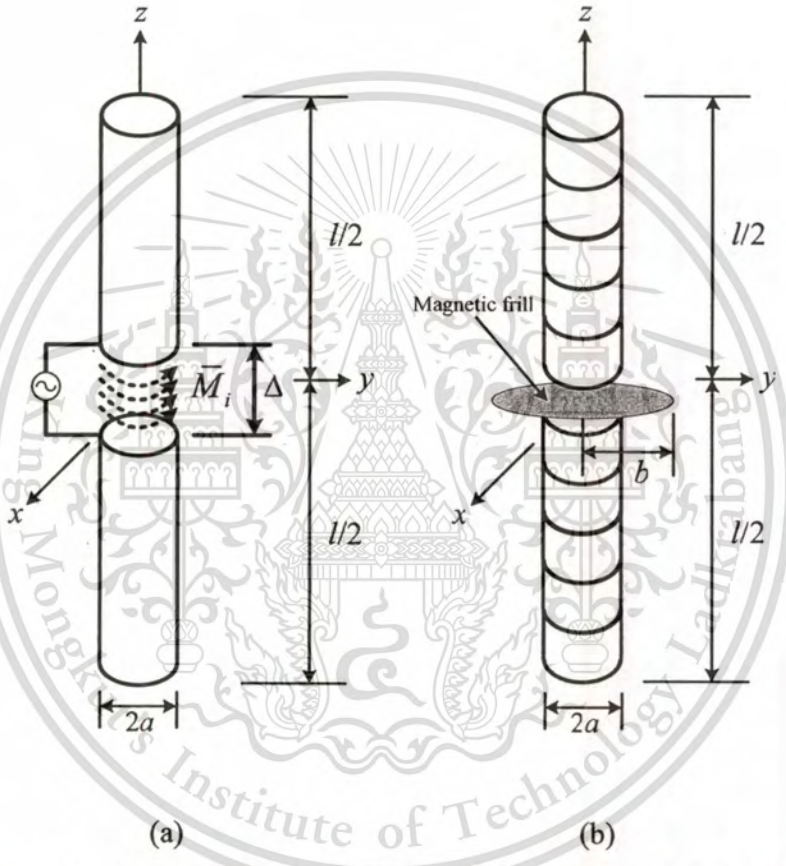

Figure 2.3 Cylindrical dipole with the excitation [4]. (a) Delta gap, and (b) Magnetic-frill generator.

2.3 Method of Moments (MM)

To transform (2.19) to the matrix equation, the method of *weighted residuals* is utilized in conjunction with the inner product of weighting function. This technique is called *Method of Moments* (MM). It is a general procedure for solving the IE. The procedure to employ the MM with the IE involves three steps: [4]-[5]

$$\bar{E}_z^i(\rho=0,-\frac{l}{2}\le z\le\frac{l}{2})=-\frac{V_i}{2\ln(b/a)}\left[\frac{e^{-jkR_1}}{R_1}-\frac{e^{-jkR_2}}{R_2}\right], \tag{2.21}$$

where $R_1=\sqrt{z^2+a^2}$ and $R_2=\sqrt{z^2+b^2}$.

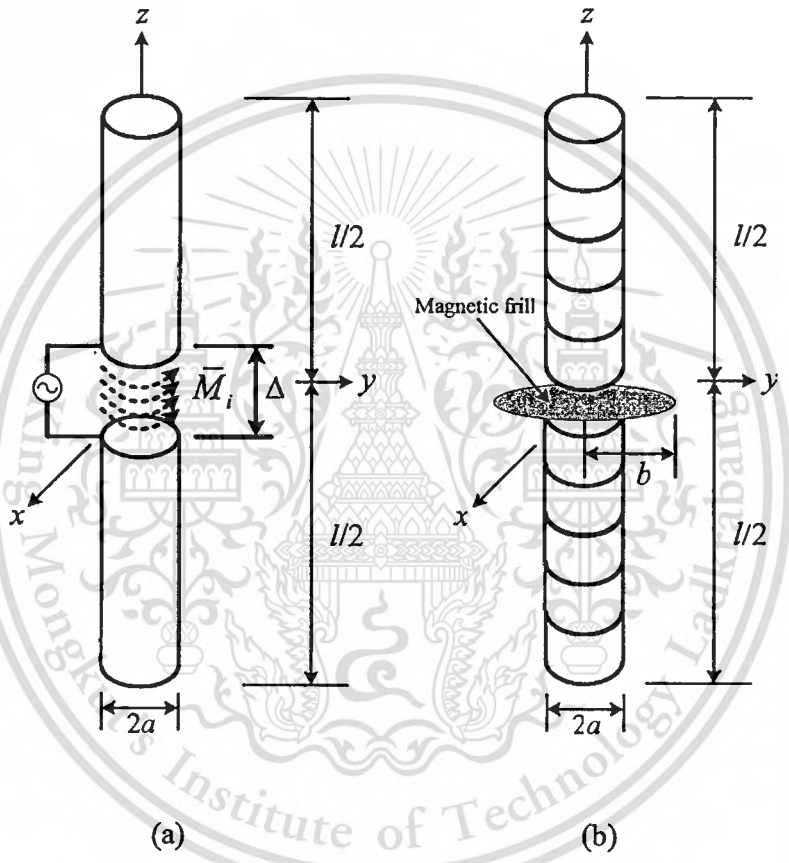

Figure 2.3 Cylindrical dipole with the excitation [4]. (a) Delta gap, and (b) Magnetic-frill generator.

2.3 Method of Moments (MM)

To transform (2.19) to the matrix equation, the method of *weighted residuals* is utilized in conjunction with the inner product of weighting function. This technique is called *Method of Moments* (MM). It is a general procedure for solving the IE. The procedure to employ the MM with the IE involves three steps: [4]-[5]

1. The discretization of the IE into the matrix equation by using the expansion and testing functions.
2. Evaluation of each matrix element.
3. Solving the matrix equation.

From the IE point of view, (2.19) can be written in the form of

$$F(g) = h, \tag{2.22}$$

where F is a known linear operator, h is a known excitation function, and g is the response function. Note that the linearity of the operator (F) makes a solution possible. The discretization of the IE requires that the unknown expansion function (the response function) can be expanded as a linear combination of N terms; i.e.,

$$g(z') = \sum_{n=1}^{N} a_n g_n(z'), \tag{2.23}$$

where a_n is an unknown constant, and g_n is a known expansion function. Substituting (2.23) into (2.22) and using the fact that F is a linear operator, Equation (2.22) can be rewritten as

$$\sum_{n=1}^{N} a_n F(g_n) = h. \tag{2.24}$$

Note that (2.24) is only one equation with N unknowns, which it is not sufficient to solve. This can be accomplished by evaluating (2.24) at N different points. Forming the inner product between each function and the testing function or weighting function (w_m), (2.24) can be reexpressed as

$$\langle w_m, h \rangle = \sum_{n=1}^{N} a_n \langle w_m, F(g_n) \rangle, \qquad m = 1, 2, \ldots, N. \tag{2.25}$$

where the inner product $\langle w, g \rangle = \iint_S w^* \cdot g ds$, the w's are the weighting (testing) functions, the asterisk (*) indicates complex conjugation and S is the surface of the structure being analyzed. Then, (2.25) can be rewritten in the matrix equation form as

$$[h_m] = [F_{mn}][a_n], \tag{2.26}$$

or

$$[V_m] = [Z_{mn}][I_n], \tag{2.27}$$

where $[F_{mn}]$ or $[Z_{mn}]$ represents the $N \times N$ impedance matrix, $[h_m]$ or $[V_m]$ represents the known excitation voltage vector, and $[a_n]$ or $[I_n]$ represents the unknown current vector.

2.3.1 Basis Functions

The basis function is important for the MM solution, which affects the accuracy and computational time. There are several possible basis functions, which can be classified into two classes; i.e., subdomain and entire domain basis functions. This section will describe some of the popular basis functions. [4]-[5]

2.3.1.1 Subdomain Basis Functions

The subdomain functions are nonzero only over a part of the domain of the function g_n. Its domain is the surface of the structure. It approach involves subdivision of the structure into N nonoverlapping segments, as illustrate on the axis in Fig. 2.4 (a). The piecewise constant (PWC) basis function or pulse basis function is the conceptually simple. It is shown in Fig. 2.4, where g_n is defined as

$$g_n(z') = \begin{cases} 1, & z'_{n-1} \le z' \le z'_n \\ 0, & \text{elsewhere} \end{cases}. \tag{2.28}$$

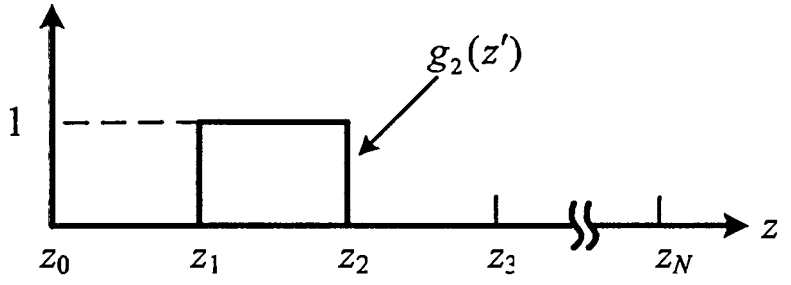

(a)

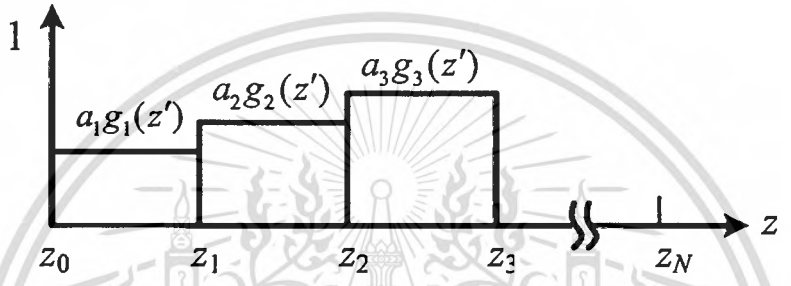

(b)

Figure 2.4 Piecewise constant basis function [4]. (a) Single piecewise constant, and (b) Multiple piecewise constants.

For increasing the sophistication of subdomain basis function, it is possible to improve accuracy. The piecewise sinusoid (PWS) basis function is employed, which is shown in Fig. 2.5. g_n is defined as

$$g_n(x') = \begin{cases} \dfrac{\sin[k(z'-z'_{n-1})]}{\sin[k(z'_n-z'_{n-1})]}, & z'_{n-1} \le z' \le z'_n \\ \dfrac{\sin[k(z'_{n+1}-z')]}{\sin[k(z'_{n+1}-z'_n)]}, & z'_n \le z' \le z'_{n+1} \\ 0, & \text{elsewhere} \end{cases} . \tag{2.29}$$

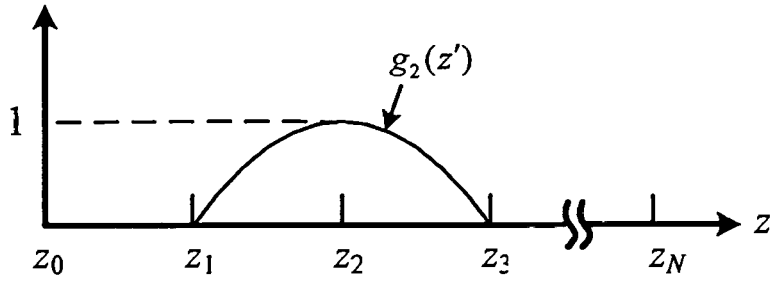

(a)

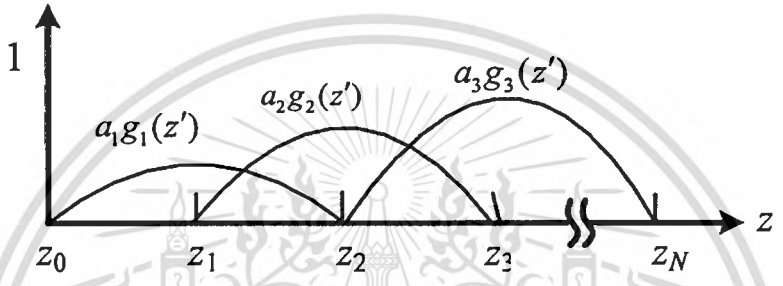

(b)

Figure 2.5 Piecewise sinusoidal basis function [4]. (a) Single piecewise sinusoid, and (b) Multiple piecewise sinusoids.

Note that the PWS basis function has advantages in computational time and resistance to errors compared with the PWC basis function [4].

2.3.1.2 Entire Domain Basis Functions

Entire domain basis functions are defined and they are nonzero over the entire length of the structure being considered. Thus no segmentation is involved in their use. The sinusoidal entire domain basis functions with no segmentation involved in their use. It is defined as

$$g_n(z') = \cos\left[\frac{(2n-1)\pi z'}{l}\right], \qquad -\frac{l}{2} \le z' \le \frac{l}{2} \quad . (2.30)$$

Note that this basis function set would be particularly useful for modeling the current distribution on a wire dipole. It is known to have primarily sinusoidal distribution.

The main advantage of entire domain basis function lies in problems where the unknown function is assumed a priori to follow a known pattern [4]-[5].

2.4 Multiple Sweep Method of Moments (MSMM)

A variation of the MM, called the Multiple Sweep Method of Moments (MSMM), has been applied in various radiation/scattering EM problems [1], [20]-[24]. The MSMM is a stationary method, and it is an $O(N^2)$ *recursive technique*, where the total number of unknowns N of currents on structures of interest can be determined in a recursive fashion. In the MSMM, the structure is split into P sections, and the currents on these sections are determined in a *recursive fashion*. For large antenna arrays in free space, the MSMM has been found to provide relatively fast convergence. For the MSMM, the first sweep includes the dominant radiation/scattering mechanisms, and each subsequent sweep includes higher order mechanisms. Thus, the MSMM can provide more physical insights into radiation/scattering mechanisms of large antenna arrays. In this section, the MSMM procedure for collinear and planar dipole antenna arrays are discussed in detail.

2.4.1 The MSMM Procedure for the Collinear Dipole Antenna Array

The MSMM procedure for dipole antenna array in free space is described. For convenience in understanding in the MSMM, the analysis of collinear dipole antenna array as shown in Fig. 2.6 is first presented. In the MSMM, the object of interest is split into P sections, and the currents on these sections are found in a *recursive fashion* [1], [24].

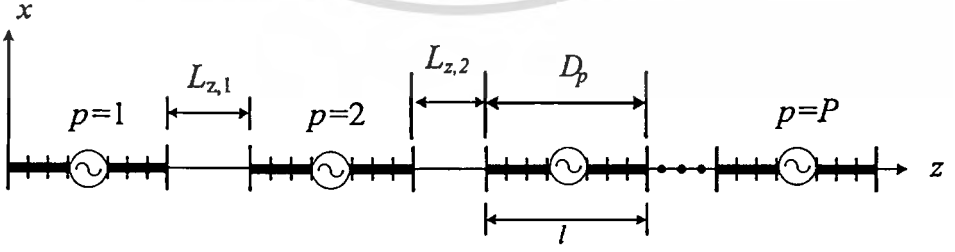

Figure 2.6 Collinear dipole antenna array for the MSMM solution.

In Fig. 2.6, the collinear dipole antenna array is split into P identical sections and $N_p = N/P$ expansion functions for each section of width D_p, where D_p is chosen to be the dipole length l for convenience in illustration, and $L_{z,p}$ denotes the distance between adjacent elements along the z axis. The optimum number of sections, P_{opt}, for computing the optimum width, $D_{p,opt}$, will be discussed later. For the MSMM calculation, (2.27) can be expressed in the block matrix form as

$$\begin{bmatrix} \bar{\bar{Z}}_{11} & \bar{\bar{Z}}_{12} & \cdots & \bar{\bar{Z}}_{1p} & \cdots & \bar{\bar{Z}}_{1P} \\ \bar{\bar{Z}}_{21} & \bar{\bar{Z}}_{22} & \cdots & \bar{\bar{Z}}_{2p} & \cdots & \bar{\bar{Z}}_{2P} \\ \vdots & \vdots & \vdots & \vdots & \vdots & \vdots \\ \bar{\bar{Z}}_{p1} & \bar{\bar{Z}}_{p2} & \cdots & \bar{\bar{Z}}_{pp} & \cdots & \bar{\bar{Z}}_{pP} \\ \vdots & \vdots & \vdots & \vdots & \vdots & \vdots \\ \bar{\bar{Z}}_{P1} & \bar{\bar{Z}}_{P2} & \cdots & \bar{\bar{Z}}_{Pp} & \cdots & \bar{\bar{Z}}_{PP} \end{bmatrix} \begin{bmatrix} \bar{I}_1 \\ \bar{I}_2 \\ \vdots \\ \bar{I}_p \\ \vdots \\ \bar{I}_P \end{bmatrix} = \begin{bmatrix} \bar{V}_1^i \\ \bar{V}_2^i \\ \vdots \\ \bar{V}_p^i \\ \vdots \\ \bar{V}_P^i \end{bmatrix}, \tag{2.31}$$

where $\bar{\bar{Z}}_{pq}$ is the $N_p \times N_p$ block matrix containing the mutual impedances between expansion functions in sections p and q, $\bar{V}_p^i$ contains the N_p elements of the excitation voltage vector for section p, and $\bar{I}_p$ contains the N_p elements of the unknown current vector for section p. It is noted that, for the first MSMM sweep, there is no need to employ the resistive card (R-card) [1], [24] at the end of each section due to existing physical discontinuity at the ends of each array element.

For each MSMM sweep, the current on each section $\bar{I}_p$ is computed *recursively*. The general form to compute $\bar{I}_p^{(t)}$ for each MSMM sweep t is given as follows:

$$\bar{\bar{Z}}_{pp}\bar{I}_p^{(2m+1)} = \bar{V}_p^i - \sum_{j=1}^{p-1} \bar{\bar{Z}}_{pj}\bar{I}_j^{(2m+1)} - \sum_{j=p+1}^{P} \bar{\bar{Z}}_{pj}\bar{I}_j^{(2m)}, \quad p:1 \to P, \tag{2.32}$$

where $\bar{I}_p^{(0)} = \bar{0}$ for a first sweep $t = 1$, $m = 0, 1, 2, \ldots$ and

$$\bar{\bar{Z}}_{pp}\bar{I}_p^{(2m)} = \bar{V}_p^i - \sum_{j=1}^{p-1}\bar{\bar{Z}}_{pj}\bar{I}_j^{(2m-1)} - \sum_{j=p+1}^{P}\bar{\bar{Z}}_{pj}\bar{I}_j^{(2m)}, \qquad p: P \to 1, \tag{2.33}$$

where $m = 1, 2, 3, \ldots$.

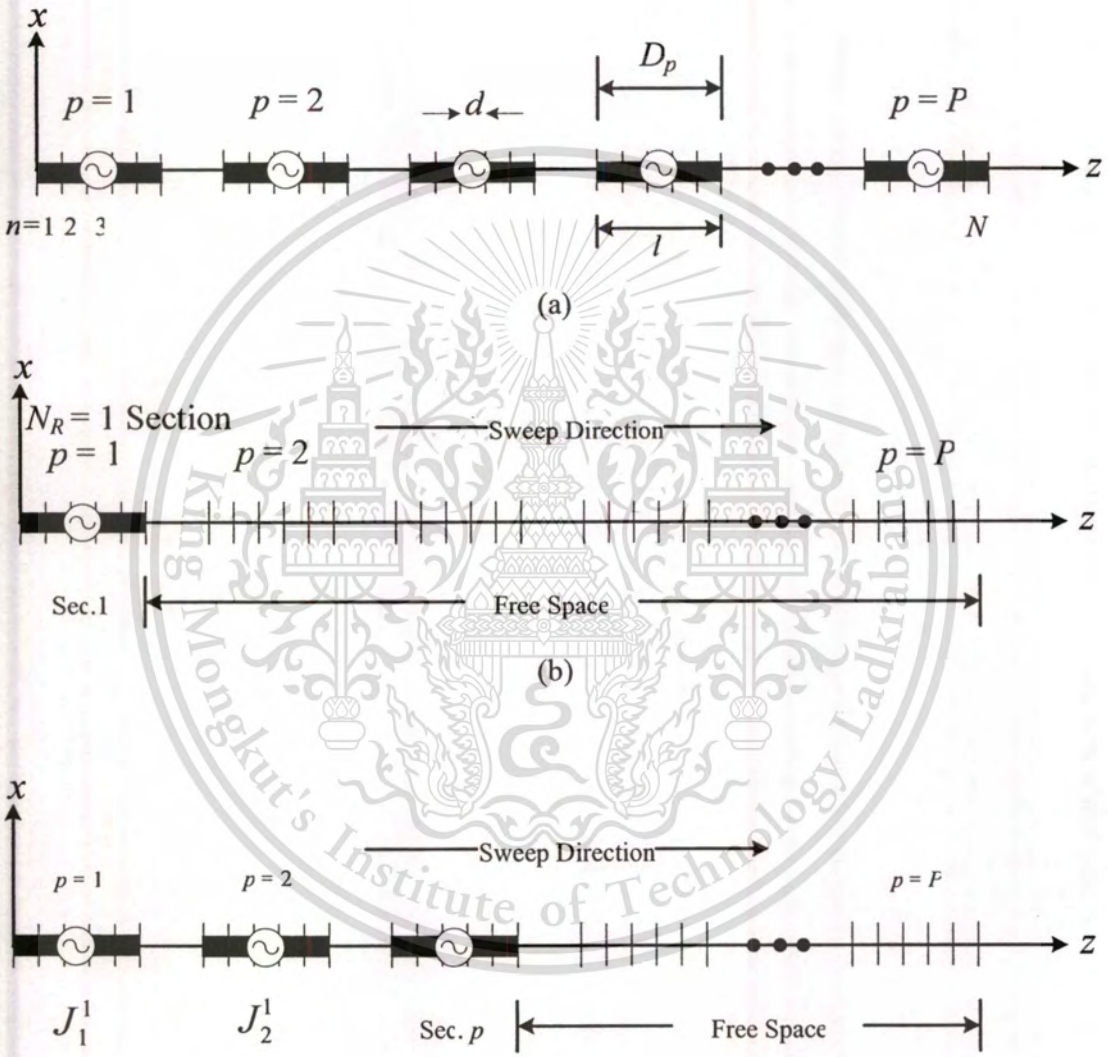

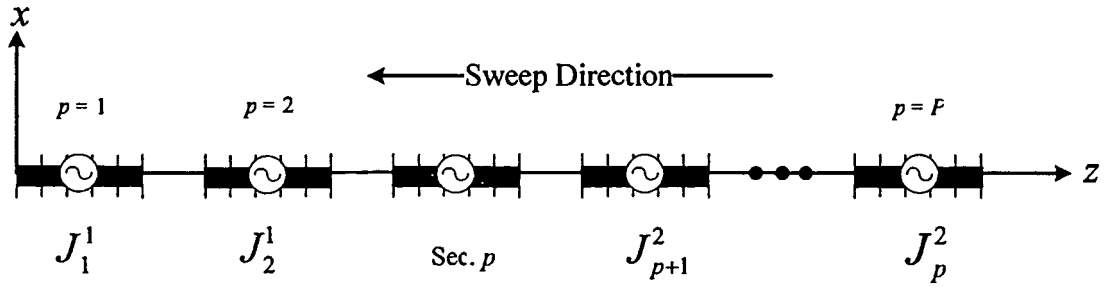

(d)

Figure 2.7 The MSMM procedure of the collinear dipole antenna array. (a) Geometry for the MSMM solution, (b) Computing the 1st sweep current on section p = 1, (c) Computing the 1st sweep current on section p, and (d) Computing the 2nd sweep current on section p.

2.4.1.1 The First MSMM Sweep

The first MSMM sweep begins with computing the current distribution, $J_{p=1}^{t=1}$, on section p = 1, which it is a dipole antenna. The remaining sections have no current, which are considered as the free space [1], [24]. In this thesis, there is no need to employ the R-card at the end of each section due to existing physical discontinuity at the ends of each array element as shown in Fig. 2.7(b). After the current distribution on section $p = 1$ is determined in (2.32), the current distribution on section p = 2, $J_{p=2}^{t=1}$, is computed by considering the radiation from the current distribution of the previous section ($J_{p=1}^{t=1}$) as shown in Fig. 2.7(c) and using (2.32). This process continues from the left hand side to the right hand side ($p: 1 \rightarrow P$) until $p = P$.

2.4.1.2 The Second and Subsequent MSMM Sweeps

The second sweep is processed in the reverse direction; i.e., the section $p = P$ will be computed first then section $p = P$-1, P-2, …, 1 ($p: P \rightarrow 1$). Figure 2.7(d) illustrates the computation of the second sweep on an arbitrary section ($J_p^{t=2}$). For this sweep, the section p is a dipole antenna, where and other sections are represented by the latest computed current distribution. The current distribution on the section p can be computed

via (2.33). For subsequent MSMM sweeps, MSMM odd and even sweeps can be computed using (2.32) and (2.33), respectively.

2.4.2 The MSMM Procedure for the Planar Dipole Antenna Array

In the case of planar dipole antenna array, the forward and backward sweeping directions associated with the MSMM are discussed as shown in Fig. 2.8. The antenna array is split into P identical sections, where each section contains the whole column elements. The current distributions on each section are computed recursively as sweeping forwardly and backwardly in the row direction. It should be pointed out that these sweeping processes can be defined differently. For example, the antenna array can be grouped in row, and associated currents are calculated recursively by the MSMM sweeping in the column direction. Note that, the first, second, and subsequent MSMM sweeps can be performed as in those of the collinear dipole antenna array as shown in Fig. 2.9.

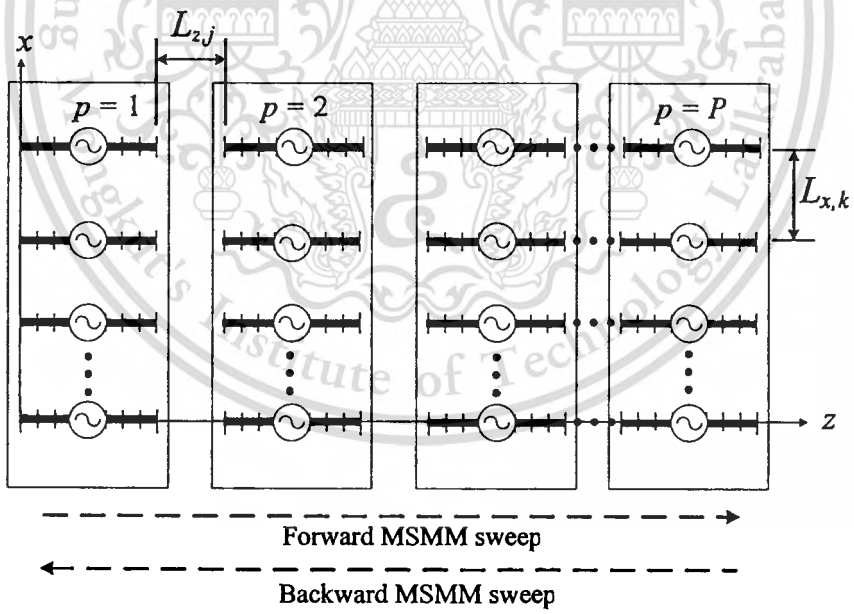

Figure 2.8 Planar dipole antenna array analyzed using the MSMM by sweeping in the row direction.

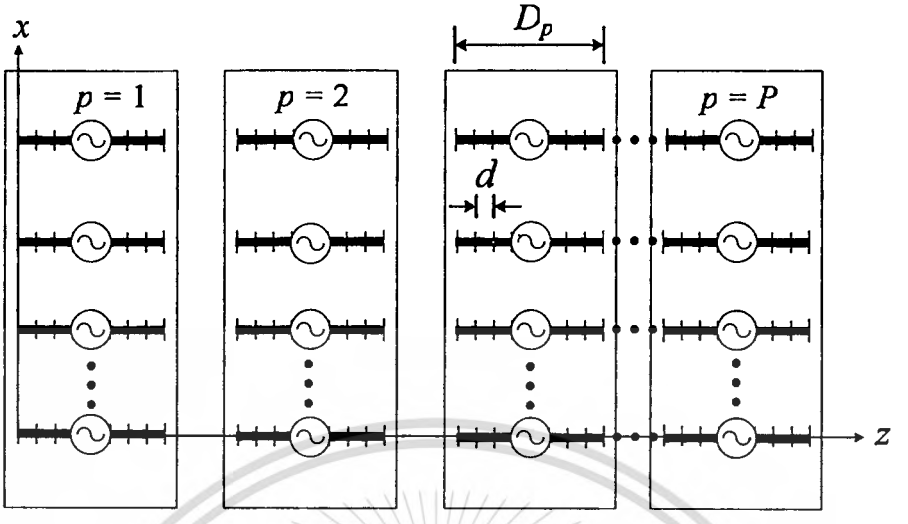

(a)

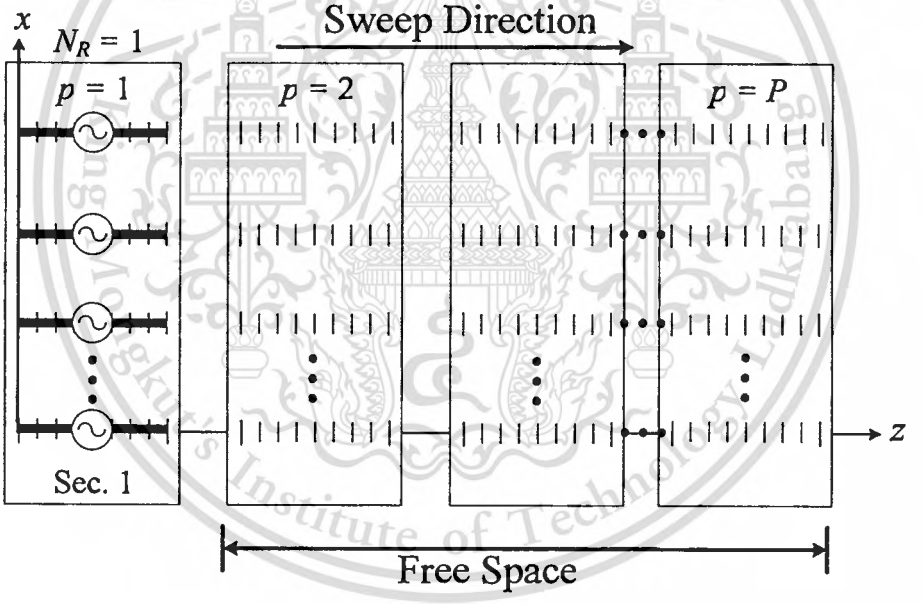

(b)

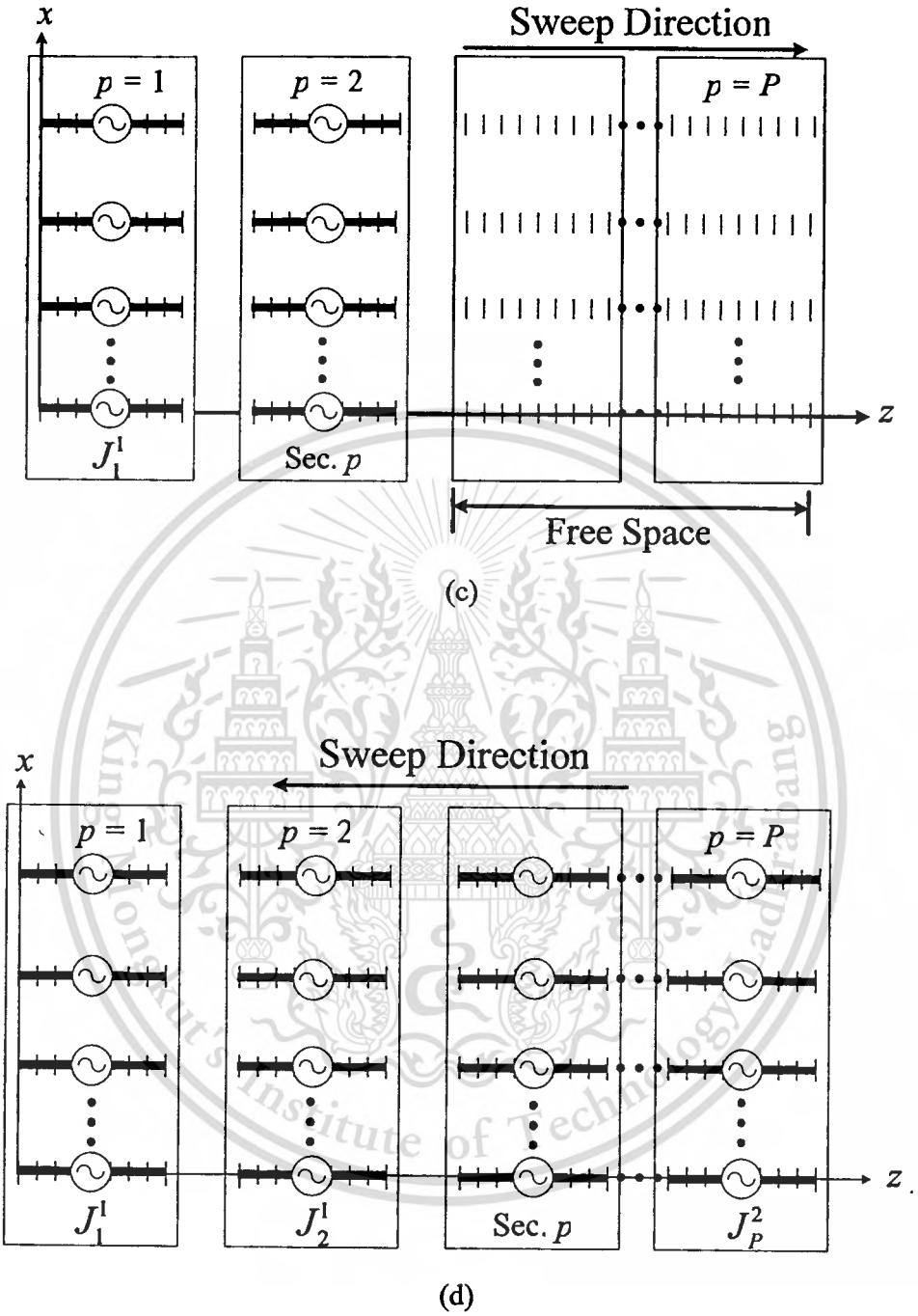

Figure 2.9 The MSMM procedure of the planar dipole antenna array. (a) Geometry for MSMM solution, (b) Computing the 1st sweep current on section $p = 1$, (c) Computing the 1st sweep current on section p, and (d) Computing the 2nd sweep current on section p.

The MSMM sweeping in either row or column direction is not efficient due to the fact that the associated number of unknowns for each section is relatively large, especially for large array problems, resulting in inefficiency in computing $\bar{I}_p^t$ in (2.32) and (2.33). This is due to the fact that the computation of $\bar{I}_p^t$ involves the matrix inversion of $\bar{\bar{Z}}_{pp}$ of relatively large size. To overcome the inefficiency of the MSMM sweeping in either row or column direction, the sawtooth sweep associated with the MSMM is proposed as discussed in the next section.

2.4.3 The MSMM with the Sawtooth Sweep for the Planar Dipole Antenna Array

For the sawtooth sweep, the antenna can be separated into P sections, where each section corresponds to each array element for illustration purpose as shown in Fig. 2.10. For the first sweep, the current distribution of each section is computed by starting from the left section to the right section until the last section of that row is reached. Then, continue on the first section of the next row, and repeat the same process in the sawtooth fashion until the last section ($p = P$) as shown in Fig. 2.10. The second sweep is performed in the reverse order as compared to the first sweep. Note that the odd and even sweeps are performed in the same manner as the first and second sweeps, respectively. It should be pointed out that each section for the MSMM sweeping in either row or column direction is usually larger than that for the MSMM sweeping in the sawtooth fashion, which requires larger block matrix $\bar{\bar{Z}}_{pp}$ in (2.32) and (2.33). Thus, the latter is more efficient than the former. Due to the inefficiency of the former, it will not be considered further in this thesis. Figure 2.11 shows the MSMM with the sawtooth procedure of the planar dipole antenna array.

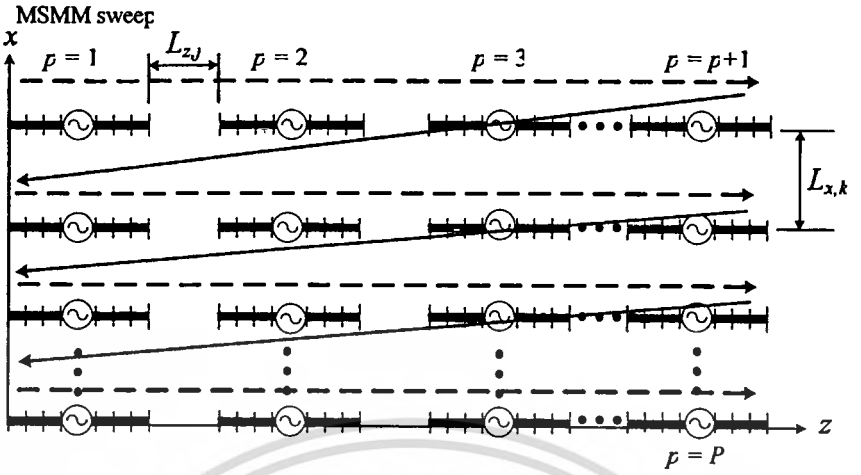

Figure 2.10 The MSMM with the sawtooth sweep of the planar dipole antenna array.

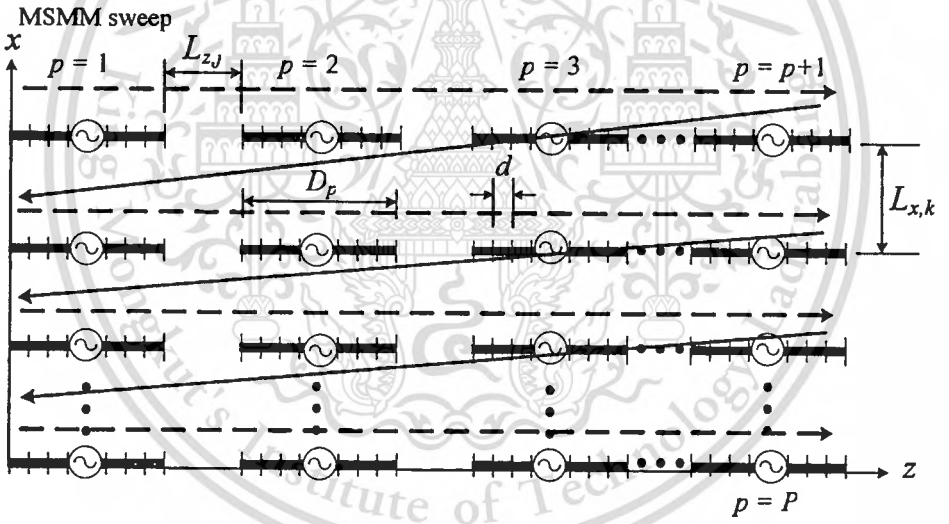

(a)

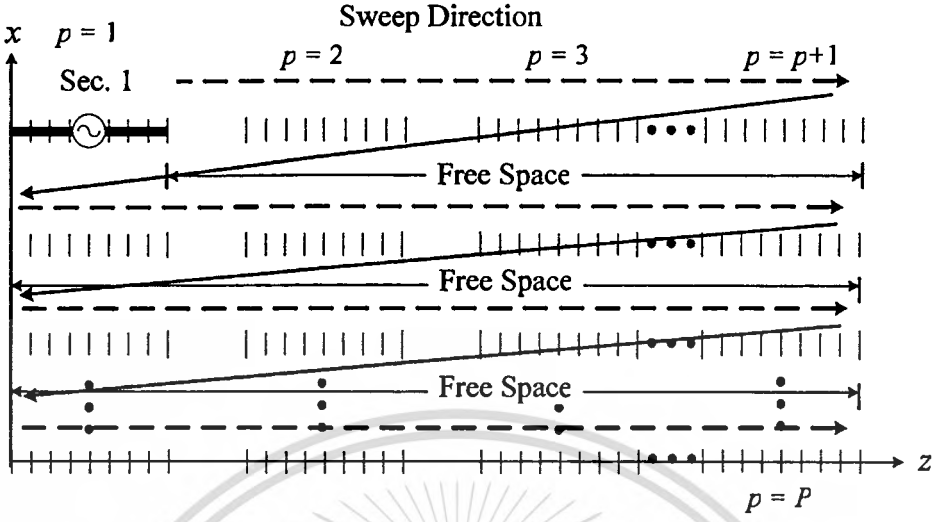

(b)

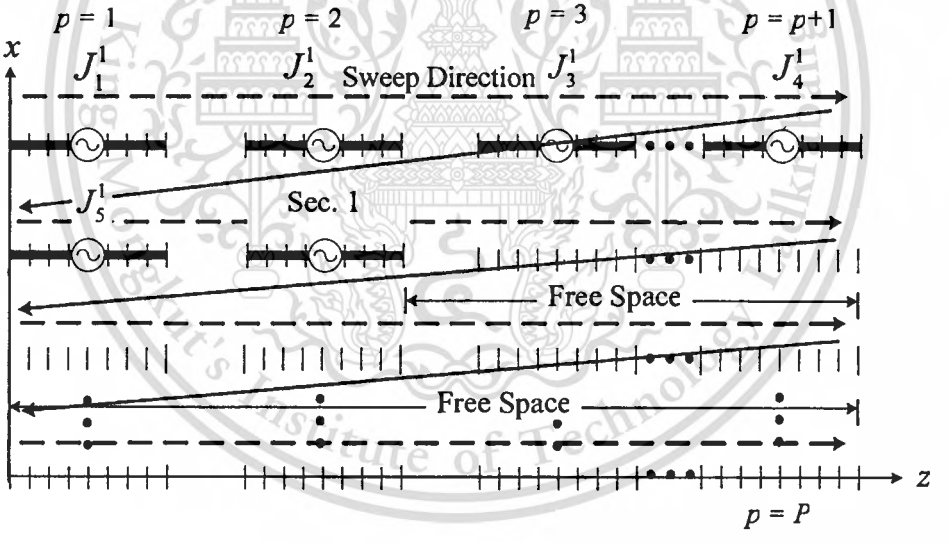

(c)

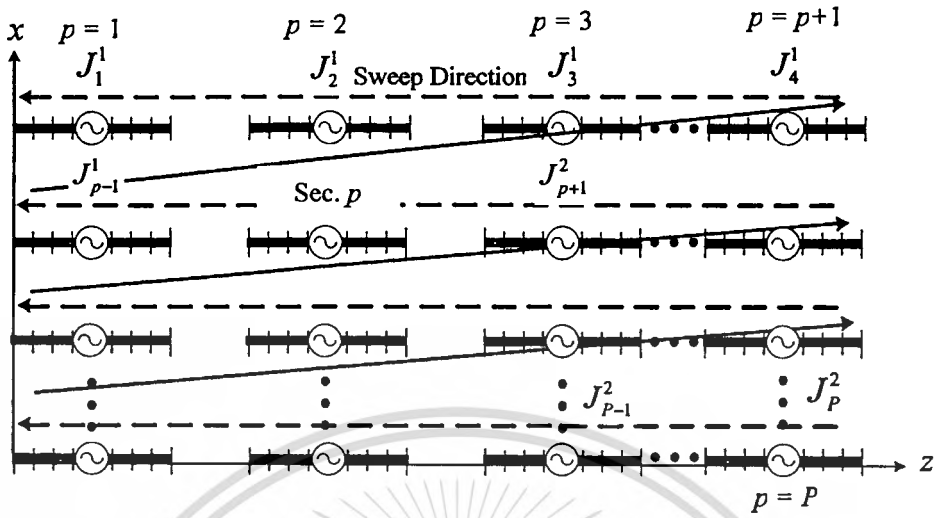

(d)

Figure 2.11 The MSMM procedure with the sawtooth sweep of the planar dipole antenna array. (a) Geometry for the MSMM solution, (b) Computing the 1st sweep current on section p = 1, (c) Computing the 1st sweep current on section p, and (d) Computing the 2nd sweep current on section p.

The total root mean square (RMS) error, E^t, and the residual error norm, R^t, are used to monitor the convergence of the MSMM, where they are defined for the t^{th} iteration as follows [1]

$$E^t = \frac{\sqrt{\sum_{n=1}^{N} \left| \bar{I}_n^t - \bar{I}_n^{(t-1)} \right|^2}}{\sqrt{\sum_{n=1}^{N} \left| \bar{I}_n^{(t-1)} \right|^2}}, \tag{2.34}$$

and

$$R^t = \frac{\left\| \bar{V} - \bar{\bar{Z}}\, \bar{I}^t \right\|}{\left\| \bar{V} \right\|}, \tag{2.35}$$

where $\|\cdot\|$ is the vector norm. The convergence test based on E^t is employed first. Once the $\bar{I}^{(t)}$ vector satisfies this test, another convergence test based on R^t is employed to

ascertain accuracy of the final solution. If $\overline{I}^{(t)}$ does not satisfy a specified accuracy criterion for R^t, the accuracy criterion for E^t is reduced further and the two-step testing is started again until both residuals of $\overline{I}^{(t)}$ are satisfied. The reason for performing this testing procedure is to reduce the number of matrix vector multiplications used in the R^t convergence test while keeping the desired accuracy. It is noted that the E^t convergence test does not require a matrix vector multiplications. However, it may not be an acceptable stopping test for general problems. In contrast, the R^t convergence test is a desirable for stopping test since the solution errors are tied directly to the accuracy of the elements of the impedance matrix $\overline{\overline{Z}}$ and the excitation vector $\overline{V}$ [1], [24].

In the MSMM computation, the number of MSMM sections, P, has effects to both total computational time and convergence rate, which is discussed in detail in [1], [24]. It is found that the optimum number of MSMM sections, P_{opt}, is related to the total number of unknowns N as

$$P_{opt} = 2\sqrt{B/AN}^{1/2}, \tag{2.36}$$

where A is a constant dependent upon the speed of computer, and B is a constant dependent upon the speed of the computer and the solution algorithm [1]. Using the optimum number of MSMM sections, the computational time of the MSMM was found to be $O(N^2)$ as discussed in detail in [1].

2.5 Numerical Results

Numerical results are presented to demonstrate the accuracy and efficiency of the MSMM method. In this section, the MSMM is employed to analyze EM radiation problems of uniform and non-uniform dipole antenna arrays in free space.

2.5.1 Uniform Collinear Dipole Antenna Array

A uniform collinear dipole antenna array of 100 elements is analyzed in this section. The array parameters of Fig. 2.6 are given as follows: $L_{z,k} = 0.5\lambda$ and $l = \lambda$, where λ is a wavelength in free space. Five PWS basis functions for each dipole element

with radius of 0.005λ are employed resulting in $N = 500$, and each element is excited by 1 Volt at the center. Figure 2.12 shows a comparison of RMS errors (E^t) for the MSMM and the CG method. Note that both methods initialize the unknown current vector $\overline{I}$ with the zero vector. In this study, the RMS error of 10^{-2} is employed for convergence criterion. From Fig. 2.12, the MSMM and the CG method converge within 3 iterations, respectively. The MSMM shows rapid convergence, while the CG method shows convergence with some fluctuations.

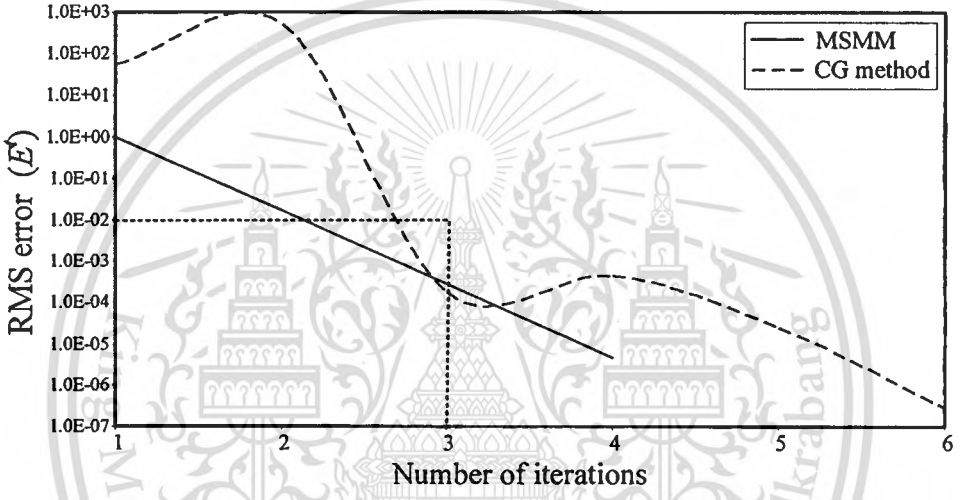

Figure 2.12 RMS errors of the MSMM and the CG method for a uniform collinear dipole antenna array of 100 elements.

In addition, the error in computing the current coefficient for the basis function n on the sweep t (E_n^t) can be computed as [23]-[24]

$$E_n^t = \frac{\left|\mathrm{MM}i_n - \mathrm{MSMM}i_n\right|}{\left|\mathrm{MM}i_n\right|}, \tag{2.37}$$

where $\mathrm{MM}i_n$ and $\mathrm{MSMM}i_n$ are the current coefficients on the mode "n" of the MM and MSMM, respectively. Figure 2.13 shows the error in computing E_n^t for the final iteration of the MSMM and the CG method compared with the MM. It is found that the MSMM

can provide less percentage of error than that of the CG method. In addition, Fig. 2.14 shows the calculated current distribution for both normalized magnitude and phase of the uniform collinear dipole antenna array compared between the MM and the MSMM. It is found that both methods are in excellent agreement. Moreover, Fig. 2.15 illustrates the *E*-plane radiation pattern of the uniform collinear dipole antenna array. It is obvious that the MM and the MSMM method yield identical radiation patterns as well.

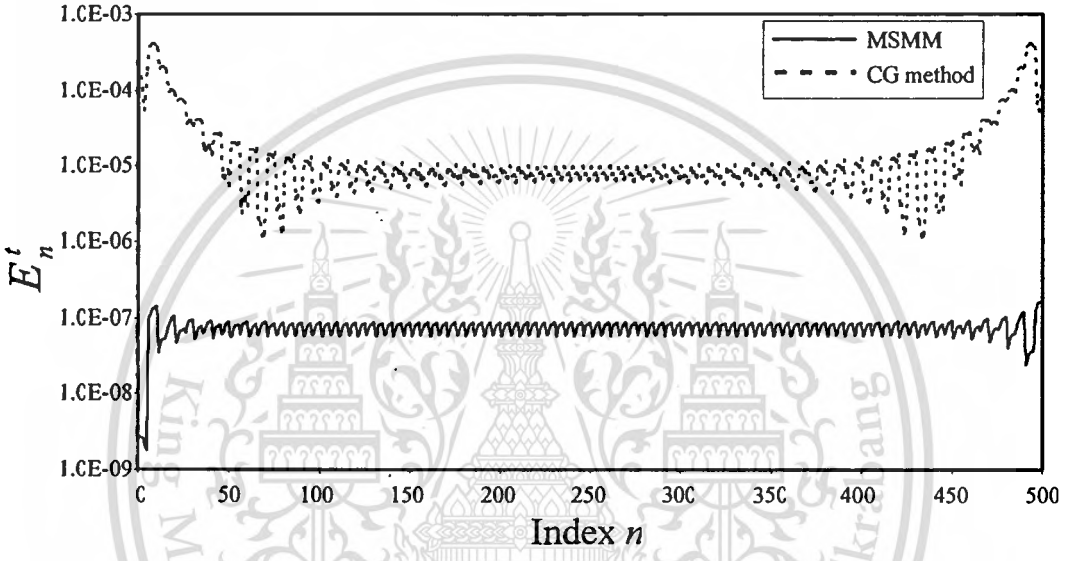

Figure 2.13 Errors in computing E_n^t for the final sweep of the MSMM and the CG method for the uniform collinear dipole antenna array of 100 elements.

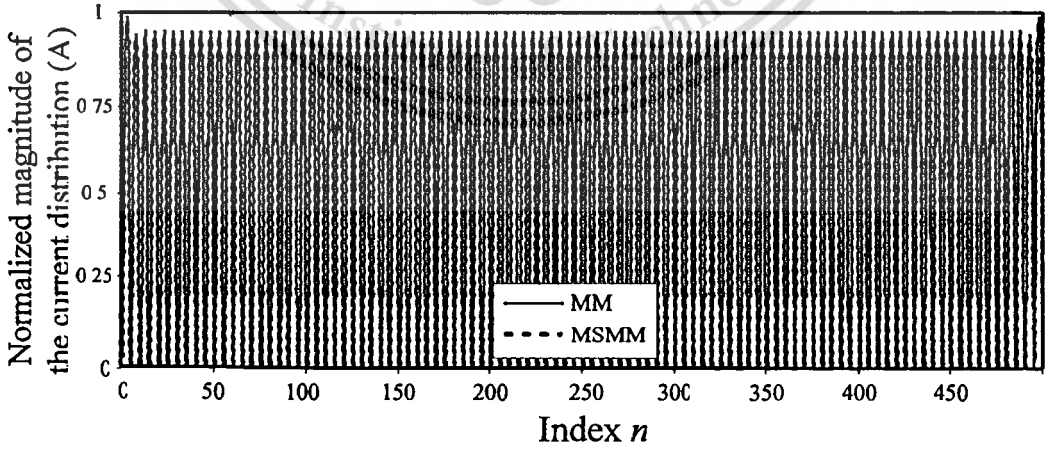

(a)

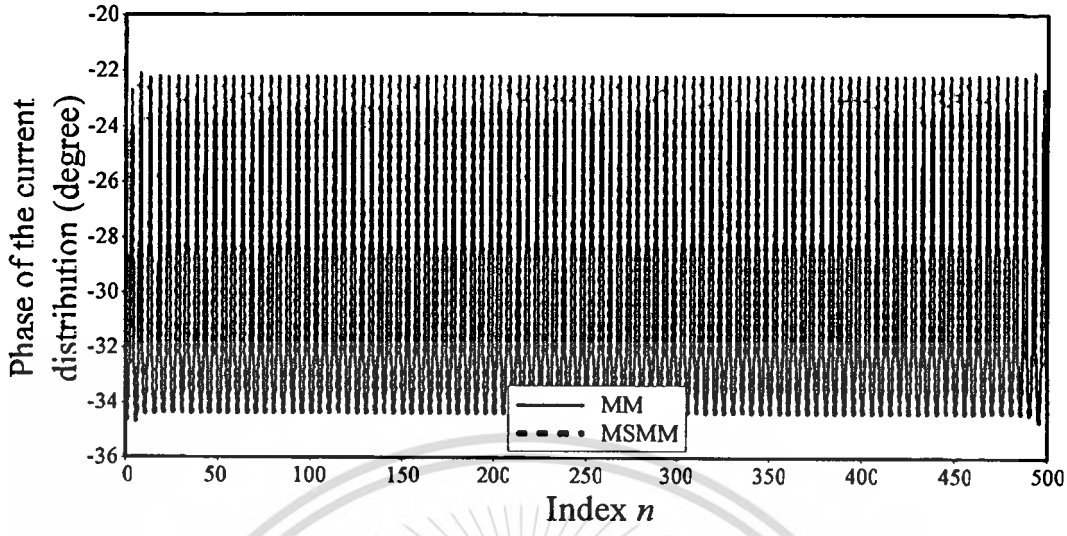

(b)

Figure 2.14 Current distribution of the uniform collinear dipole antenna array of 100 elements. (a) Normalized magnitude of the current distribution, and (b) Phase of the current distribution.

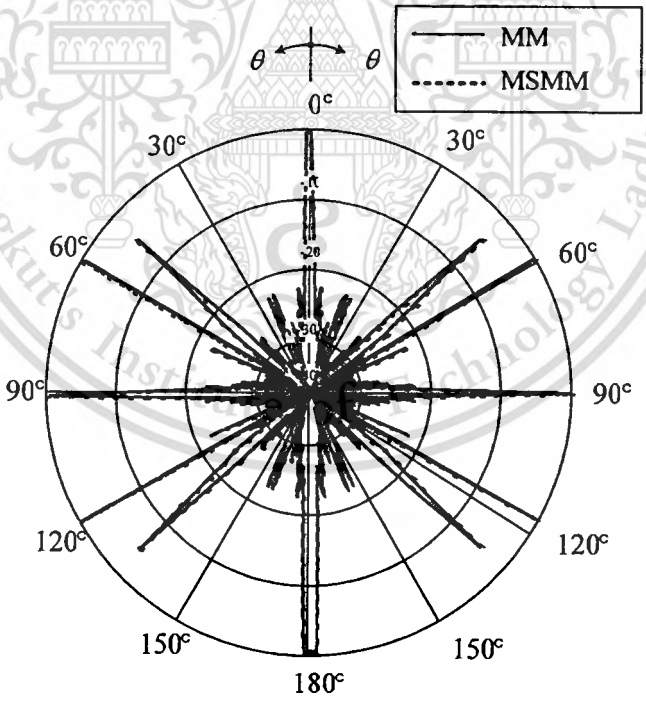

Figure 2.15 The *E*-plane radiation pattern of the uniform collinear dipole antenna array of 100 elements.

2.5.2 Uniform Planar Dipole Antenna Array

This section presents MSMM numerical results for uniform planar dipole antenna arrays in free space. For the 5×5 uniform planar dipole antenna array, the array parameters of Fig. 2.8 are given as follows: $L_{x,j} = L_{z,k} = \lambda$, and $l = 7\lambda$ with radius of 0.005λ. Sixty-three PWS basis functions for each element are used resulting in $N = 1{,}575$, where each element is excited by 1 Volt at the center. In this study, the MSMM with the sawtooth sweep splits the planar array into $P_{opt} \approx 25$ sections (see (2.36)). Figure 2.16 shows the RMS errors (E^t) of the MSMM with the sawtooth sweep and the CG method. In this study, the RMS error of 10^{-2} is employed for convergence criterion.

From Fig. 2.16, the CG method requires 35 iterations to converge to the specified convergence criterion with fluctuation. For the MSMM with the sawtooth sweep, it requires only 4 iterations to converge without any fluctuation. It is obvious from Fig. 2.16 that the MSMM with the sawtooth sweep provides faster and more uniform convergence rate than the CG method for this uniform planar dipole antenna array.

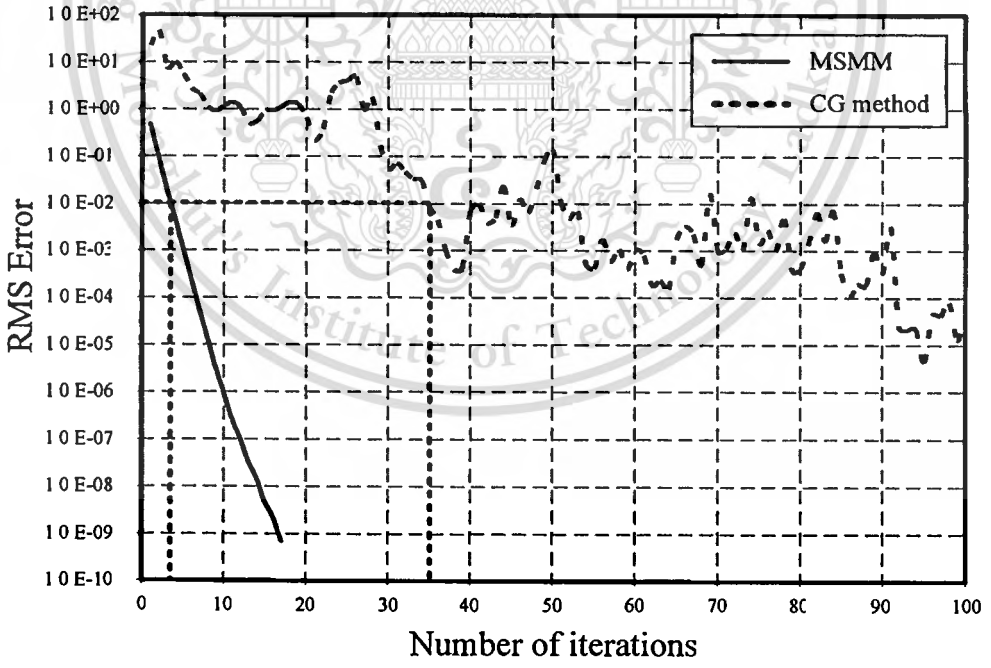

Figure 2.16 RMS errors of the MSMM with the sawtooth sweep and the CG method for the 5×5 uniform planar dipole antenna array.

Figure 2.17 illustrates the plot of the normalized magnitude of the current distribution on the uniform planar dipole antenna array versus the index n computed using the MSMM with the sawtooth sweep for the first ($t = 1$), the second ($t = 2$) and the third ($t = 3$) sweeps. The MM is employed to compute the exact solution for the planar array for comparing with the MSMM results. For the first sweep, the MSMM result is noticeably different from the MM result as shown in Fig. 2.17(a). However, the first sweep includes dominant radiation/scattering mechanisms of this antenna array. After finishing the second sweep, the MSMM result is improved considerably, where both MM and MSMM results are almost identical as shown in Fig. 2.17(b). For the third sweep, the MSMM result is in excellent agreement with the MM result as shown in Fig. 2.17(c). Thus, in this example only few sweeps are required for engineering practice.

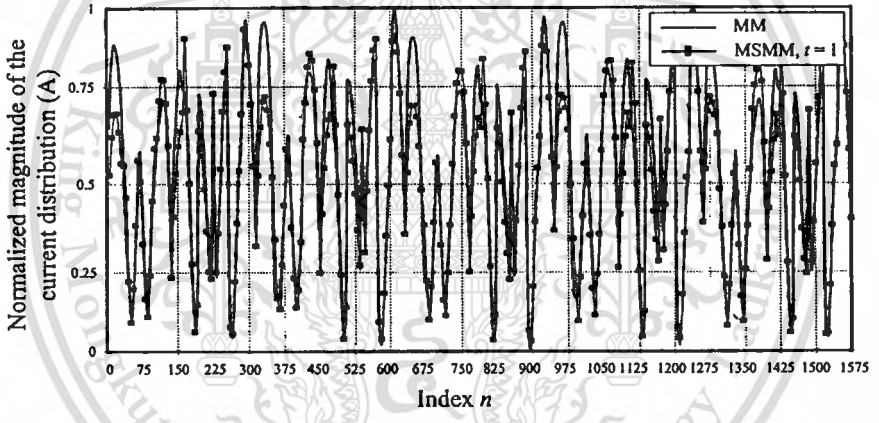

(a) $t = 1$.

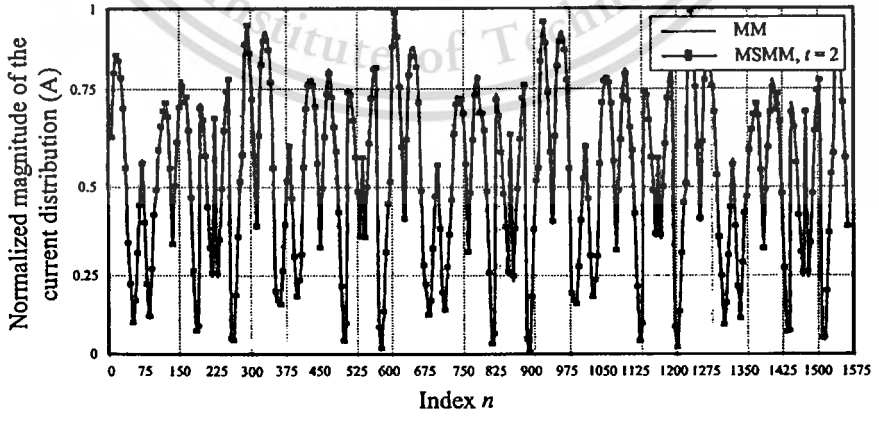

(b) $t = 2$.

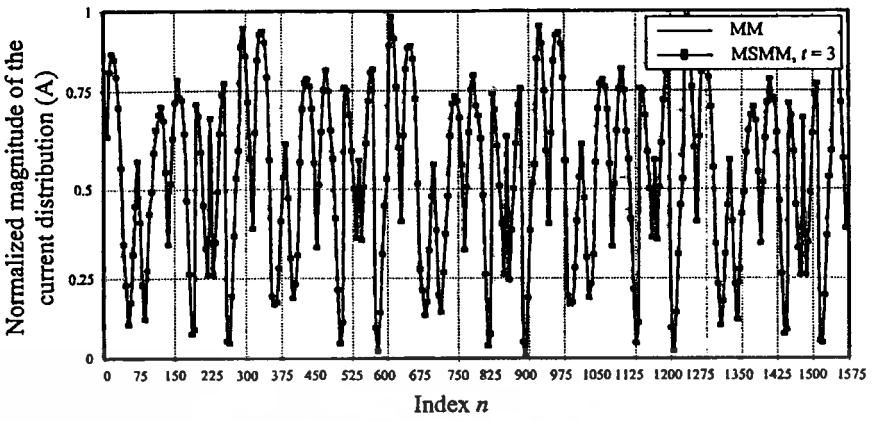

(c) $t = 3$.

Figure 2.17 Normalized magnitude of the current distribution on the 5×5 uniform planar dipole antenna array computed using the MSMM with the sawtooth sweep. (a) First sweep ($t = 1$), (b) Second sweep ($t = 2$), and (c) Third sweep ($t = 3$).

Figure 2.18 shows the plot of E_n^t versus the index n for the sweeps $t = 1$ to 6. The sweep $t = 1$ error begins at about 0.2 at the left edge and then tend to decrease to about 0.01 at the right edge. The sweep $t = 2$ error at the right edge begins about 0.01, and then drops to about 0.002 at the left edge. As the sweeps continue, the overall error continues to drop, and the maximum error is reduced to approximately less than 0.0001 by the sweep $t = 6$. Figure 2.19 shows the comparison of the current distribution for both magnitude and phase of the 5×5 uniform planar dipole antenna array between the MM and the MSMM. They are in very good agreement for both normalized magnitude and phase. In addition, Fig. 2.20 illustrates the E-plane radiation pattern of the antenna array. It is obvious that the MM and MSMM results are in excellent agreement. Next, an example of non-uniform collinear dipole antenna arrays is considered.

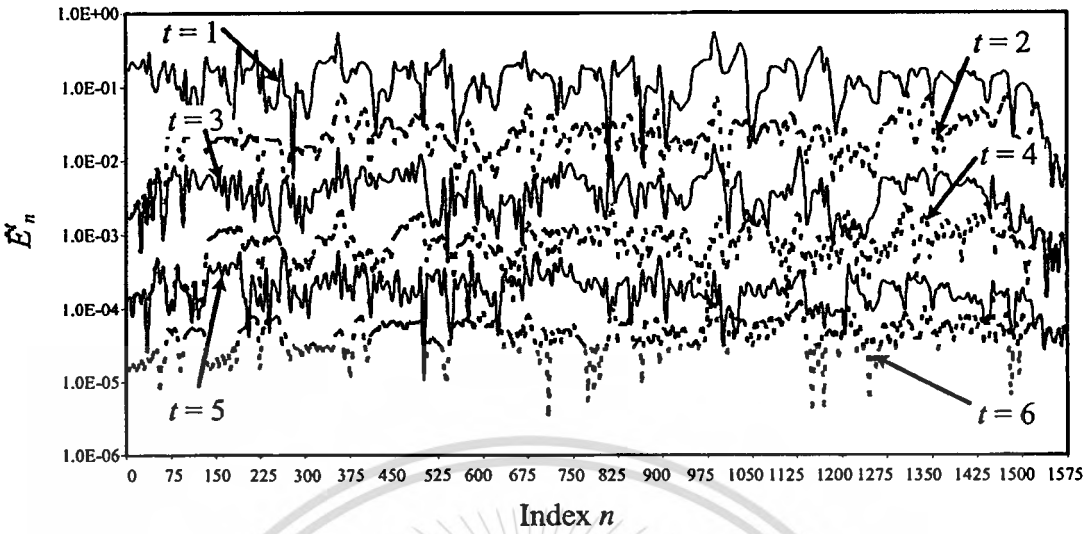

Figure 2.18 Errors in computing E_n^t for the sweeps t = 1 to 6.

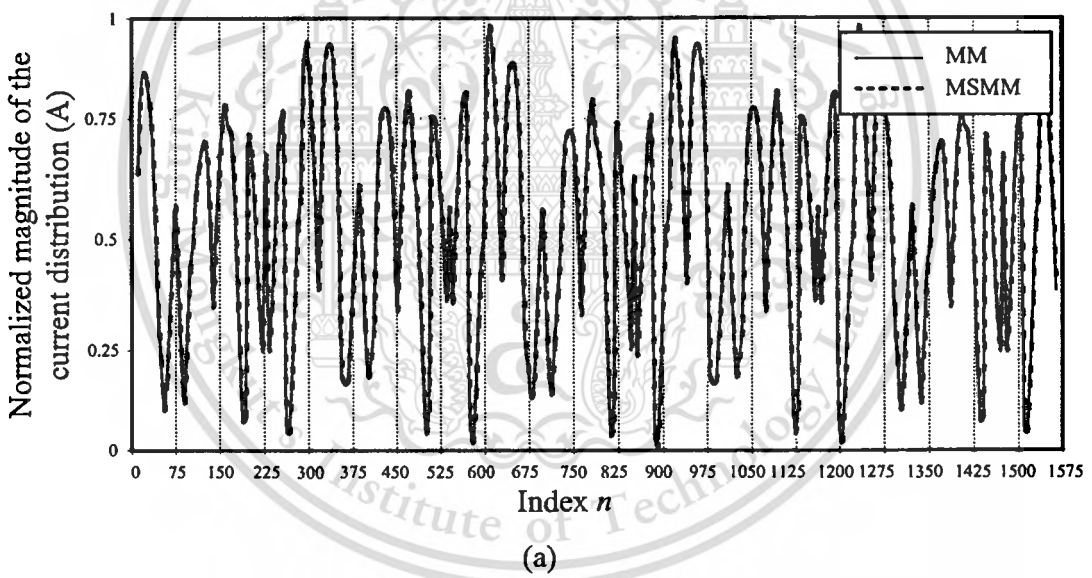

(a)

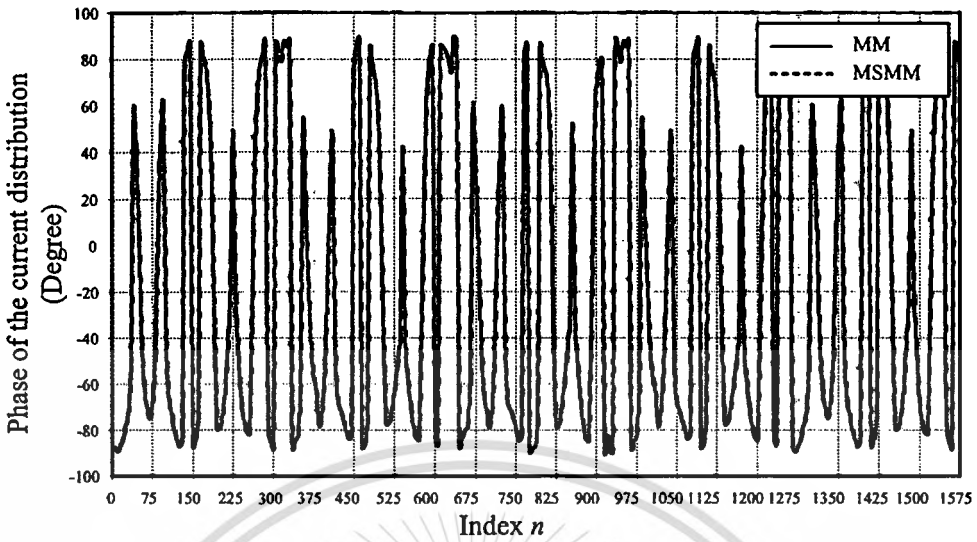

(b)

Figure 2.19 Normalized magnitude and phase of the current distribution of the 5×5 uniform planar dipole antenna array. (a) Normalized magnitude of the current distribution, and (b) Phase of the current distribution.

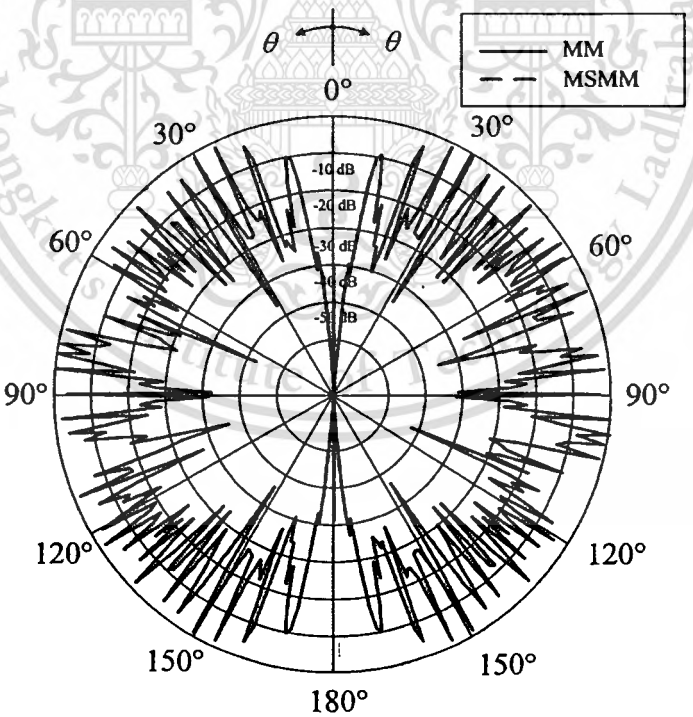

Figure 2.20 The *E*-plane radiation pattern of the 5×5 uniform planar dipole antenna array.

2.5.3 Non-uniform Collinear Dipole Antenna Array

This section presents MSMM numerical results for a non-uniform collinear dipole antenna array in free space. Consider a non-uniform collinear dipole antenna array of 26 elements, where the array parameters of Fig. 2.6 are given as $l = 0.5\lambda$ with 0.005λ radius, and the distances between each element are given in Table. 2.1. Only 13 elements are shown due to its symmetrical structure. Nine PWS basis functions for each element are used resulting in $N = 234$, where each element is excited by 1 Volt at the center. Figure 2.21 shows the RMS errors (E^t) of the MSMM and the CG method. In this study, the RMS error of 10^{-2} is employed for convergence criterion. It is found that the MSMM still converge faster than the CG method, which it requires only 4 iterations.

Table 2.1 Distance between each element of 26 elements of non-uniform collinear dipole antenna array.

Parameters	Distance (λ)
$L_{z,1}$	1.406
$L_{z,2}$	1.177
$L_{z,3}$	1.005
$L_{z,4}$	1.392
$L_{z,5}$	0.739
$L_{z,6}$	1.036
$L_{z,7}$	0.233
$L_{z,8}$	1.398
$L_{z,9}$	0.522
$L_{z,10}$	0.892
$L_{z,11}$	0.732
$L_{z,12}$	0.423
$L_{z,13}$	0.424

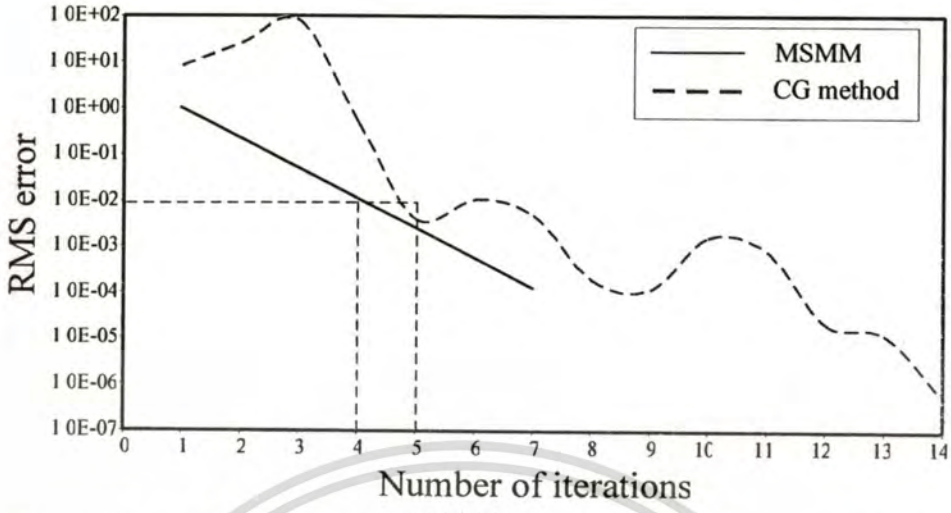

Figure 2.21 RMS errors of the MSMM and the CG method for the non-uniform collinear dipole antenna array of 26 elements.

In addition, E_n^t of the MSMM and the CG method are shown in Fig. 2.22. It is found that the overall error of the MSMM less than the CG method. Furthermore, the normalized magnitude and phase of the current distribution of the non-uniform planar dipole antenna array are shown in Fig. 2.23, which are in excellent agreement. For the *E*-plane radiation pattern, it is found that the MM and the MSMM, provide identical radiation patterns as shown in Fig. 2.24.

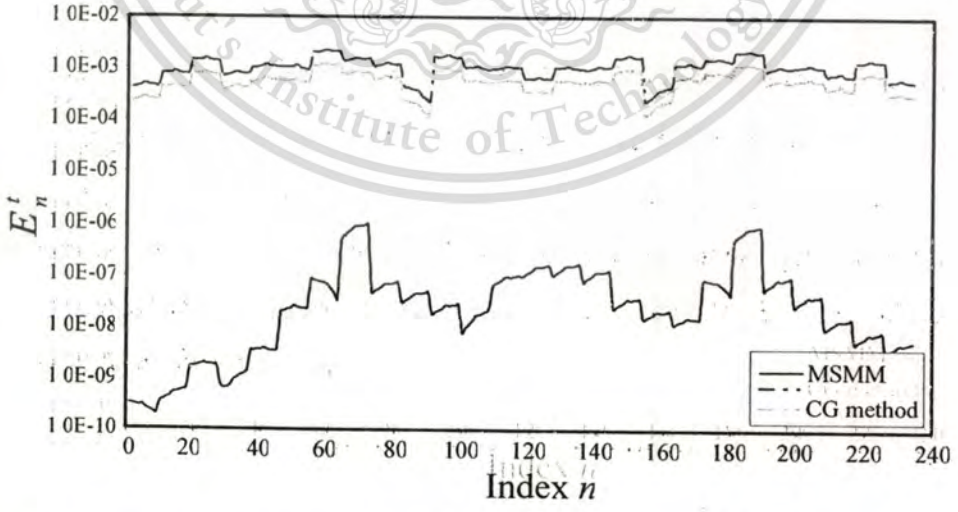

Figure 2.22 Errors in computing E_n^t for the final sweep of the CG method and the MSMM for the non-uniform collinear dipole antenna array of 26 elements.

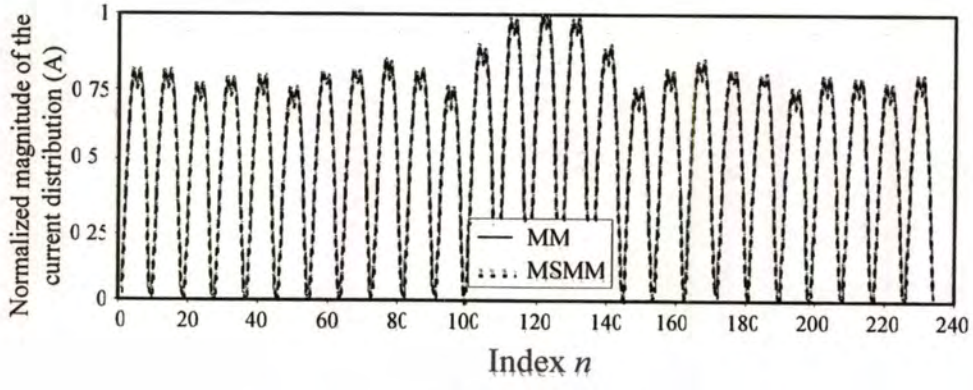

(a)

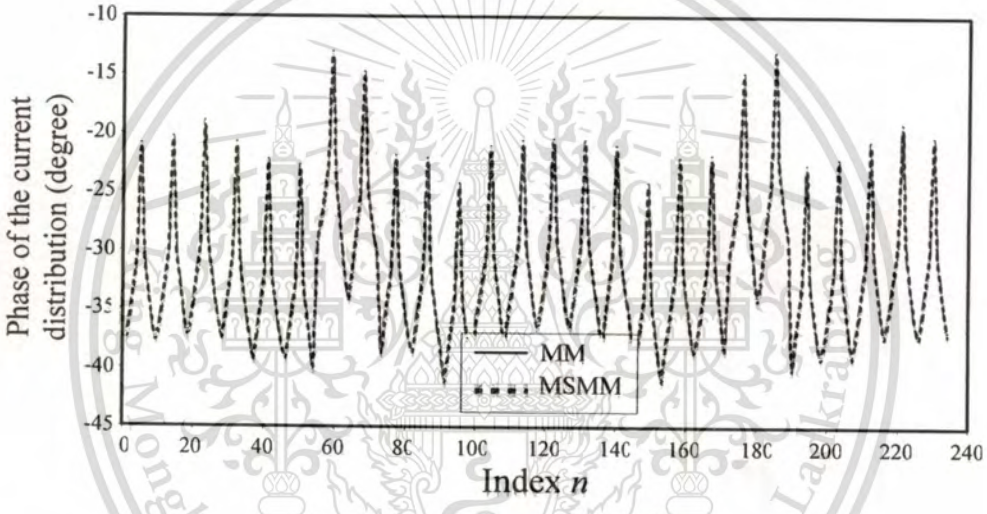

(b)

Figure 2.23 Normalized magnitude and phase of the current distribution of the non-uniform collinear dipole antenna array of 26 elements. (a) Normalized magnitude of the current distribution, and (b) Phase of the current distribution.

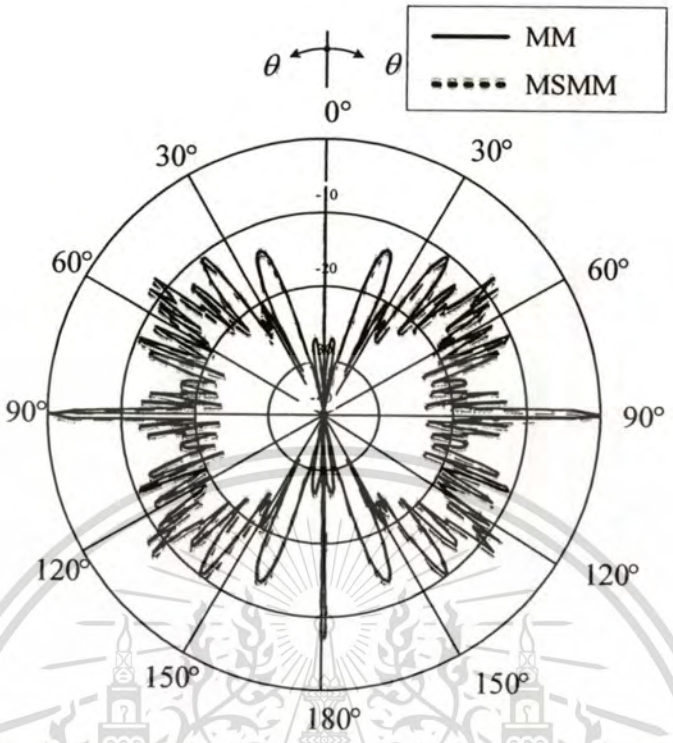

Figure 2.24 The *E*-plane radiation pattern of the non-uniform collinear dipole antenna array of 26 elements.

2.5.4 Non-uniform Planar Dipole Antenna Array

For non-uniform planar antenna arrays, the 24×24 planar dipole antenna array with non-uniform spacing [66] is analyzed. The antenna parameters of Fig. 2.8 are l = 0.5λ, and the distances between each element are shown in Table 2.2. Only 12 elements are shown due to its symmetrical structure. Five PWS basis functions for each element with radius of 0.005λ are employed resulting in N = 2,880, and each element is excited by 1 Volt at the center.

Table 2.2 Distance between each element of the 24×24 non-uniform planar dipole antenna array [66].

Parameters	Distance (λ)
$L_{x,1}, L_{z,1}$	0.375
$L_{x,2}, L_{z,2}$	0.125
$L_{x,3}, L_{z,3}$	0.620
$L_{x,4}, L_{z,4}$	0.370
$L_{x,5}, L_{z,5}$	0.750
$L_{x,6}, L_{z,6}$	0.785
$L_{x,7}, L_{z,7}$	1.050
$L_{x,8}, L_{z,8}$	1.245
$L_{x,9}, L_{z,9}$	1.545
$L_{x,10}, L_{z,10}$	1.890
$L_{x,11}, L_{z,11}$	2.386
$L_{x,12}, L_{z,12}$	2.893

Figure 2.25 shows the RMS error of the MSMM and the CG method. It is found that the MSMM requires 25 iterations, while the CG method requires 30 iterations to meet the convergence criterion of 10^{-2}. It is obvious that the MSMM converges faster than the CG method without any fluctuation for this non-uniform planar dipole antenna array. Note that the MSMM for the 24×24 non-uniform planar dipole antenna array requires more iterations than the 5×5 uniform planar dipole antenna array due to larger impedance matrix of the former one and the property of the impedance matrices. In addition, Fig. 2.26 shows the plot of E_n^t versus the index n for the final sweep (t = 14) for the 24×24 non-uniform planar dipole antenna array. It is found that the maximum error is less than 10^{-4}. Furthermore, the E-plane radiation pattern of the array is illustrated in Fig. 2.27. It is obvious that the MM and MSMM results are in excellent agreement, and these

results also agrees well with that in [66]. Furthermore, the MSMM is also applied to several planar dipole antenna arrays in free space, and it is found that it provides relatively good convergent results. Thus, it can be concluded that the MSMM can be effectively employed to analyze and design both uniform and non-uniform planar dipole antenna arrays in free space indeed.

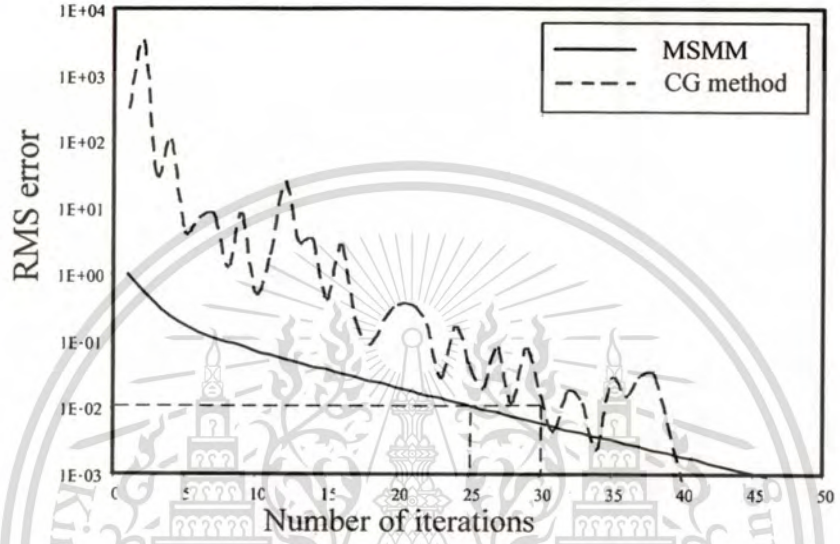

Figure 2.25 RMS errors of the MSMM with the sawtooth sweep and the CG methods for the 24×24 non-uniform planar dipole antenna array.

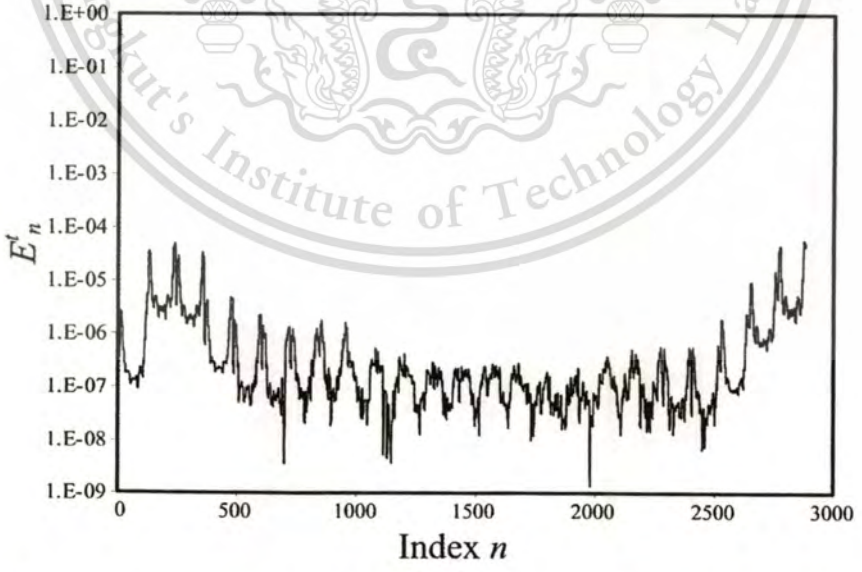

Figure 2.26 Error in computing E_n^t for the 24×24 non-uniform planar dipole antenna array for the final sweep ($t = 14$) of the MSMM.

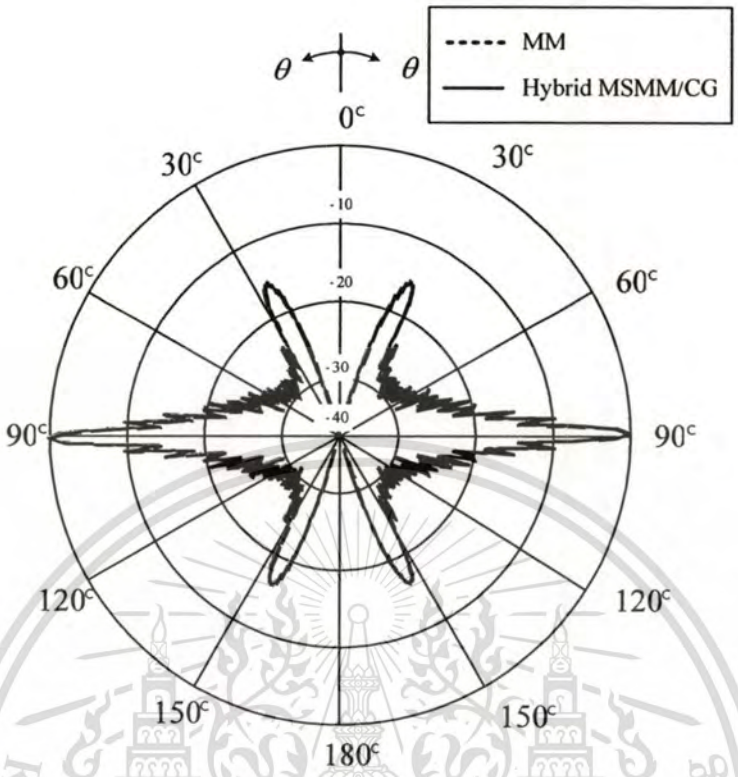

Figure 2.27 The *E*-plane radiation pattern of the 24×24 non-uniform planar dipole antenna array.

2.6 Conclusions

The MSMM can be effectively applied to analyze both uniform and non-uniform dipole antenna arrays with collinear and planar configurations in free space, which usually provides relatively fast convergence rate with additional physical insight into radiation/scattering mechanisms. The row and sawtooth MSMM sweeps are proposed in this chapter. It is found that the latter one is more efficient than the former one because the associated number of unknowns for each section of the row sweep is relatively large. In addition, the latter one exhibits faster convergent than the CG method without any fluctuation for the examples of interest. Furthermore, numerical results of the MSMM for both uniform and non-uniform dipole antenna arrays are in excellent agreement with those of the MM.

CHAPTER 3
HYBRID OF THE MSMM AND THE CONJUGATE GRADIENT METHOD (HYBRID MSMM/CG METHOD)

3.1 Introduction

This chapter presents an efficient hybrid algorithm of the MSMM and the CG method, called hybrid MSMM/CG method, for electrically large array problems. The MSMM is a stationary method, which provides physical insight into associated radiation and scattering mechanisms with relatively fast convergence rate [1], [24]. Note that the stationary method is simple to implement, but its convergence rate is limited by a class of impedance matrices. For the CG method, it is a non-stationary method based on sequential orthogonal vectors depending mainly on the iteration coefficients [28]-[29]. Therefore, the hybrid method can combine the advantages of the MSMM and the CG method to improve the convergence rate without sacrificing accuracy. For this method, the MSMM is employed first and than switch into the CG method when the convergence criterion is met. Note that the MSMM is employed as the initial value for the CG method. To show the improvement, electrically large uniform and non-uniform dipole antenna arrays in free space are analyzed by the hybrid MSMM/CG method [35]. These antenna arrays have several applications such as generating directional or contour beam for satellite, radar and microwave terrestrial systems [35].

3.2 Hybrid MSMM/CG Procedure

3.2.1 Multiple Sweep Method of Moments (MSMM)

The MSMM is an $O(N^2)$ recursive method, which has been introduced for solving electrically large problems; e.g., rough surface scattering and 3D radiation problems. For the MSMM in this chapter, the object of interest is split into P identical sections, and the currents on these sections are found in a *recursive fashion*. The first MSMM sweep includes dominant radiation/scattering mechanisms, and subsequent sweeps include

higher order mechanisms [1], [24]. The details of the MSMM procedure are discussed in Chapter 2.

3.2.2 Conjugate Gradient (CG) Method

The CG method is an efficient method for symmetrical positive definite systems. It is well-known as a non-stationary method. The method proceeds by generating vector sequences of iterated residuals corresponding to the iteration, and the search directions used in updating the iterations and residuals. This method requires two inner products to compute each iteration [28]-[29]. Like other iterative methods, the CG method is an $O(N^2)$ algorithm per iteration. The CG method is usually appropriate for general electrically large EM problems [28]-[29].

For the CG procedure, it starts by the initial guess for $\overline{I}$ by $\overline{I}_0$, which $\overline{I}_0$ is the zeros vector of the current. This suggests taking the first basis vector p_1 to be the negative of the gradient of function at $\overline{I} = \overline{I}_0$, this means we take $p_1 = \overline{V}$. The other vectors in the basis will be conjugate to the gradient, hence the name conjugate gradient method. Let r_k be the residual at the kth step as follow

$$r_k = \overline{V} - \overline{\overline{Z}}\overline{I}_k \tag{3.1}$$

Note that r_k is the negative gradient of function at $\overline{I} = \overline{I}_k$, so the gradient descent method would be to move in the direction r_k. It insists that the directions p_k be conjugate to each other. It also require the next search direction is built out of the current residue and all previous search directions, which is reasonable enough in practice. The conjugation constraint is an orthonormal-type constraint and hence the algorithm bears resemblance to Gram-Schmidt orthonormalization. This gives the following expression as

$$p_{k+1} = r_k - \sum_{i \le k} \frac{p_i^T \overline{\overline{Z}} r_k}{p_i^T \overline{\overline{Z}} p_i} p_i \tag{3.2}$$

$$I_{k+1} = I_k + \alpha_k + p_k + 1 \tag{3.3}$$

where

$$\alpha_{k+1} = \frac{p_{k+1}^T r_k}{p_{k+1}^T \bar{\bar{Z}} p_{k+1}} \tag{3.4}$$

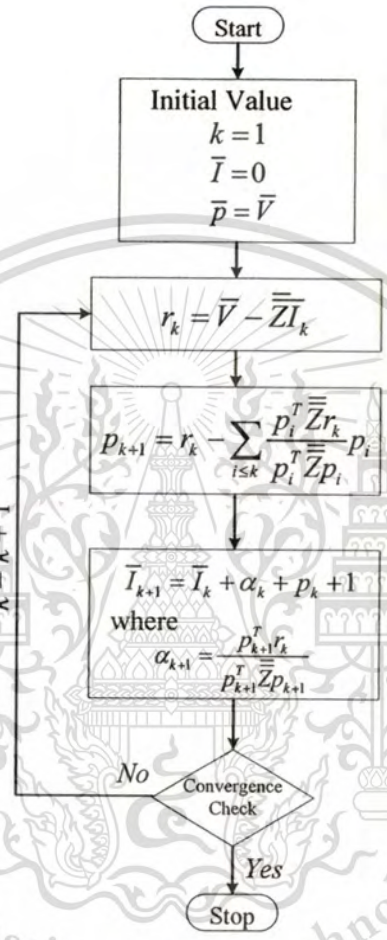

Figure 3.1 The flow chart of the CG method.

3.2.3 Hybrid MSMM/CG Method

To reduce the computational time of iterative methods for solving electrically large EM problems, an appropriate combination of the MSMM and the CG method is newly proposed as shown in Fig. 3.2. The hybrid MSMM/CG method starts with the MSMM and subsequently switches to the CG method when the preliminary solution satisfies the first convergence test, which is a preliminary test. One may also think that the MSMM is employed as a good initial guess for the CG method resulting in faster

convergence rate since the first few MSMM sweeps include dominant and higher order radiation/scattering mechanisms as pointed out earlier. Note that the total root mean square (RMS) error, E^t (2.34), is appropriately specified for the MSMM and the CG method of 10^{-1} and 10^{-2} corresponding to the convergence checks #1 and #2 in Fig. 3.2, respectively. It should be pointed out that the convergence check #2 is usually tighter than that of #1. In Fig. 3.2, the trend of convergence of the MSMM is also checked for monitoring the direction of the convergence. If the MSMM is not converge to the specified criterion, the result of the first MSMM sweep can still be used as a good initial guess for the CG method since it usually includes dominant radiation/scattering mechanisms. In addition, the residual error norm, R^t (2.35), is employed as a final convergence check. Once the $\overline{I}^t$ vector satisfies the convergence tests based on E^t, another convergence test based on R^t is employed to ascertain accuracy of the final solution. If $\overline{I}^t$ does not satisfy a specified accuracy criterion for R^t, the accuracy criteria for E^t used in the convergence checks #1 and #2 in Fig.3.2 are appropriately reduced further, and the two-step testing is started again until both error checks of $\overline{I}^t$ are satisfied.

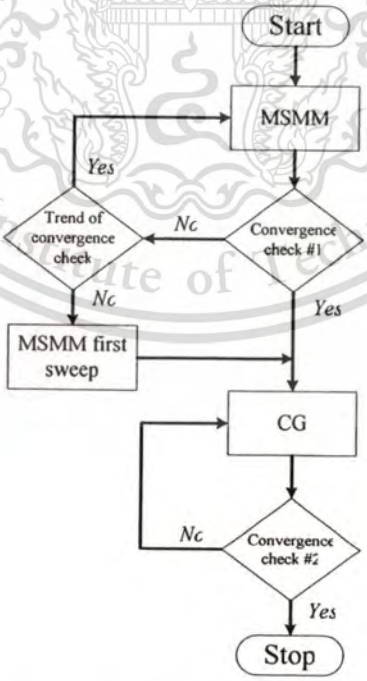

Figure 3.2 Hybrid MSMM/CG method.

3.3 Numerical Results

Numerical results are presented to demonstrate the accuracy and efficiency of the hybrid MSMM/CG method. Both uniform and non-uniform dipole antenna arrays with collinear and planar configurations are considered.

3.3.1 Uniform Collinear Dipole Antenna Array

A uniform collinear dipole antenna array of 100 elements is analyzed in this section. The array parameters of Fig. 2.6 are given as follows: $L_{z,k} = 0.5\lambda$ and $l = \lambda$. Five PWS basis functions for each dipole element with radius of 0.005λ are employed resulting in N = 500, and each element is excited by 1 Volt at the center. Figure 3.3 shows a comparison of RMS errors for the CG method, the MSMM, the hybrid MSMM/CG method, and the CG method with the 1st sweep MSMM as an initial guess. Note that the MSMM and the CG method initialize the unknown current vector $\overline{I}$ with the zero vector. From Fig. 3.3, the CG method converges within 3 iterations with the some fluctuation, the MSMM converges rapidly within 3 iterations, and the hybrid MSMM/CG method converges within 3 iterations (2 iterations for the MSMM and 1 iteration for the CG method). For the CG method with the 1st sweep MSMM as an initial guess, the method converges within 4 iterations. In addition, the error in computing E_n^t for the final iteration of the CG method and the hybrid MSMM/CG method for the antenna array are shown in Fig. 3.4. It is found that the error of the CG method is less than that of the hybrid MSMM/CG method, but both of them are less than the 10^{-5}.

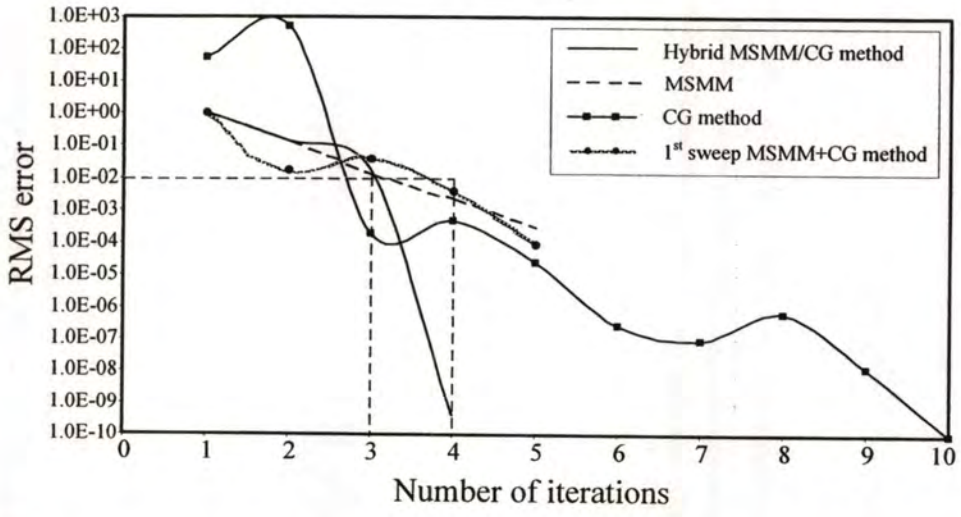

Figure 3.3 RMS errors of the CG method, the MSMM, the hybrid MSMM/CG method, and the CG method initialized with the 1st sweep MSMM for the uniform collinear dipole antenna array of 100 elements.

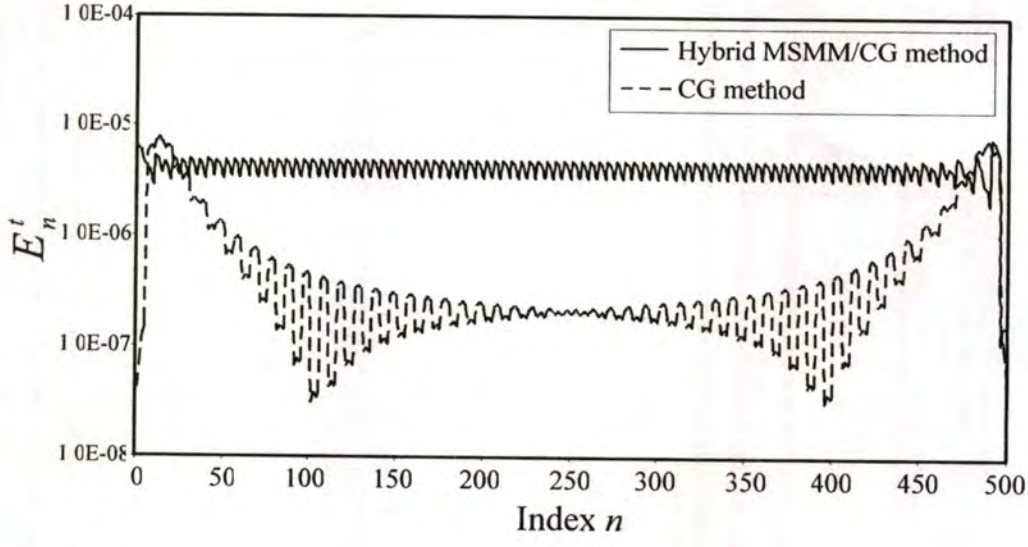

Figure 3.4 Errors in computing E_n^t for the final iteration of the CG and the hybrid MSMM/CG methods for the uniform collinear dipole antenna array of 100 elements.

Moreover, Fig. 3.5 shows the calculated current distribution for both normalized magnitude and phase of the antenna array compared between the MM and the hybrid MSMM/CG method. It is found that both methods are in excellent agreement. Figure 3.6

illustrates the *E*-plane radiation pattern of the antenna array. It is obvious that the MM and the hybrid MSMM/CG method yield identical radiation patterns as well.

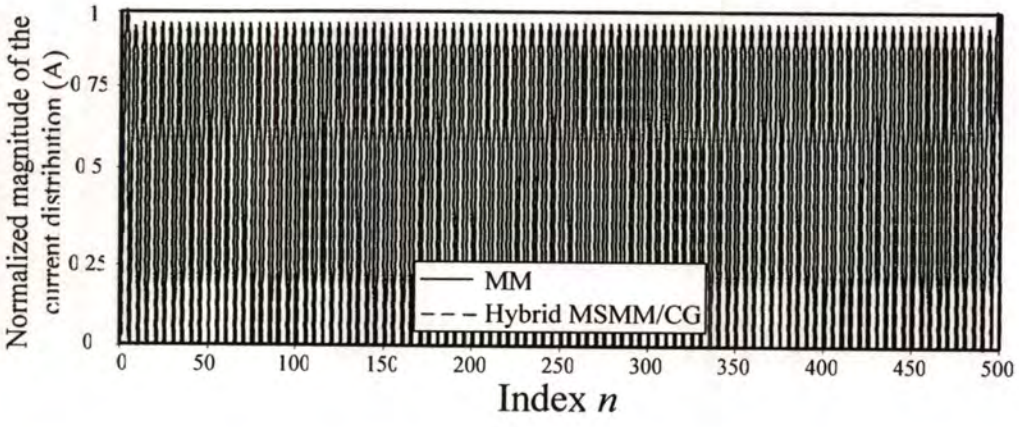

(a)

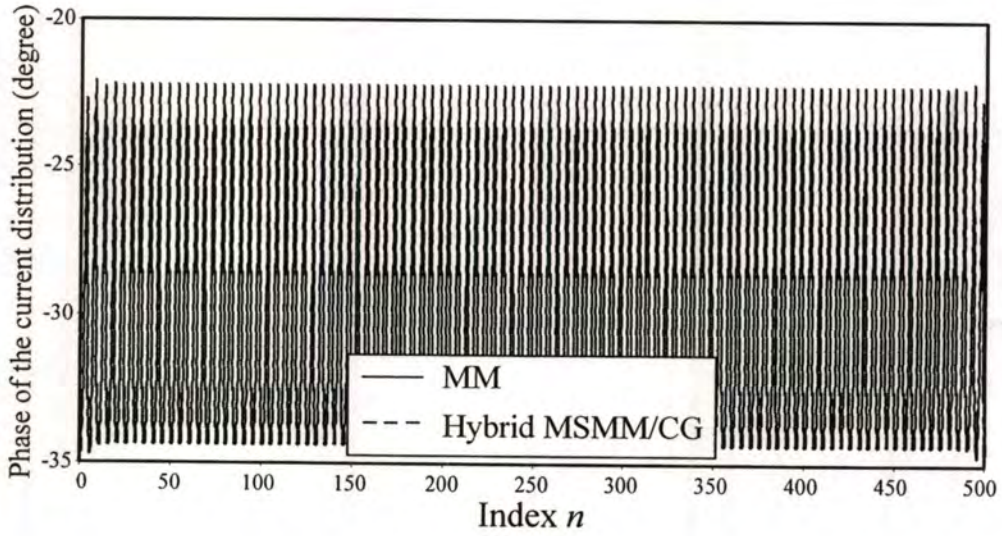

(b)

Figure 3.5 Current distribution of the uniform collinear dipole antenna array of 100 elements. (a) Normalized magnitude of the current distribution, (b) Phase of the current distribution.

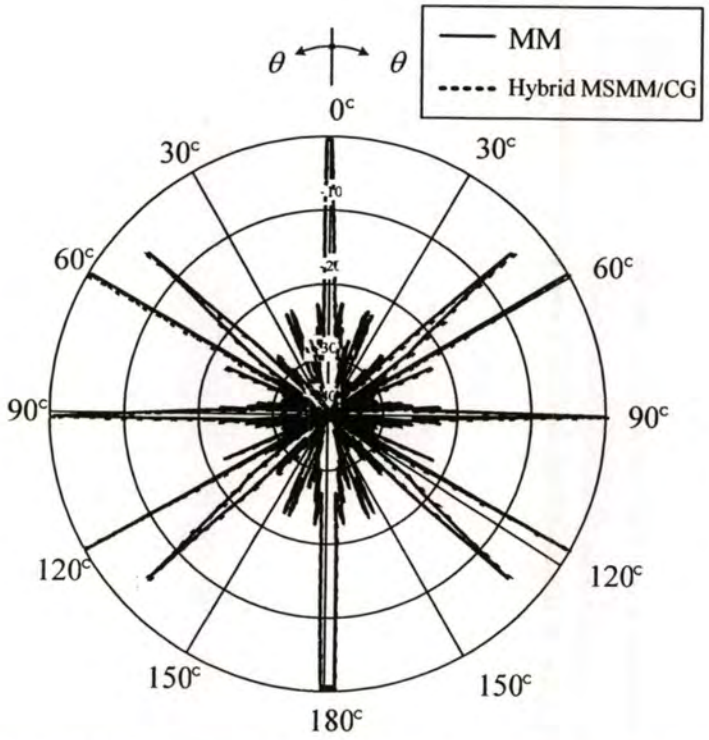

Figure 3.6 The *E*-plane radiation pattern of the uniform collinear dipole antenna array of 100 elements.

3.3.2 Uniform Planar Dipole Antenna Array

Consider the 21×21 uniform planar dipole antenna array in free space, where the array parameters of Fig. 2.8 are given as follows: $L_{x,j} = 0.3\lambda$, $L_{z,k} = 0.6\lambda$ and $l = 0.5\lambda$ with radius of 0.005λ. Five PWS basis functions for each element are used and each element is excited by 1 V at the center. Figure 3.7 shows a comparison of RMS errors for the CG method, the MSMM, the hybrid MSMM/CG method, and the CG method with the 1st sweep MSMM as an initial guess. Note that the MSMM and the CG method initialize the unknown current vector $\overline{I}$ with the zero vector. From Fig. 3.7, the MSMM and the CG method converge within 14 and 18 iterations, respectively. However, the hybrid MSMM/CG method provides the fastest convergence rate for this example; i.e., it requires only 7 iterations (6 iterations for the MSMM and 1 iterations for the CG method) to converge to the specified criterion. After the 6th iteration of the MSMM, the CG method rapidly converges within 1 iterations.

For the CG method initialized with the 1st sweep MSMM, it requires 18 iterations, which shows that the 1st sweep MSMM still be a good initial guess for the CG method because it includes the dominant radiation/scattering mechanisms.

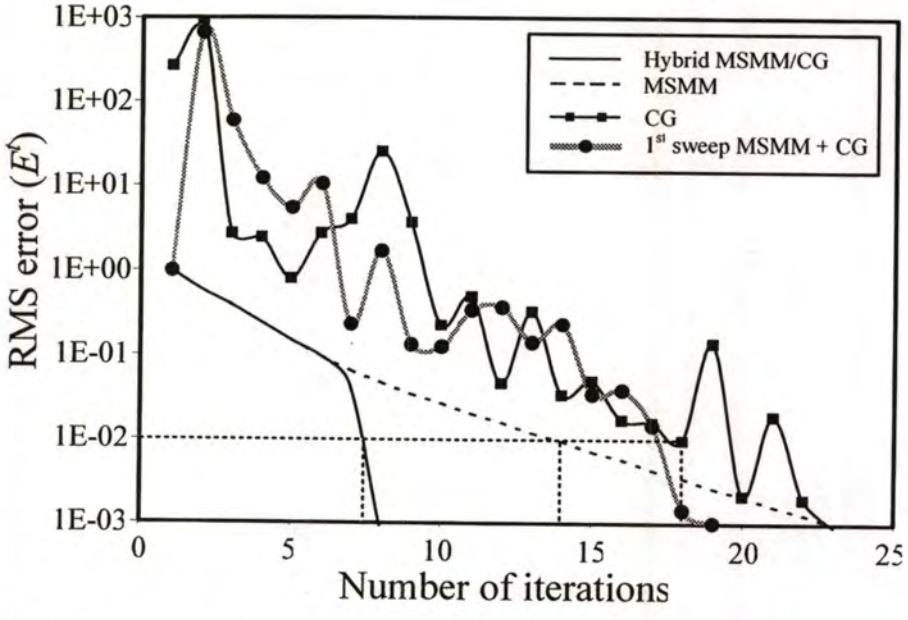

Figure 3.7 RMS errors of the CG method, the MSMM, the hybrid MSMM/CG method, and the CG method initialized with the 1st sweep MSMM for the 21×21 uniform planar dipole antenna array.

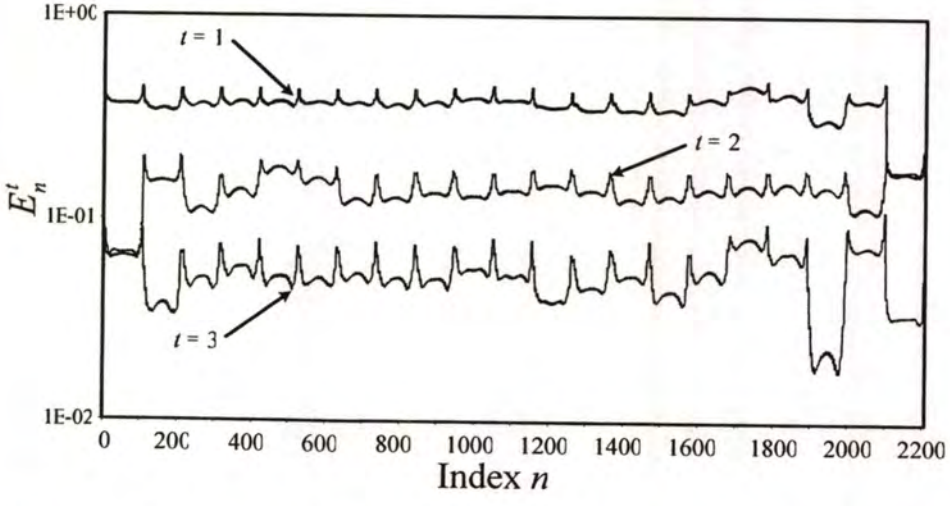

Figure 3.8 Errors in computing E_n^t for the sweep t = 1 to 3 of the hybrid MSMM/CG method.

Figure 3.8 shows the plot of E_n^t (2.37) versus the index n for the sweep $t = 1$ to 3. Note that the sweep $t = 1$ error starts with 0.384 at the left edge. The sweep $t = 2$ error at the right edge begins with 0.219, and then drops to 0.086 at the left edge. As the sweeps continue, the overall error tends to drop, and is reduced to 0.05 at the right edge by the end of the sweep $t = 3$. Fig. 3.8 illustrates that the first few MSMM sweeps can be employed as good initial guesses for the CG method due to the fact they include dominant and higher order radiation/scattering mechanisms.

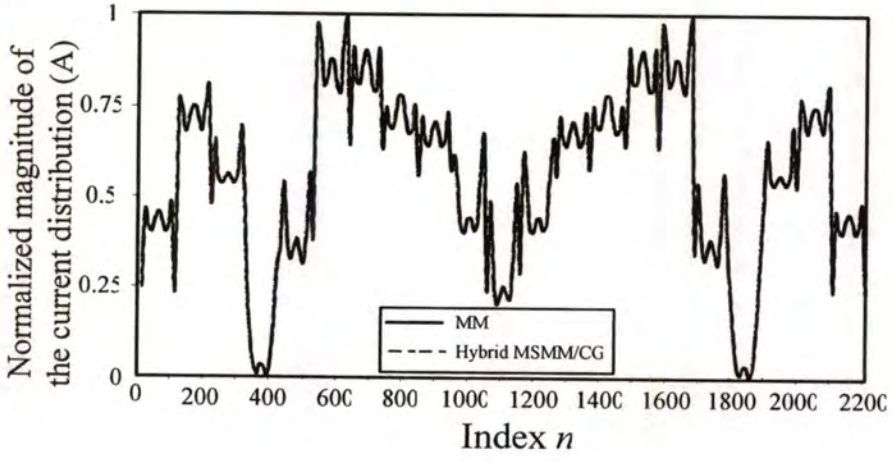

(a)

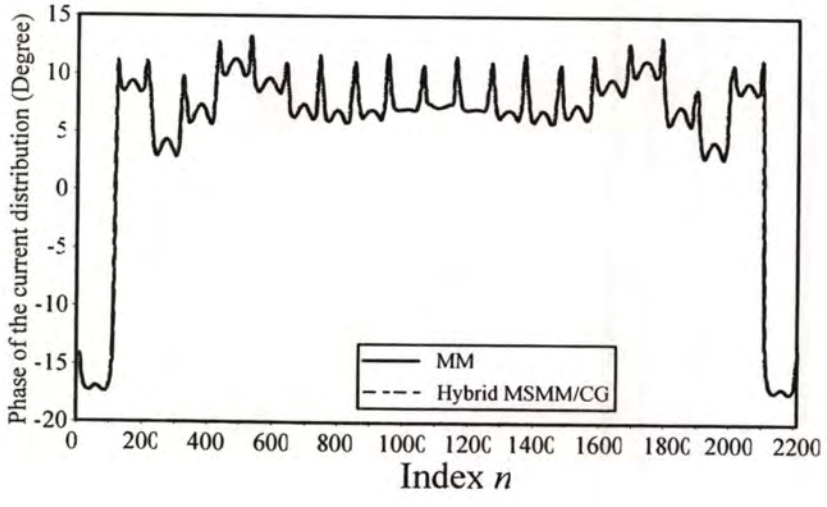

(b)

Figure 3.9 Current distribution of the 21×21 uniform planar dipole antenna array. (a) Normalized magnitude of the current distribution, (b) Phase of the current distribution.

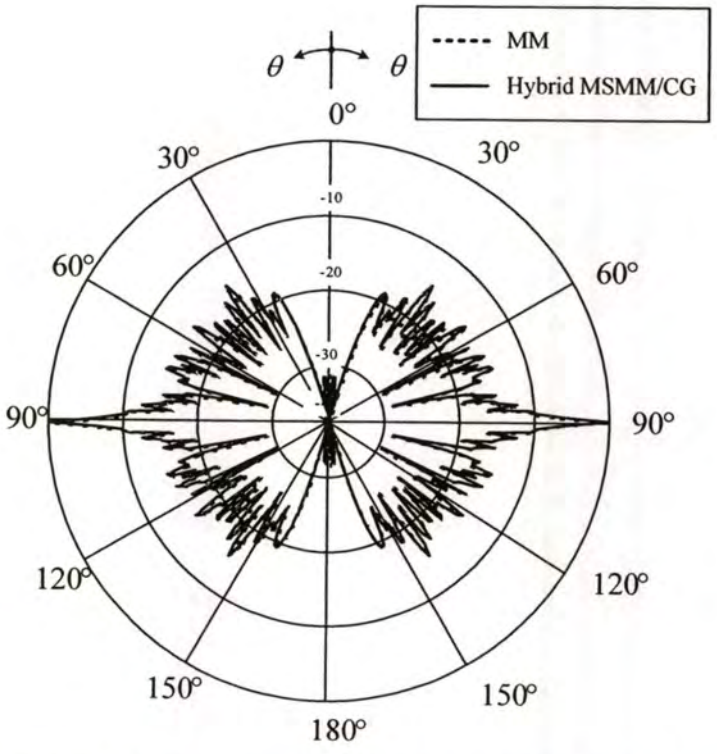

Figure 3.10 The *E*-plane radiation pattern of the 21×21 uniform planar dipole antenna array.

In addition, Fig. 3.9 shows the calculated current distribution for both normalized magnitude and phase of the 21×21 uniform planar dipole antenna array compared between the MM and the hybrid MSMM/CG method. It is found that both methods are in excellent agreement. Moreover, Fig. 3.10 illustrates the *E*-plane radiation pattern of the dipole antenna array. It is obvious that the MM and the hybrid MSMM/CG method yield identical radiation patterns.

3.3.3 Non-uniform Collinear Dipole Antenna Array

This section presents numerical results for a non-uniform collinear dipole antenna array in free space. For non-uniform collinear dipole antenna array of 26 elements, the array parameters of Fig. 2.6 are given as $l = 0.5\lambda$ with radius of 0.005λ, and the distance between each element are given in Table. 3.1. Only 13 elements are shown due to its symmetrical structure. Nine PWS basis functions for each element are used resulting in $N = 234$, where each element is excited by 1 Volt at the center. Figure 3.11 shows a

comparison of RMS errors for the CG method, the MSMM, the hybrid MSMM/CG method, and the CG method with the 1st sweep MSMM as an initial guess. Note that the MSMM and the CG method initialize the unknown current vector $\overline{I}$ with the zero vector. From Fig. 3.11, the MSMM and the CG method converge within 5 iterations. However, the hybrid MSMM/CG method provides the fastest convergence rate for this example; i.e., it requires only 4 iterations (2 iterations for the MSMM and 2 iterations for the CG method) to converge to the specified criterion. After the 2th iteration of the MSMM, the CG method is rapidly converged within 2 iterations. In addition, Fig. 3.12 shows the plot of E_n^t versus the index n for the final sweep ($t = 4$) for the antenna array. It is found that the maximum error is approximately less than 10^{-3}.

Table 3.1 Distances between each element of the non-uniform collinear dipole antenna array of 26 elements.

Parameters	Distance (λ)
$L_{z,1}$	1.406
$L_{z,2}$	1.177
$L_{z,3}$	1.005
$L_{z,4}$	1.392
$L_{z,5}$	0.739
$L_{z,6}$	1.036
$L_{z,7}$	0.233
$L_{z,8}$	1.398
$L_{z,9}$	0.522
$L_{z,10}$	0.892
$L_{z,11}$	0.732
$L_{z,12}$	0.423
$L_{z,13}$	0.424

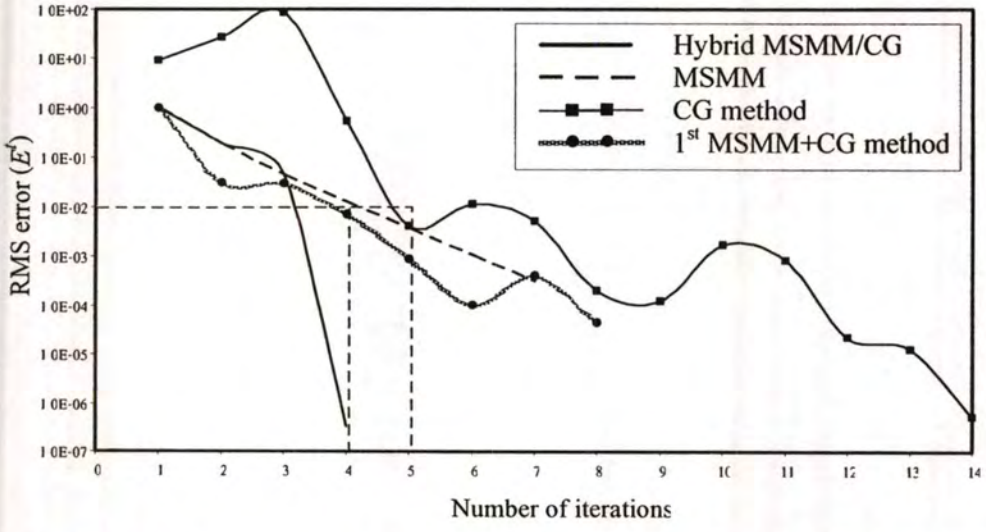

Figure 3.11 RMS errors of the CG method, the MSMM, the hybrid MSMM/CG method, and the CG method initialized with the 1st sweep MSMM of the non-uniform collinear dipole antenna array of the 26 elements.

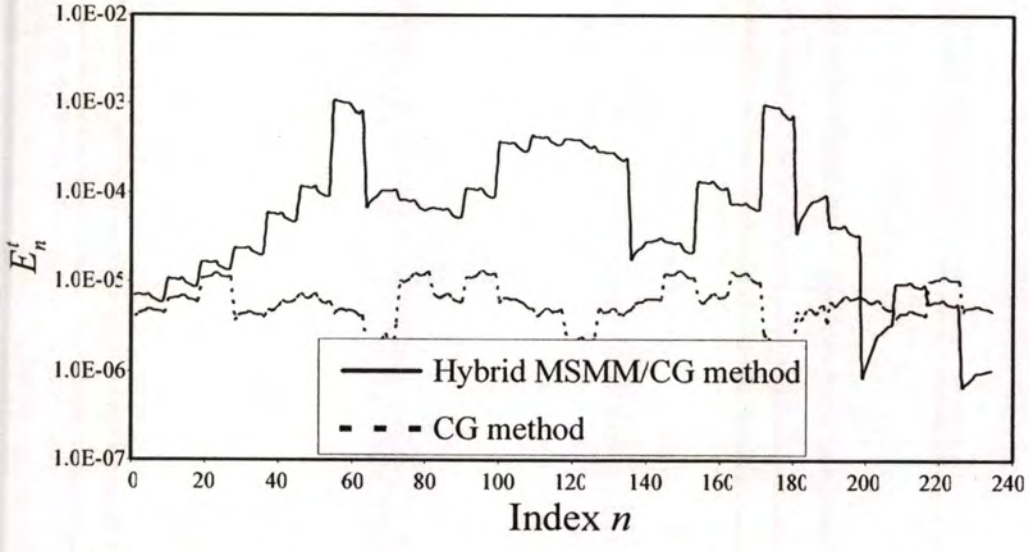

Figure 3.12 Error in computing E_n^t for the final iteration of the CG method and the hybrid MSMM/CG method for the non-uniform collinear dipole antenna array of 26 elements.

Furthermore, the current distribution and the *E*-plane radiation pattern of the array are illustrated in Figs. 3.13 and 3.14, respectively. It is obvious that the MM and MSMM results are in excellent agreement.

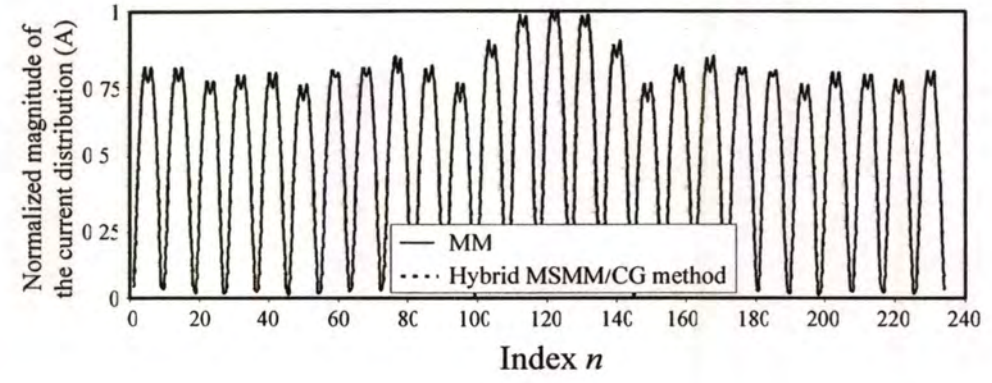

(a)

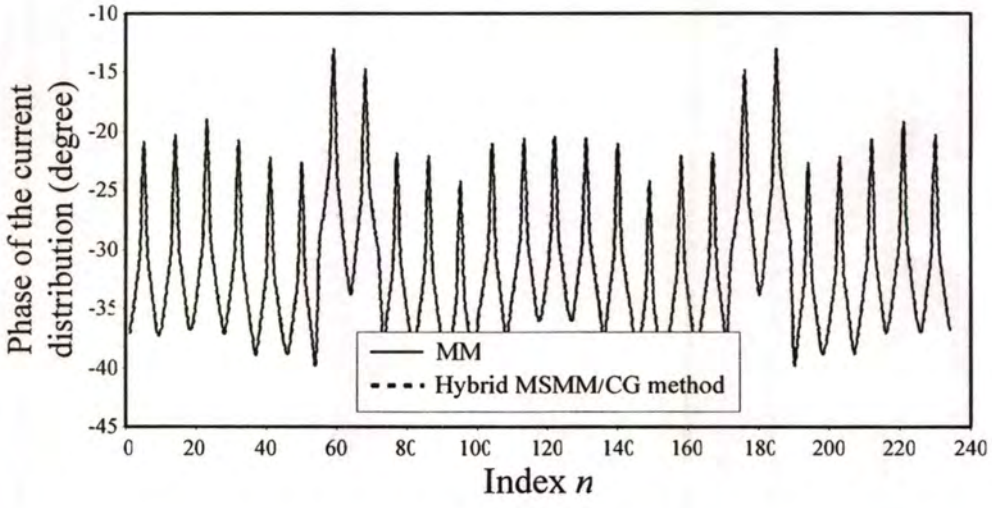

(b)

Figure 3.13 Normalized magnitude and phase of the current distribution of the non-uniform planar dipole antenna array of the 26 elements. (a) Normalized magnitude of the current distribution, and (b) Phase of the current distribution.

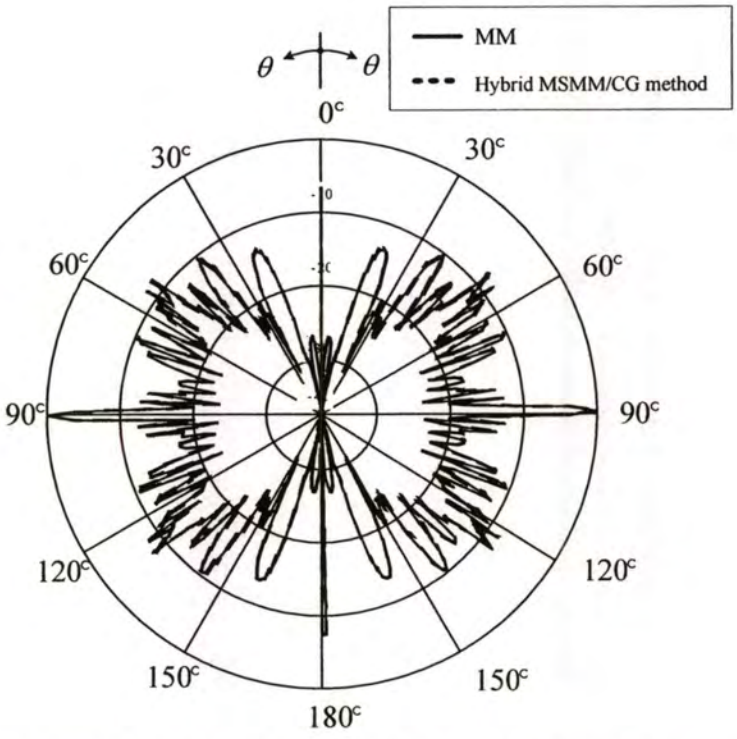

Figure 3.14 The *E*-plane radiation pattern of the non-uniform collinear dipole antenna array of the 26 elements.

3.3.4 Non-uniform Planar Dipole Antenna Array

In this section, a non-uniform planar dipole antenna array of 24×24 elements in [66] is analyzed, which was used to reduce the sidelobe level. The array parameters of Fig. 2.8 are given as follows: $l = 0.5\lambda$ with radius of 0.005λ, and the distances between each element are shown in Table 3.2. Only 12 elements are shown due to its symmetrical structure. Five PWS basis functions for each element are employed resulting in N = 2,880, and each element is excited by 1 Volt at the center.

Table 3.2 Distances between each element of the 24×24 non-uniform planar dipole antenna array.

Parameters	Distance (λ)
$L_{x,1}, L_{z,1}$	0.375
$L_{x,2}, L_{z,2}$	0.125
$L_{x,3}, L_{z,3}$	0.620
$L_{x,4}, L_{z,4}$	0.370
$L_{x,5}, L_{z,5}$	0.750
$L_{x,6}, L_{z,6}$	0.785
$L_{x,7}, L_{z,7}$	1.050
$L_{x,8}, L_{z,8}$	1.245
$L_{x,9}, L_{z,9}$	1.545
$L_{x,10}, L_{z,10}$	1.890
$L_{x,11}, L_{z,11}$	2.386
$L_{x,12}, L_{z,12}$	2.893

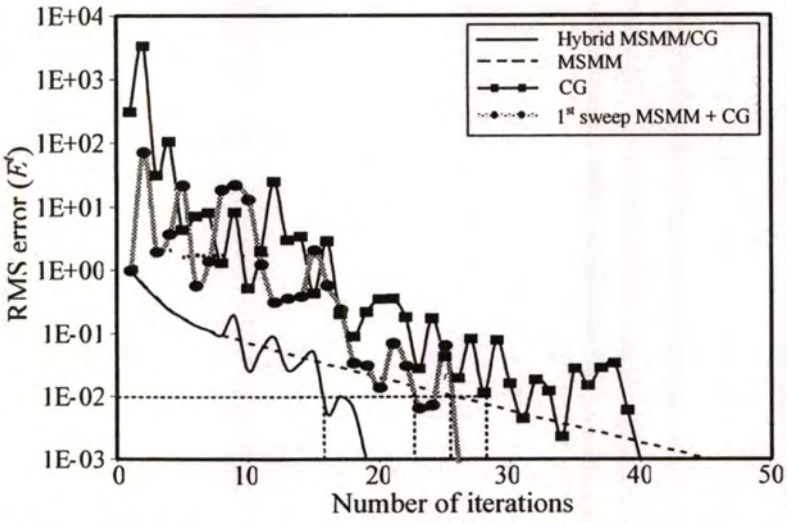

Figure 3.15 RMS errors of the CG method, the MSMM, the hybrid MSMM/CG method, and the CG method initialized with the 1st sweep MSMM for the 24×24 non-uniform planar dipole antenna array.

Figure 3.15 shows a comparison of the RMS errors of all methods for the 24×24 non-uniform planar dipole antenna array. Note that the hybrid MSMM/CG method still provides the fastest convergence rate, which requires only 19 iterations (8 iterations for the MSMM and 11 iterations for the CG method). The error in computing E_n^t of the hybrid MSMM/CG method compared with the MM for the non-uniform array is shown in Fig. 3.16. It is found that the maximum error is less than 10^{-4}. In addition, Fig. 3.17 shows the *E*-plane radiation pattern of the non-uniform planar dipole antenna array. It is obvious that the MM and the hybrid MSMM/CG method yield identical radiation pattern as well.

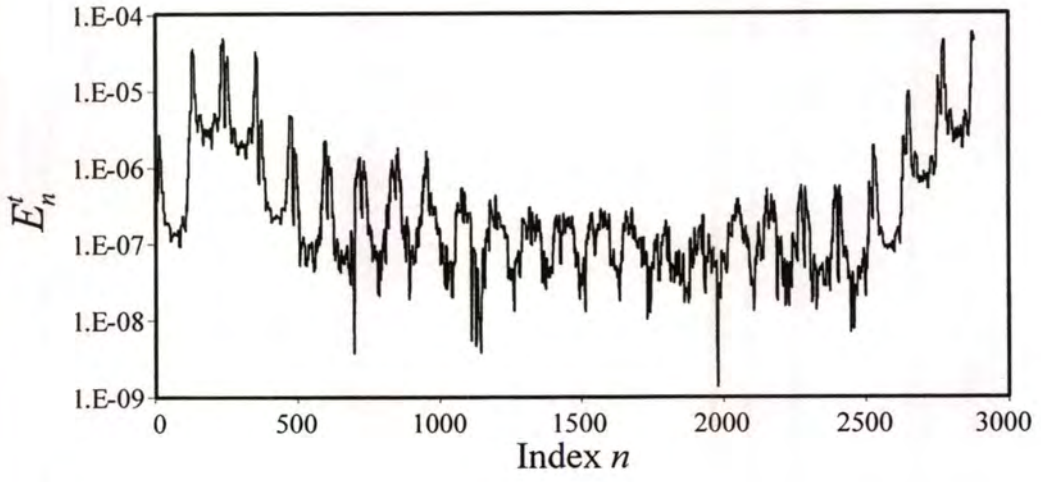

Figure 3.16 Error in computing E_n^t for the 24×24 non-uniform planar dipole antenna array for the final sweep of the hybrid MSMM/CG method.

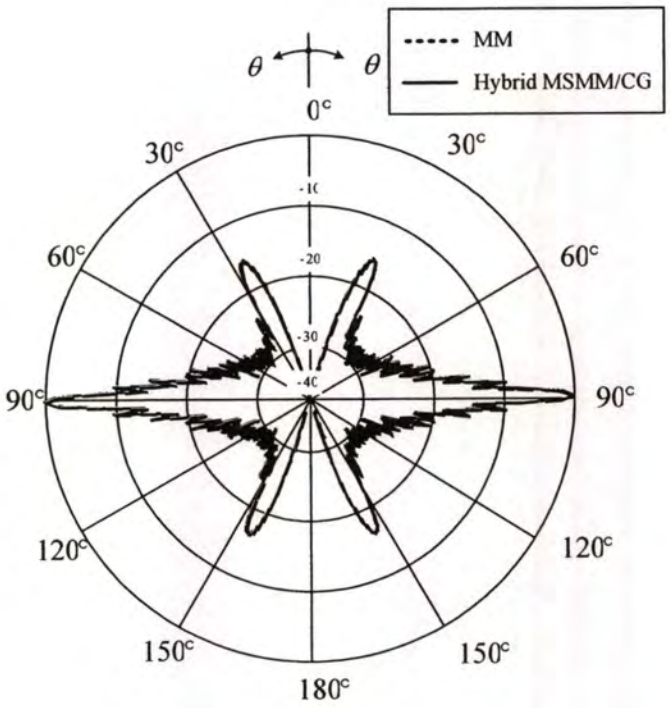

Figure 3.17 The *E*-plane radiation pattern of the 24×24 non-uniform planar dipole antenna array.

3.4 Conclusions

The hybrid MSMM/CG method can be effectively applied to analyze electrically large uniform and non-uniform dipole antenna arrays with collinear and planar configurations in free space with relatively fast convergence rate. For collinear dipole antenna array, the hybrid MSMM/CG method shows fastest convergence rate compared with the conventional MSMM and the CG method especially for non-uniform collinear dipole antenna array. Compared with the conventional MSMM and the CG methods for two considered arrays, the hybrid method provides the fastest convergence rate. It requires only 8 iterations (6 iterations for the MSMM and 2 iterations for the CG method) and 19 iterations (8 iterations for the MSMM and 11 iterations for the CG method) for the 21×21 uniform and 24×24 non-uniform planar dipole antenna arrays, respectively. Several numerical results are presented to validate the hybrid approach. It is found that the results of the hybrid MSMM/CG method are in excellent agreement with those of the MM. It shows that the hybrid MSMM/CG method can improve the convergence rate of solutions without sacrificing accuracy especially for non-uniform antenna array.

CHAPTER 4
HYBRID MSMM/CG METHOD WITH THE SPECTRAL ACCELERATION (SA) ALGORITHM

4.1 Introduction

The antenna array plays an important role in many EM applications including generating directional or contour beam for satellite, radar and microwave terrestrial systems. Due to their large geometry, complexities and difficult to obtain an accurate description of EM radiation fields for large-scale structure, several efficient numerical methods have been proposed recently such as FMM, MLFMM, FFT, DFT and SA algorithm.

The SA algorithm, as another fast technique, can be easily incorporated into other iterative techniques; i.e., the FB method, CG method, and MSMM by performing only matrix-vector multiplication without updating currents. An extremely efficient and accurate iterative MM based on the SA algorithm has been developed for the computation of scattering and radiation from 1-D, two-dimensional (2-D) and three-dimensional (3-D) vector wave problems, respectively. In the SA algorithm, the most important issue is to determine the appropriate SA parameters which include the tilt angle (δ) of the deformed contour, the domain of integration, and the integration step size. These parameters are derived based on the assumption that the outermost possible saddle point along the real axis in the complex angular plane is small as discussed in detail in [60].

This chapter is organized as follows. The SA basic theory is discussed in detail in Section 4.2. In Section 4.3, the genetic algorithm (GA) optimization is proposed to find the optimum SA integration parameters compared with the conventional technique. Some numerical results are presented in Section 4.4, and conclusions can be found in Section 4.5.

4.2 The SA Theory

The SA algorithm has been shown to be an extremely efficient and accurate iterative MM technique for the computation of the antenna arrays [60]. The SA

algorithm is employed to rapidly compute interaction between widely separated points in the conventional FB method [52], [54], and [60], and is based on a single spectral representation of source currents and the associated Green's function. In this section, the SA algorithm for antenna array is discussed in detail. The SA algorithm for this case involves a double spectral integral representation of source currents and the 3D free space scalar Green's function. The coupling between two spectral variables makes the problem more challenging, and efficiency improvements obtained for antenna arrays.

In the SA algorithm, the contributions to a receiving element on the dipole antenna arrays are separated into strong and weak source contributions. The former is calculated by the standard matrix vector multiplication, while the latter is computed by using the SA algorithm involving the spectral domain representation of the 3D scalar free-space Green's function. In the hybrid MSMM/CG method, the SA algorithm is incorporated into the MSMM and the CG methods to accelerate its computational time, called the MSMM/SA and CG/SA methods, respectively. For the MSMM/SA and the CG/SA methods, the antenna array can be separated into strong and weak contributions as shown in Fig. 4.1. Note that D_z is the total size of the array in the z-direction and L_s is a neighborhood distance in the z-direction within which interactions between points are classified as strong interactions and outside of which interactions are classified as weak interactions. In Fig. 4.1, N_z is the extended number of elements from the p^{th} section to define the strong region for its left and right sides. For the MSMM/SA method, the weak region is separated into two regions. When the MSMM sweeps from $p = 1$ to P, the weak region 1 includes currents from the present sweep, and the weak region 2 includes currents from the previous sweep. They are alternated when the MSMM sweeps from $p = P$ to 1. For the CG method, it has only weak region 1 for the SA algorithm, and the procedure is process as in the point.

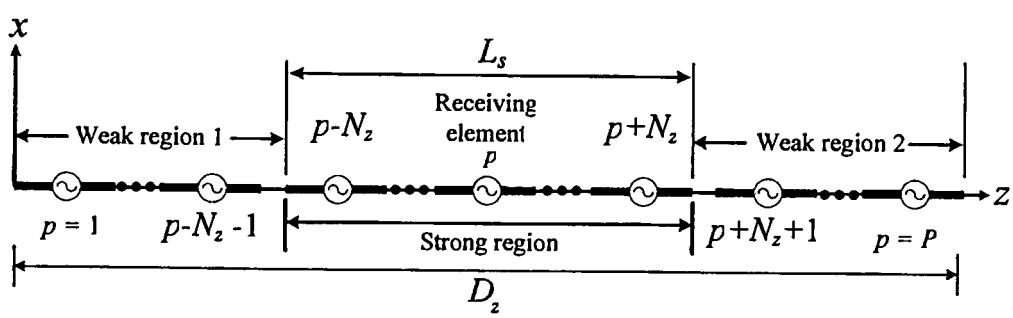

Figure 4.1 A collinear dipole antenna array analyzed by using the SA algorithm.

In the SA algorithm, the spectral domain representation of the $G(\bar{r},\bar{r}')$ is employed in (4.1) for $z-z'>0$ as follows:

$$\left(\frac{\partial^2}{\partial z^2}+k_0^2\right)G(\bar{r},\bar{r}')=\frac{-j}{8\pi^2}\int_{C_{k_x}}\int_{C_{k_y}}dk_x dk_y(-k_z^2+k^2)\left[\frac{e^{-j\left[k_x(x-x')+k_y(y-y')+k_z(z-z')\right]}}{k_z}\right], \tag{4.1}$$

where $k_z=(k^2-k_x^2-k_y^2)^{1/2}$, $\bar{r}$ is an observation point, $\bar{r}'$ is a source point, C_{k_x} and C_{k_y} are the original contours of integration on the real axes in the complex k_x and k_y planes, respectively. Note that (4.1) can be similarly evaluated for $z-z'<0$ [60]. Substituting (4.1) into the left-hand side (LHS) of (2.17) and interchanging the spatial and spectral integrations yield

$$\int_l \bar{I}_z(z')\left(\frac{\partial^2}{\partial z^2}+k_0^2\right)G(\bar{r},\bar{r}')dz'=\frac{-j}{8\pi^2}\int_{C_{k_x}}\int_{C_{k_y}}dk_x dk_y\frac{\bar{F}(\bar{r},k_x,k_y)}{k_z}, \tag{4.2}$$

where

$$\bar{F}(\bar{r},k_x,k_y)=\int_l \bar{I}_z(z')(-k_z^2+k^2)\left[\frac{e^{\left\{-j\left[k_x(x-x')+k_y(y-y')+k_z(z-z')\right]\right\}}}{k_z}\right]dz'. \tag{4.3}$$

In (4.3), $\bar{F}(\bar{r},k_x,k_y)$ is called the complex vector radiation function, which can be computed *recursively* using the *phase shifting process* [60]. This recursive computation of $\bar{F}(\bar{r},k_x,k_y)$ and the appropriate contour deformation make the SA algorithm extremely efficient; i.e., an $O(N)$ algorithm. The most important property of $\bar{F}^{(l)}(\bar{r},k_x,k_y)$ in the SA approach is that it can be computed from current in the weak region in a recursive manner. The radiation function $\bar{F}^{(l)}(\bar{r},k_x,k_y)$ in the FS direction can be recursively computed through a "phase shifting" process as follows. For $n>p+N_z$;

$$\bar{F}^{(l)}(\bar{r}_{(n,l)},k_x,k_y)=\bar{F}^{(l)}(\bar{r}_{(n-1,l)},k_x,k_y)e^{jw}, \tag{4.4}$$

and

$$\psi = \bar{k} \bullet [\bar{r}_{(n,1)} - \bar{r}_{(n-1,1)}]. \tag{4.5}$$

The topology of two coupled complex k_x and k_y planes totally depends on the order of integration in (4.1). For the 2D SA formulation in this chapter, the integration on k_y is performed first, and then follow by the integration on k_x; i.e. the spectral integral representation of $G(r,r')$ in (4.1) is rearranged as follows:

$$G(\bar{r},\bar{r}') = \frac{-j}{8\pi^2} \int_{C_{k_x}} dk_x e^{-jk_x(x-x')} \int_{C_{k_y}} dk_y \frac{e^{-j[k_x(z-z')+k_y(y-y')]}}{k_z}. \tag{4.6}$$

It is obvious from the above equation that the spectral variable k_y is dependent on k_x through k_z resulting in the dependence of the topology in the complex k_y plane on the topology in the complex k_x planes as discussed in [60]. It should be pointed out that another order of integration (i.e. integrating on k_x first and then integrating on k_y) is also possible. To gain numerical efficiency when performing the numerical contour integration, the original contours C_{k_x} and C_{k_y} are deformed to the new contours $C_{\delta_{k_x}}$ and $C_{\delta_{k_y}}$ respectively as shown in [60]. This is possible since there are no singularities in between the original and deformed contours. These contour deformations yield smaller integral involving $\bar{F}^{(i)}(\bar{r},k_x,k_y)$. This is due to the fact that the function $\bar{F}^{(i)}(\bar{r},k_x,k_y)$ is relatively smooth and localized in the complex k_x and k_y planes along the deformed complex contours, as illustrated via numerical example later in [60], where $\bar{F}^{(i)}(\bar{r},k_x,k_y)$ is highly oscillatory along the real axes, especially as the size of the weak region increases. These contour deformations are necessary to make the 2D SA method an $O(N)$ algorithm as well as the recursive property of $\bar{F}^{(i)}(\bar{r},k_x,k_y)$. Without these contour deformations, it is required to increase the sampling rate to evaluate the double spectral integral involving $\bar{F}^{(i)}(\bar{r},k_x,k_y)$ accurately as the size of the weak region increases due to more oscillation of $\bar{F}^{(i)}(\bar{r},k_x,k_y)$ along the original contours C_{k_x} and C_{k_y}. Increasing the

sampling rate as the surface size increases makes the efficiency of the 2D SA method degrade considerably. Thus, it is emphasized that both the recursive property of $\overline{F}^{(i)}(\overline{r},k_x,k_y)$ and contour deformations are necessary in the 2D SA algorithm.

Advantageous deformed contours $C_{\delta_{k_x}}$ and $C_{\delta_{k_y}}$ can be determined by considering the spectral integral representation of $G(\overline{r},\overline{r}')$. (4.6) can be rewritten as [60]

$$G(\overline{r},\overline{r}')=\frac{-j}{8\pi^2}\int_{C_{\delta_{k_x}}} dk_x e^{-jk_x(x-x')}\int_{C_{\delta_{k_y}}} dk_y \frac{e^{-j[k_x(z-z')+k_y(y-y')]}}{k_z} \tag{4.7}$$

It can be seen from (4.7) that the two spectral variables k_x and k_y are coupled through $k_z=(k^2-k_y^2-k_x^2)^{1/2}$. As k_x changes along the contour $C_{\delta_{k_x}}$, the topology in the complex k_y plane is modified.

Once the deformed contours $C_{\delta_{k_x}}$ and $C_{\delta_{k_y}}$ are known. The numerical integration is employed to solve (4.7). For convenience when performing the numerical double contour integration, the double contour integral of (4.7) is discretized and mapped to the real axis according to the following mappings: $dk_x \to \Delta k_x e^{-j\delta_{k_x}}$, $k_x \to k_{x_p}=p\Delta k_x e^{-j\delta_{k_x}}$ for $p=-P,...,P$, $dk_y \to \Delta k_y e^{-j\delta_{k_y}}$, and $k_y \to k_{y_q}=q\Delta k_y e^{-j\delta_{k_y}}$ for $q=-Q_p,...,Q_p$. where Δk_x and Δk_y are the integration step size in the complex k_x and k_y planes respectively, and $2P+1$ is the number of plane waves in the k_x plane. It is noted that Q_p depends on p and it can be shown that $Q_{-p}=Q_p$. Thus, for a fixed k_x (p is fixed), the number of plane waves in both planes $Q_{TOT,x}$ is given by

$$Q_{TOT,x}=\sum_{p=-P}^{P}(2Q_p+1), \tag{4.8}$$

where $P=\frac{k_{x,\max}}{\Delta k_x}+1$ and $Q_p=\frac{\mathrm{Re}\left[k_{y,\max}\right]}{\Delta k_y}+1$. Using the above mapping, the discretized version of (4.7) can be written as:

$$G(\bar{r},\bar{r}')=\frac{1}{8\pi^2}\Delta\Omega\sum_{p=-P}^{P}\sum_{q=-Q_p}^{Q_p}\frac{W(k_{x_p},k_{y_q})\left[F^{(t)}\left(r,k_{x_p},k_{y_q}\right)\right]}{k_{z_{p,q}}}e^{-i\delta_{k_x}}e^{-i\delta_{k_y}}, \quad (4.9)$$

where $k_{z_{p,q}}=\left(k^2-k_{y_q}^2-k_{x_p}^2\right)^{1/2}$, $\Delta\Omega=\Delta k_y\Delta k_x$ and $W(k_{x_p},k_{y_q})$ is a weighting function for numerical integration. Various integration parameters in the k_x and k_y planes are given as follows: [60]

$$k_{x,\max}=\begin{cases}\sqrt{\frac{20k}{L_s}} & ,\tan^{-1}\left(\frac{\Delta x_{\max}}{L_s}\right)\le 0.1\\ k_{x,S_{\max}}+k_{x,tail} & ,\tan^{-1}\left(\frac{\Delta x_{\max}}{L_s}\right)>0.1\end{cases}, \quad (4.10)$$

$$\mathrm{Re}\left[k_{y,\max}\right]=\begin{cases}\sqrt{\frac{20k}{L_s}} & ,\tan^{-1}\left(\frac{D_y}{L_s}\right)\le 0.1\\ \mathrm{Re}\left[k_{y,S_{\max}}\right]+k_{y,tail} & ,\tan^{-1}\left(\frac{Dy}{L_s}\right)>0.1\end{cases}, \quad (4.11)$$

and $k_{x,S_{\max}}=\frac{k\Delta x_{\max}}{R_{xz}}$, $\Delta k_x=\frac{1}{22}\sqrt{\frac{C_x k}{L_s}}$, $k_{y,S_{\max}}=\frac{\kappa D_y}{R_{zy}}$, and $\Delta k_y=\frac{1}{22}\sqrt{\frac{C_y k}{R_{zy}}}$, where $R_{xz}=\sqrt{L_s^2+(\Delta x_{\max})^2}$, $R_{zy}=\sqrt{L_s^2+D_y^2}$. The constants $k_{x,tail}$, $k_{y,tail}$, C_x and C_y are to be determined as shown in [60]. The SA algorithm procedure is shown in Figure 4.2.

In Figure 4.2, the integral on k_y is performed first, and than follow by the integration on k_x. It starts from the estimate the outermost saddle point on k_x plane by using the ratio of dimension in x direction and the length of the strong region. When the $\tan^{-1}\left(\frac{\Delta x_{\max}}{L_s}\right)$ is equal to or less than 0.1, the tilt angle of the deformed

contour on k_x plane (δ_{k_x}) is equal to $\frac{\pi}{4}$ radian. Otherwise, the δ_{k_x} is estimated by using the root-finding techniques such as the muller's method [60]. Next, the domain and the step size of the numerical integration are calculated. Therefore, the estimate the outermost saddle point on k_y plane is performed for each k_x plane by using the ratio of dimension in y direction and the length of the strong region. When the $\tan^{-1}\left(\frac{\Delta D_y}{L_s}\right)$ is equal to or less than 0.1, the tilt angle of the deformed contour on k_y plane (δ_{k_y}) is equal to $\frac{\pi}{4}$ radian. Otherwise, the δ_{k_y} is estimated by using the root-finding techniques such as the muller's method. Next, the domain and the step size of the numerical integration are calculated. Finally, the numerical integration is estimated on the k_y plane and then on the k_x plane.

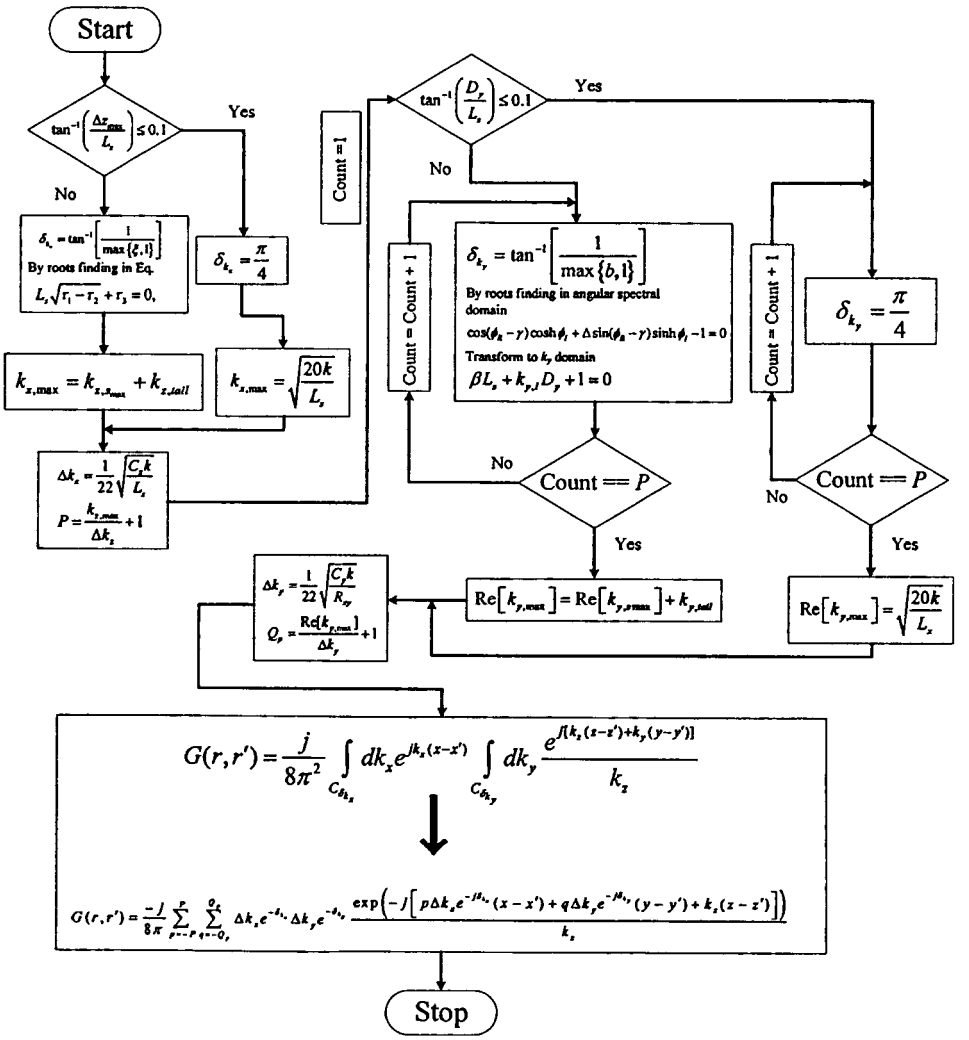

Figure 4.2 The flow chart of the SA algorithm procedure.

4.3 The Optimization of the SA parameters with the Genetic Algorithm (GA)

From free space 3D scalar Green's function in the spectral domain in (4.7), the numerical integration of the SA algorithm consists of the integration parameters as discuss in the previous section as follows

1. δ_{k_x} is the tilt angle of the deformed contour on k_x plane.
2. P is the domain of integration on k_x plane.
3. Δk_x is the integration step size of the k_x plane.
4. δ_{k_y} is the tilt angle of the deformed contour on k_y plane.
5. Q_p is the domain of integration on k_y plane, which it is varied on the integration on the k_x plane.
6. Δk_y is the integration step size of the k_y plane.

Normally, all of the SA's parameters are found by the analytical as discussed in previous section [60]. It is a complicate to find the optimum integration parameters. Moreover, it is difficult to find the integration parameter for the general problems. For gain its efficiency, the GA optimization is presented to find the optimum SA integration parameters for general problems including the optimum length of the strong region (L_s). The condition of the optimization is set as follow, the computation error is less than 1% and the minimum total computational time (both of the computational times in the weak and strong regions). Note that it is considered under the worse case scenario, which $del\_x = \Delta x_{\max}$, $del\_y = D_y$, and $del\_z = L_s$.

In this optimization, the SA numerical integration parameters are adjusted by the GA technique. It consists of

1. δ_{k_x} is the tilt angle of the deformed contour on k_x plane.
2. P is the domain of integration on k_x plane.
3. Δk_x is the integration step size of the k_x plane.
4. δ_{k_y} is the tilt angle of the deformed contour on k_y plane, where it is varied on k_x plane.

5. Q_p is the domain of integration on k_y plane, where it is varied on the integration on the k_x plane.
6. Δk_y is the integration step size of the k_y plane, where it is also varied on the integration on the k_x plane.
7. L_s is the length of the strong region.

The GA optimization is linked with the SA algorithm to find the optimum SA integration parameters. The GA optimization procedure is shown in Figure 4.6. It starts by the creation of the initial of the population size of GA and then calculate the fitness function by using the SA algorithm, when the fitness function is the total computational time and percentage of error. Next, the GA operators are employed to find the optimum parameters and the convergence criteria is checked on each iteration. It is stopped when the criteria is met. The simple GA is employed, which the GA operators consist of the selection wheel, crossover, mutation and elitism operators. The GA operators are defined as follows; i.e., 50 populations, the crossover of 80%, the mutation of 5% and the elitism with 5 best populations are employed. Therefore, some of examples are studied as shown in Table 4.1.

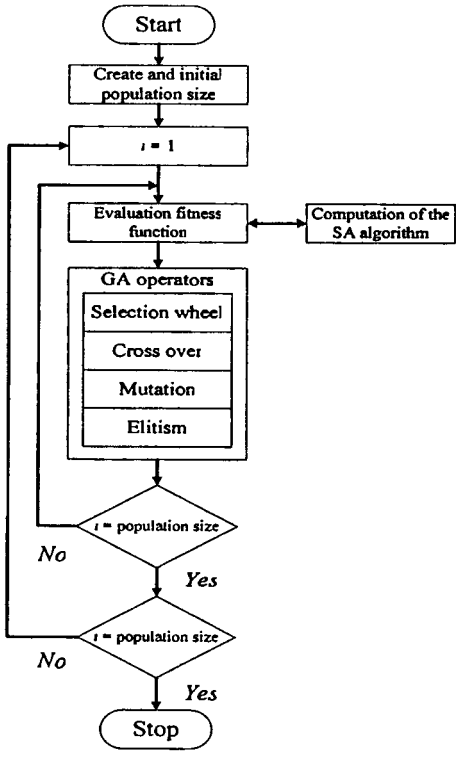

Figure 4.3 The flow chart of the GA optimization to find the optimum SA integration parameters.

Table 4.1 The case of study for the GA optimization of the optimum SA integration parameters.

Cases	D_y in (λ)	Optimum L_s (λ)
1	0.5	1.02
2	1	1.31
3	2	4.44
4	3	5.21
5	4	6

From the case of study in Table 4.1, the comparison of the computational time between the conventional SA algorithm and the optimum integration parameters optimized by the GA are shown in Fig. 4.4. It is found that the computation time of the optimum integration parameters is less than the conventional SA algorithm. However, the integration parameters of all cases are investigated.

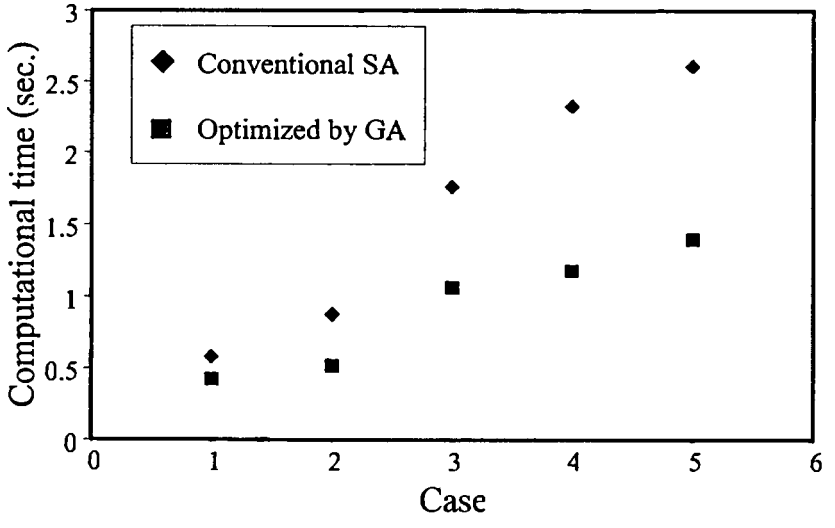

Figure 4.4 Comparison of the computational time between the conventional SA algorithm and the optimum integration parameters.

For the 1st case, the dimension in the y axis (D_y) is 0.5λ, where the optimum L_s is found to be 1.02λ. The optimum integration parameters are found to provide the minimum computational time and the percentage of error less than 1%. The optimum

integration parameters in the k_y and k_x planes are shown, which are found by the GA algorithm. In Table 4.2, the integration parameters on the k_x plane is shown by comparing with the conventional SA algorithm. It is found that the optimum integration parameters required the tilt angle 41.5 degree, the integration point is 30 points, and the integration step size is 0.475λ. In addition, the optimum integration parameters on k_y plane are shown in Figs. 4.5, 4.6, and 4.7. It is obvious that the tilt angle, the integration point, and the integration step are varied along the k_x plane. Moreover, the percentage of error along the x axis is shown in Fig. 4.8. The percentage of error of the optimum integration parameters is more than the computational error of the conventional SA algorithm, but it is less than 1%. It is sufficient for the engineering practice.

Table 4.2 The integration parameters on k_x plane of the D_y is 0.5λ.

No.	Parameters	Conventional SA	Optimized by GA
1	δ_{k_x}	45 degree	41.5 degree
2	P	45	30
3	Δk_x	0.318	0.475

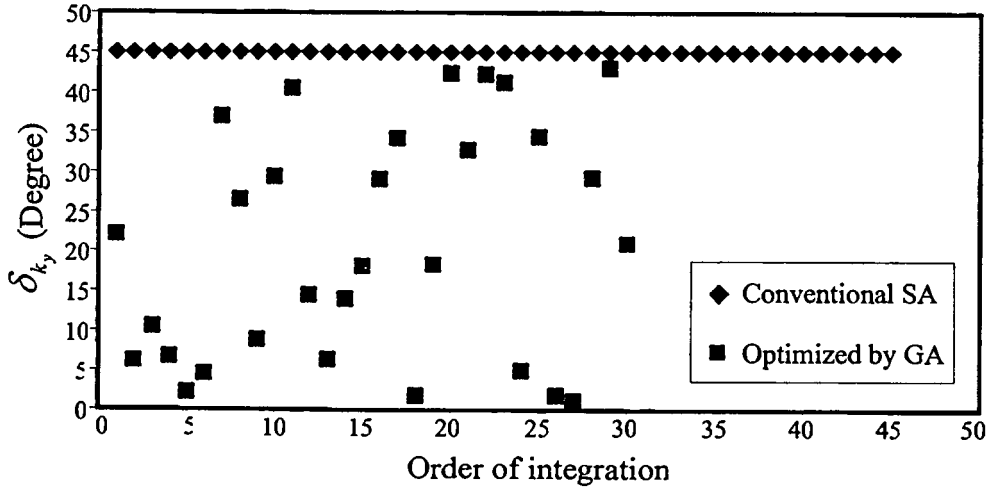

Figure 4.5 Comparison of the δ_{k_y} of the conventional SA algorithm and the optimum integration parameters when $D_y = 0.5\lambda$.

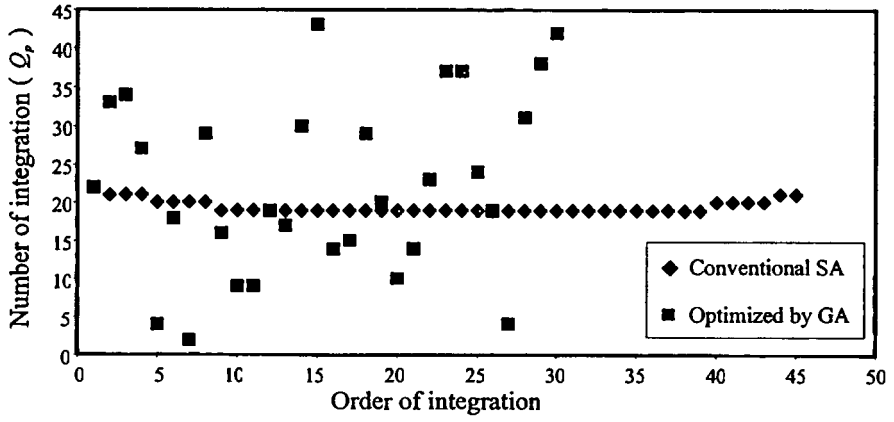

Figure 4.6 Comparison of the Q_p of the conventional SA algorithm and the optimum integration parameters when $D_y = 0.5\lambda$.

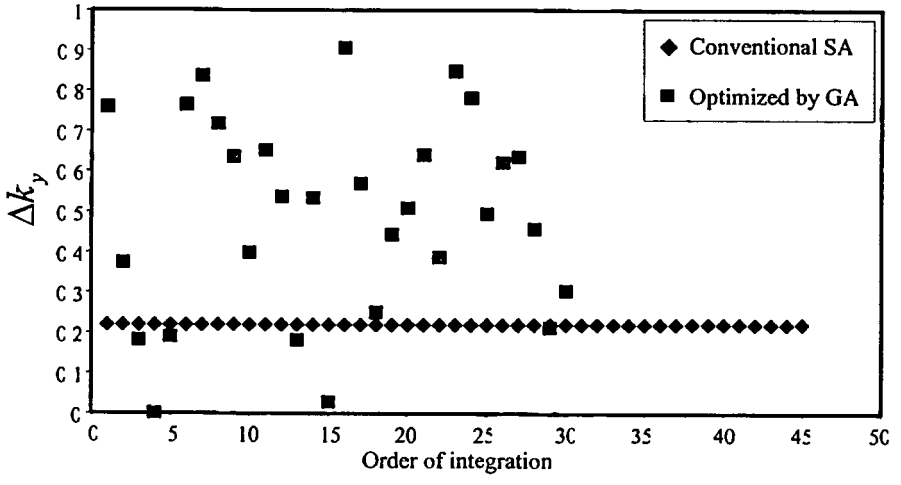

Figure 4.7 Comparison of the Δk_y of the conventional SA algorithm and the optimum integration parameters when $D_y = 0.5\lambda$.

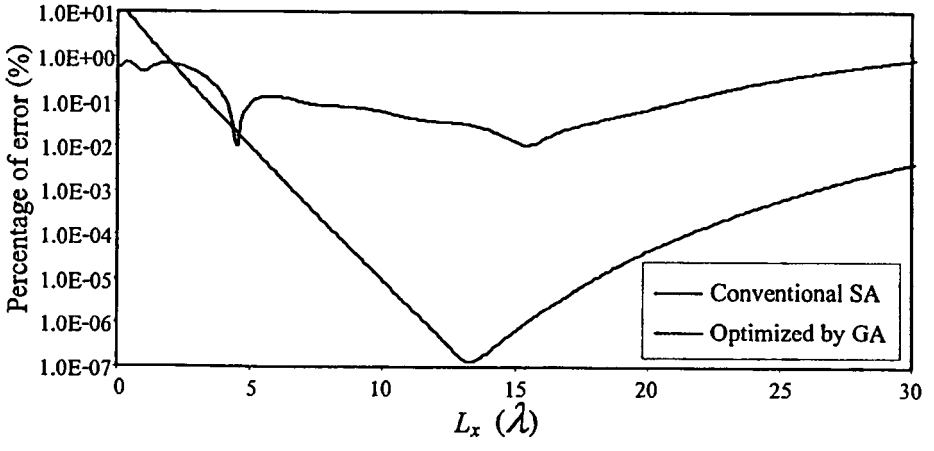

Figure 4.8 Comparison of percentage of error of the conventional SA algorithm and the optimum integration parameters when $D_y = 0.5\lambda$.

For the 2nd case, the D_y is 1λ, where the optimum L_s is found to be 1.31λ. The optimum integration parameters are found to provide the minimum computational time and the percentage of error less than 1%. The optimum integration parameters in the k_y and the k_x planes are shown, which are found by the GA algorithm. In Table 4.3, the integration parameters on the k_x plane is shown by comparing with the conventional SA algorithm. It is found that the optimum integration parameters required the tilt angle 36 degree, the integration point is 13 points, and the integration step size is 0.7λ. In addition, the optimum integration parameters on the k_y plane are shown in Figs. 4.9, 4.10, and 4.11. It is obvious that the tilt angle, the integration point, and the integration step are varied along the k_x plane. In addition, the computational error along the x axis is shown in Fig. 4.12. The percentage of error of the optimum integration parameters is more than the percentage of error of the conventional SA algorithm, but it is less than 1%. It is sufficient for the engineering practice.

Table 4.3 The integration parameters on k_x plane of the D_y is λ.

No.	Parameters	Conventional SA	Optimized by GA
1	δ_{k_x}	45 degree	36 degree
2	P	23	13
3	Δk_x	0.29	0.7

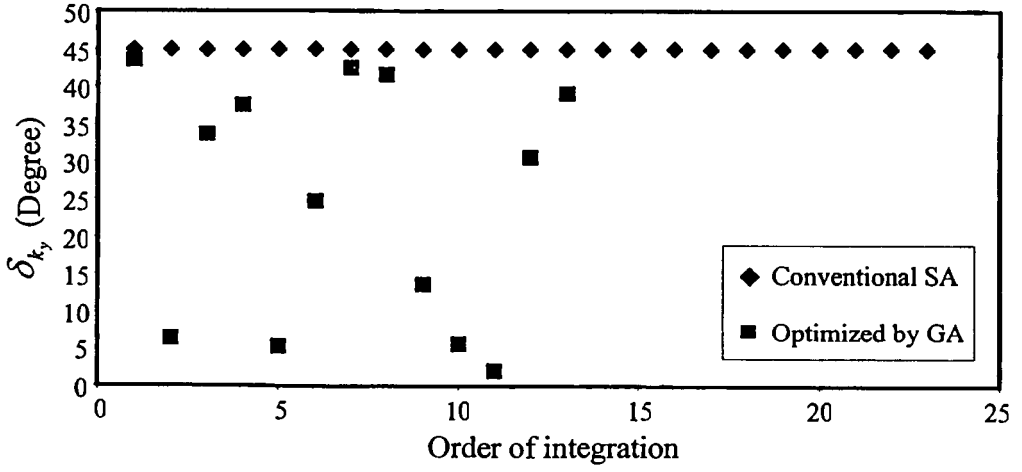

Figure 4.9 Comparison of the δ_{k_y} of the conventional SA algorithm and the optimum integration parameters when $D_y = \lambda$.

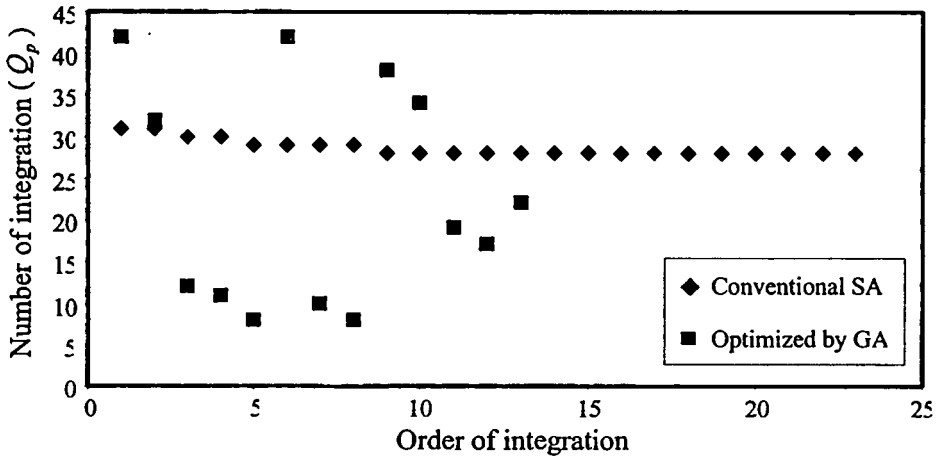

Figure 4.10 Comparison of the Q_p of the conventional SA algorithm and the optimum integration parameters when $D_y = \lambda$.

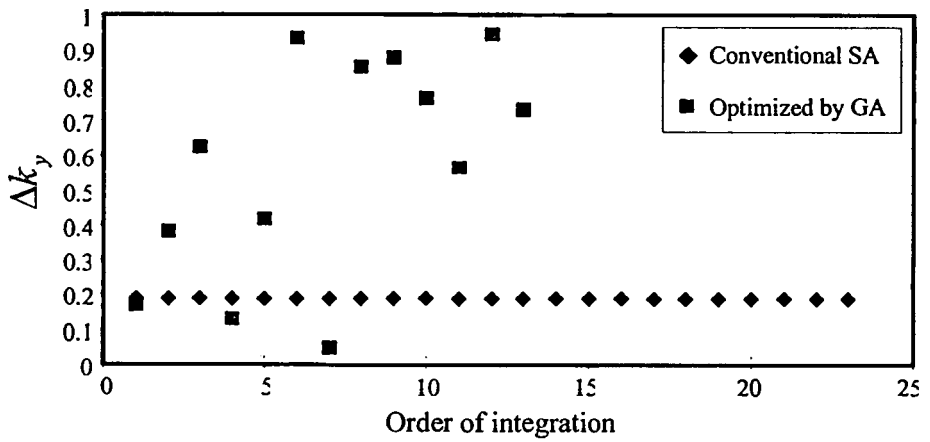

Figure 4.11 Comparison of the Δk_y of the conventional SA algorithm and the optimum integration parameters when $D_y = \lambda$.

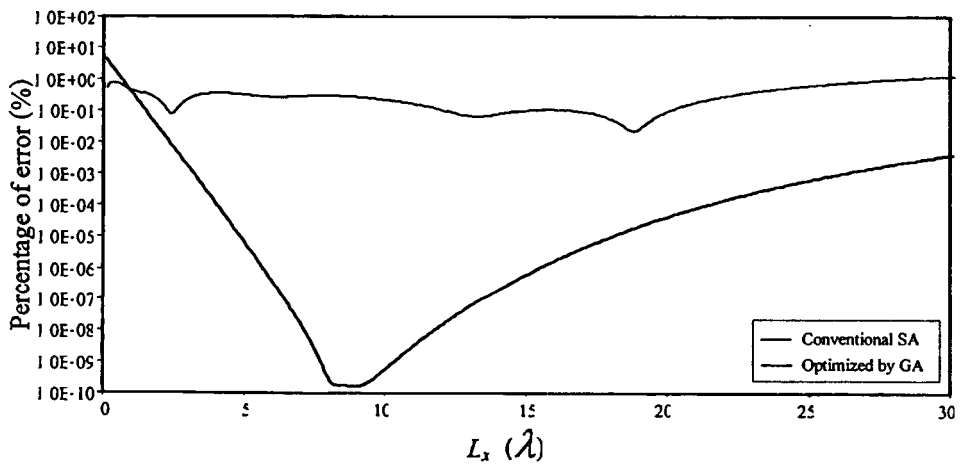

Figure 4.12 Comparison of percentage of error of the conventional SA algorithm and the optimum integration parameters when $D_y = \lambda$.

For the 3rd case, the D_y is 2λ, where the optimum L_s is found to be 4.44λ. The optimum integration parameters are found to provide the minimum computational time and the percentage of error less than 1%. The optimum integration parameters in the k_y and the k_x planes are shown, which are found by the GA algorithm. In Table 4.4, the integration parameters on the k_x plane is shown by comparing with the conventional SA algorithm. It is found that the optimum integration parameters required the tilt angle 36 degree, the integration point is 13 points, and the integration step size is 0.7λ. In addition, the optimum integration parameters on k_y plane are shown in Figs. 4.13, 4.14, and 4.15. It is obvious that the tilt angle, the integration point, and the integration step are varied along the k_x plane. Moreover, the computational error along the x axis is shown in Fig. 4.16. The computational error of the optimum integration parameters is more than the computational error of the conventional SA algorithm, but it is less than 1%. It is sufficient for the engineering practice.

Table 4.4 The integration parameters on k_x plane of the D_y is 2λ.

No.	Parameters	Conventional SA	Optimized by GA
1	δ_{k_x}	45 degree	25 degree
2	P	23	19
3	Δk_x	0.208	0.129

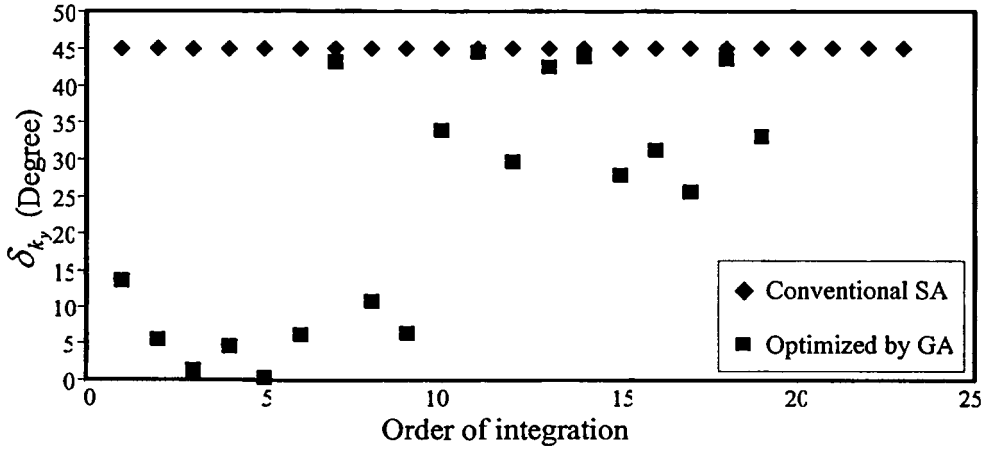

Figure 4.13 Comparison of the δ_{k_y} of the conventional SA algorithm and the optimum integration parameters when $D_y = 2\lambda$.

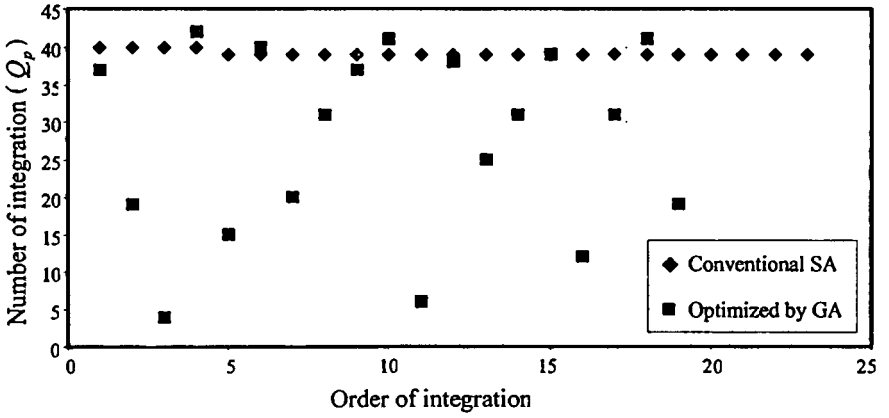

Figure 4.14 Comparison of the Q_p of the conventional SA algorithm and the optimum integration parameters when $D_y = 2\lambda$.

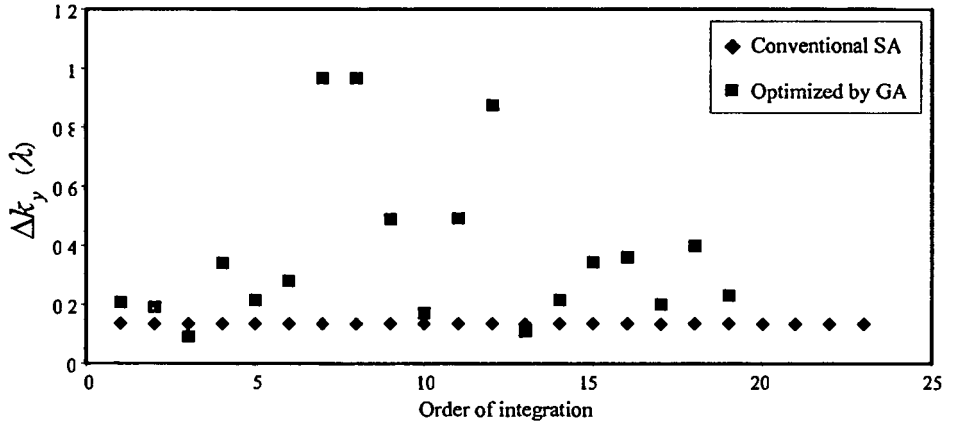

Figure 4.15 Comparison of the Δk_y of the conventional SA algorithm and the optimum integration parameters when $D_y = 2\lambda$.

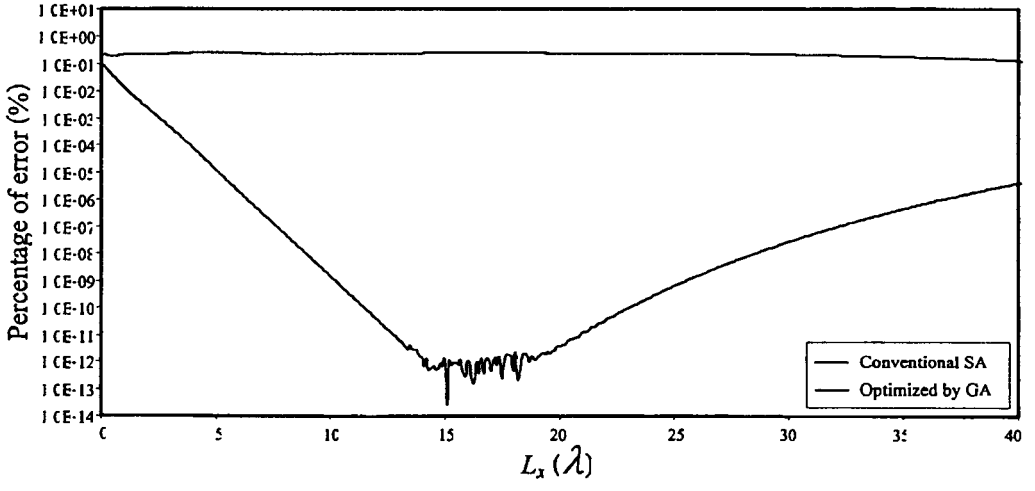

Figure 4.16 Comparison of percentage of error of the conventional SA algorithm and the optimum integration parameters when $D_y = 2\lambda$.

For the 4th case, the D_y is 3λ, where the optimum L_s is found to be 5.21λ. The optimum integration parameters are found to provide the minimum computational time and the percentage of error less than 1%. The optimum integration parameters in the k_y and the k_x are shown, which are found by the GA algorithm. In Table 4.5, the integration parameters on the k_x plane is shown by comparing with the conventional SA algorithm. It is found that the optimum integration parameters required the tilt angle 35 degree, the integration point 17 points, and the integration step size is 0.625λ. In addition, the optimum integration parameters on k_y plane are shown in Figs. 4.17, 4.18, and 4.19. It is obvious that the tilt angle, the integration point, and the integration step are varied along the k_x plane. Moreover, the percentage of error along the x axis is shown in Fig. 4.20. The percentage of error of the optimum integration parameters is more than the percentage of error of the conventional SA algorithm, but it is less than 1%. It is sufficient for the engineering practice.

Table 4.5 The integration parameters on k_x plane of the D_y is 3λ.

No.	Parameters	Conventional SA	Optimized by GA
1	δ_{k_x}	45 degree	35 degree
2	P	23	17
3	Δk_x	0.133	0.625

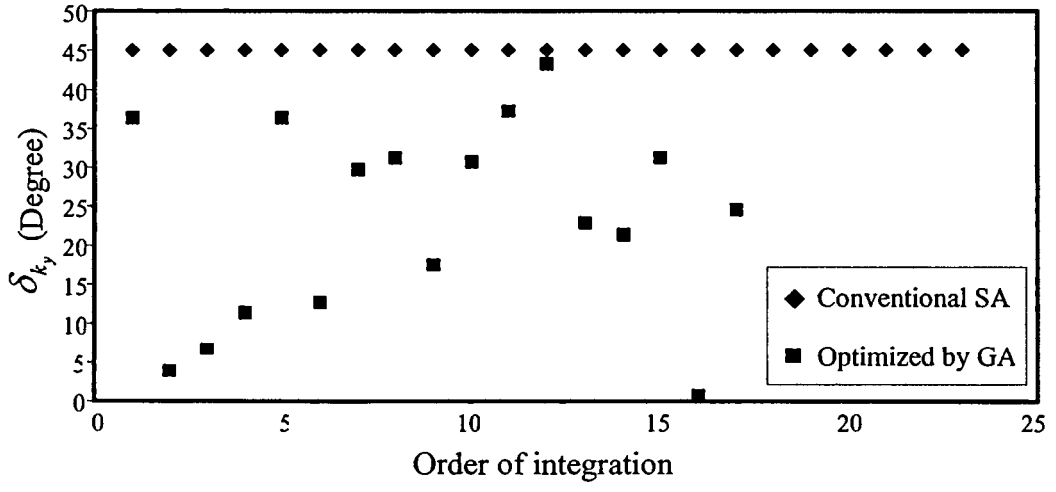

Figure 4.17 Comparison of the δ_{k_y} of the conventional SA algorithm and the optimum integration parameters when $D_y = 3\lambda$.

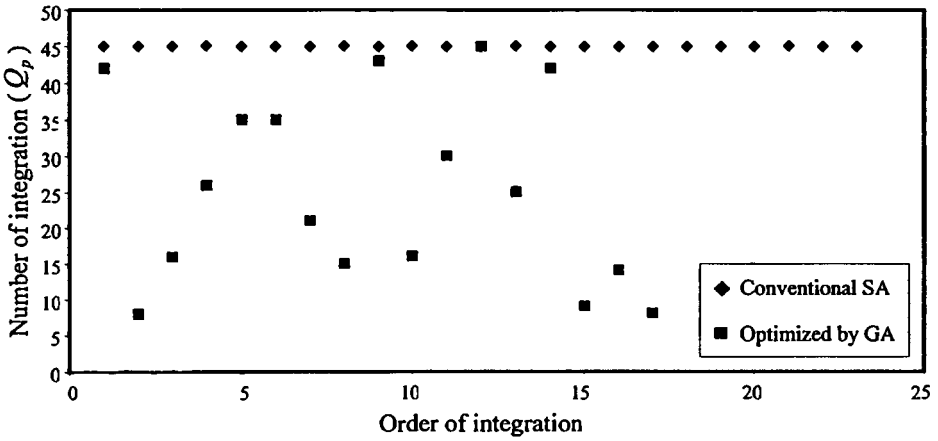

Figure 4.18 Comparison of the Q_p of the conventional SA algorithm and the optimum integration parameters when $D_y = 3\lambda$.

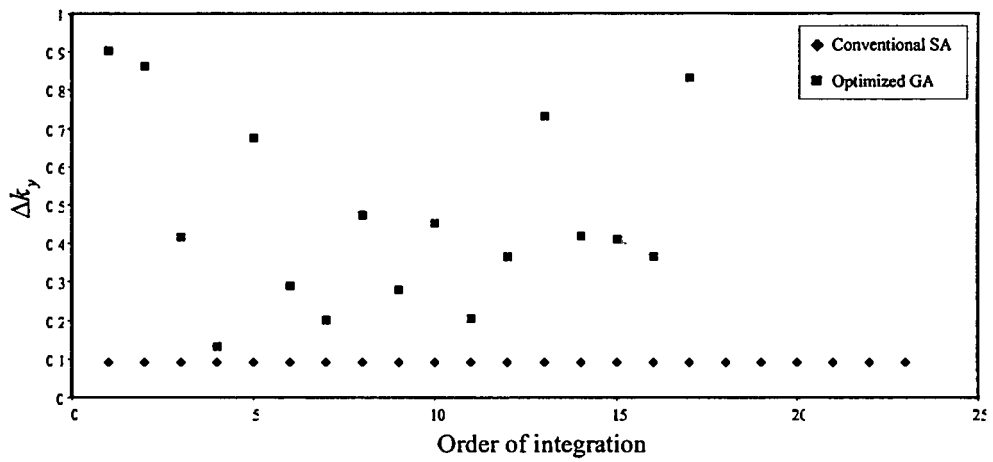

Figure 4.19 Comparison of the Δk_y of the conventional SA algorithm and the optimum integration parameters when $D_y = 3\lambda$.

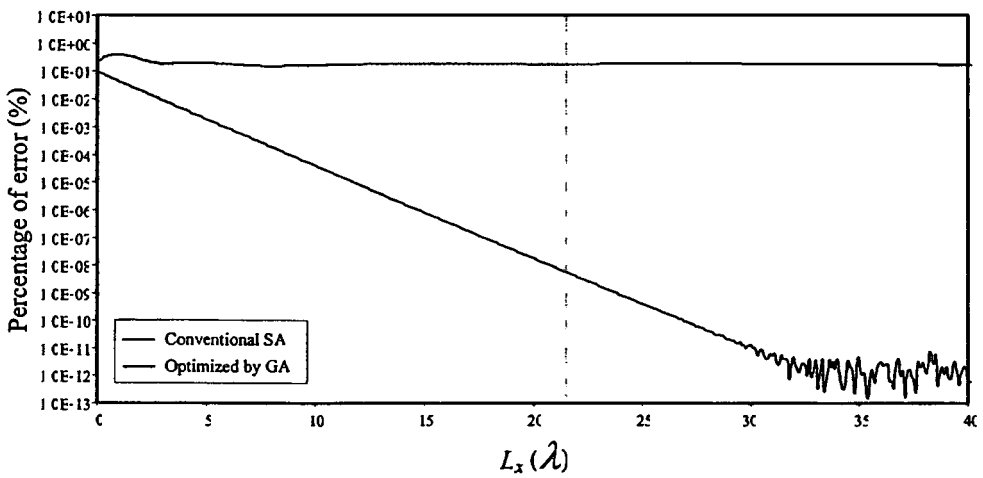

Figure 4.20 Comparison of percentage of error of the conventional SA algorithm and the optimum integration parameters when $D_y = 3\lambda$.

For the 5th case, the D_y is 4λ, where the optimum L_s is found to be 6λ. The optimum integration parameters are found to provide the minimum computational time and the percentage of error less than 1%. The optimum integration parameters in the k_y and the k_x planes are shown, which are found by the GA algorithm. In Table 4.6, the integration parameters on the k_x plane is shown by comparing with the conventional SA algorithm. It is found that the optimum integration parameters required the tilt angle 37 degree, the integration point is 8 points, and the integration step size is 0.312λ. In addition, the optimum integration parameters on k_y plane are shown in Figs. 4.21, 4.22, and 4.23. It is obvious that the tilt angle, the integration point, and the integration step are varied along the k_x plane. Moreover, the percentage of error along the x axis is shown in Fig. 4.24. The computational error of the optimum integration parameters is more than the percentage of error of the conventional SA algorithm, but it is less than 1%. It is sufficient for the engineering practice.

Table 4.6 The integration parameters on k_x plane of the D_y is 4λ.

No.	Parameters	Conventional SA	Optimized by GA
1	δ_{k_x}	45 degree	37 degree
2	P	23	8
3	Δk_x	0.085	0.312

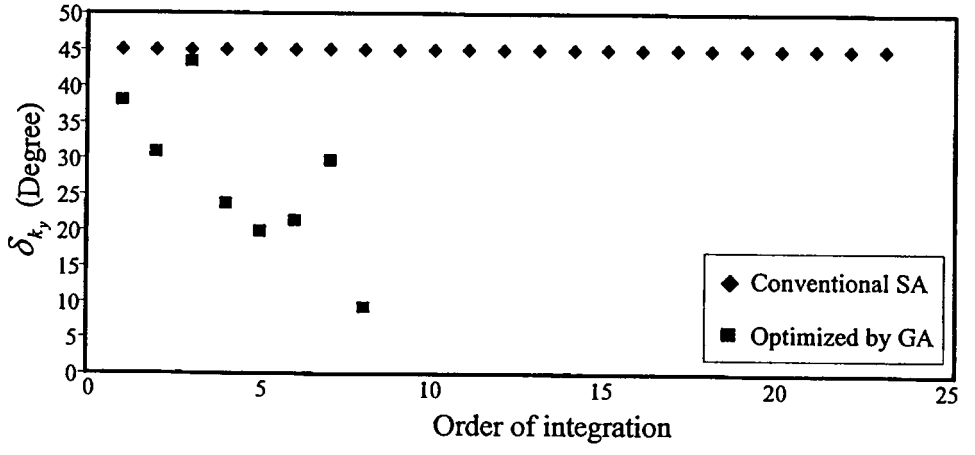

Figure 4.21 Comparison of the δ_{k_y} of the conventional SA algorithm and the optimum integration parameters when $D_y = 4\lambda$.

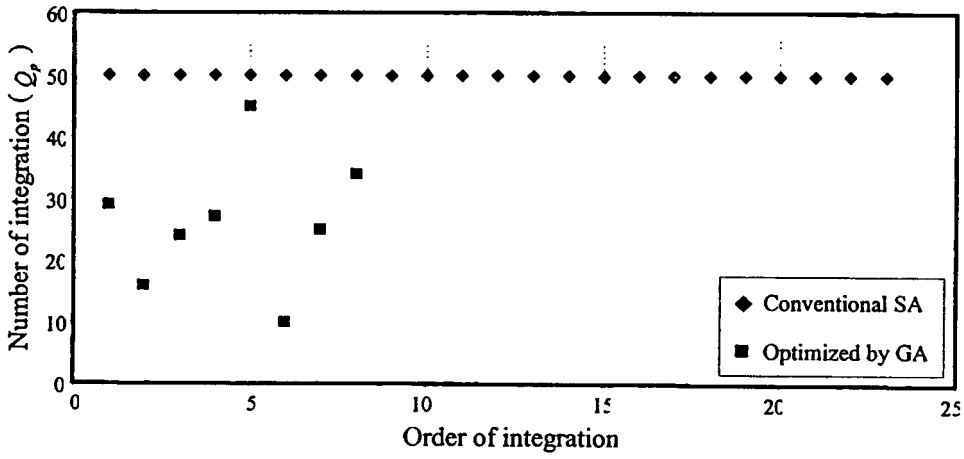

Figure 4.22 Comparison of the Q_p of the conventional SA algorithm and the optimum integration parameters when $D_y = 4\lambda$.

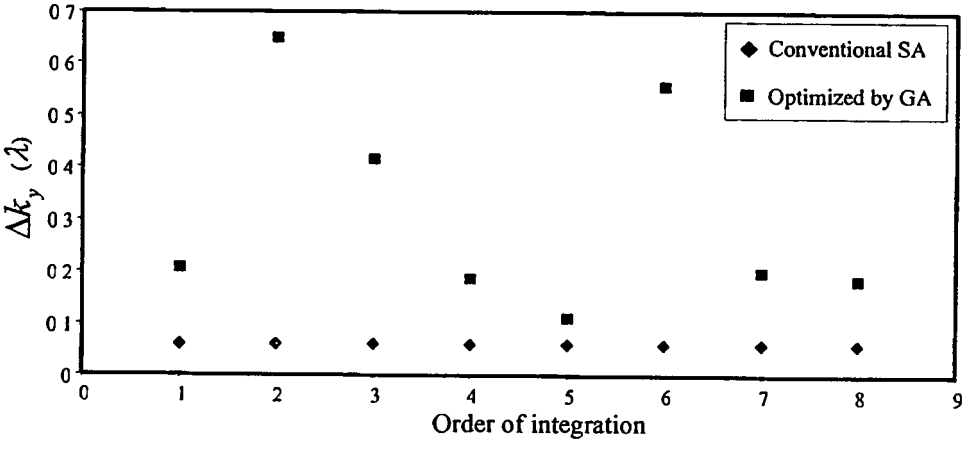

Figure 4.23 Comparison of the Δk_y of the conventional SA algorithm and the optimum integration parameters when $D_y = 4\lambda$.

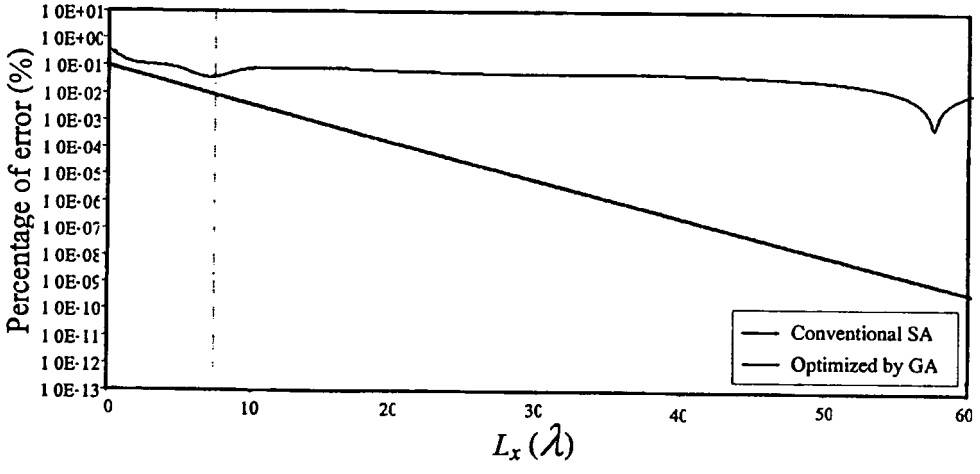

Figure 4.24 Comparison of percentage of error of the conventional SA algorithm and the optimum integration parameters when $D_y = 4\lambda$.

4.4 Numerical Results

In this section, the numerical results are presented to demonstrate the accuracy and efficiency of the hybrid MSMM/CG/SA method. Both the uniform and non-uniform dipole antenna arrays are considered as examples.

4.4.1 Uniform Collinear Dipole Antenna Array

For the first example, the uniform collinear dipole antenna array of 100 elements is analyzed in this section. The array parameters are given as follow: $L_z = 0.5\lambda$ and $l = \lambda$ with radius of 0.005λ. Twenty-one PWL basis functions for each dipole element are employed resulting in $N = 2{,}100$ and each element is excited by 1 Volt at the center. Figure 4.25 shows the compared the RMS error between hybrid MSMM/CG and the hybrid MSMM/CG/SA methods, which they are converged within the 3 iterations when the RMS error of 10^{-3} is employed. However, the RMS error of the hybrid MSMM/CG/SA method is more than RMS error of the hybrid MSMM/CG method, which it can be accepted in the engineering practice. Moreover, the normalized magnitude and the phase of the current distribution are shown in Fig. 4.26, where both the hybrid MSMM/CG/SA and hybrid MSMM/CA methods provide identical results.

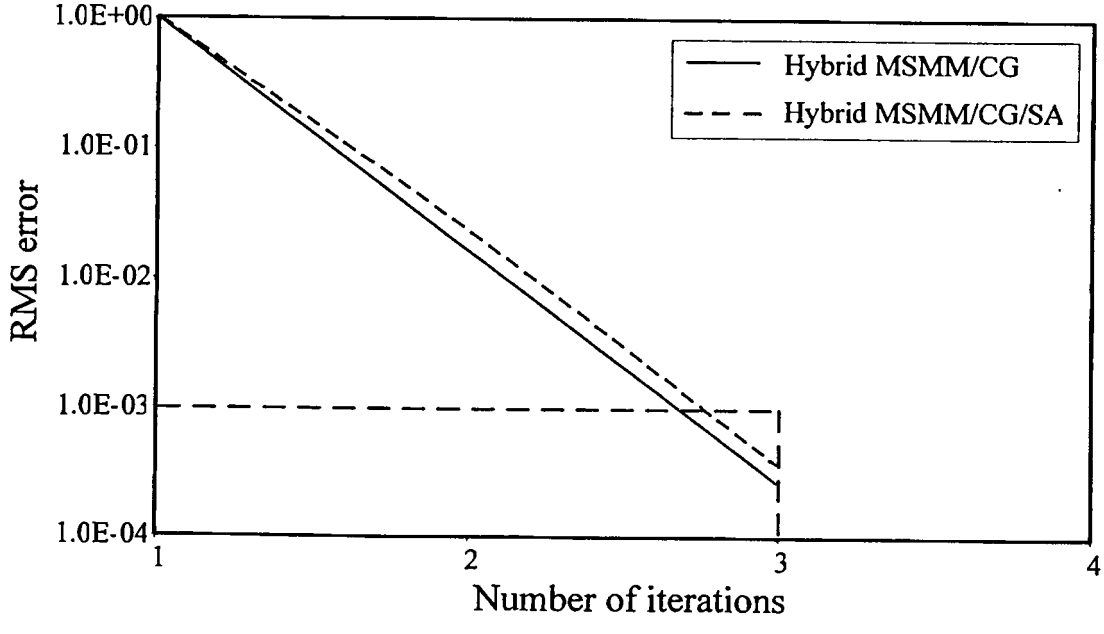

Figure 4.25 The RMS error of the hybrid MSMM/CG and the hybrid MSMM/CG/SA methods for uniform collinear dipole antenna arrays of 100 elements.

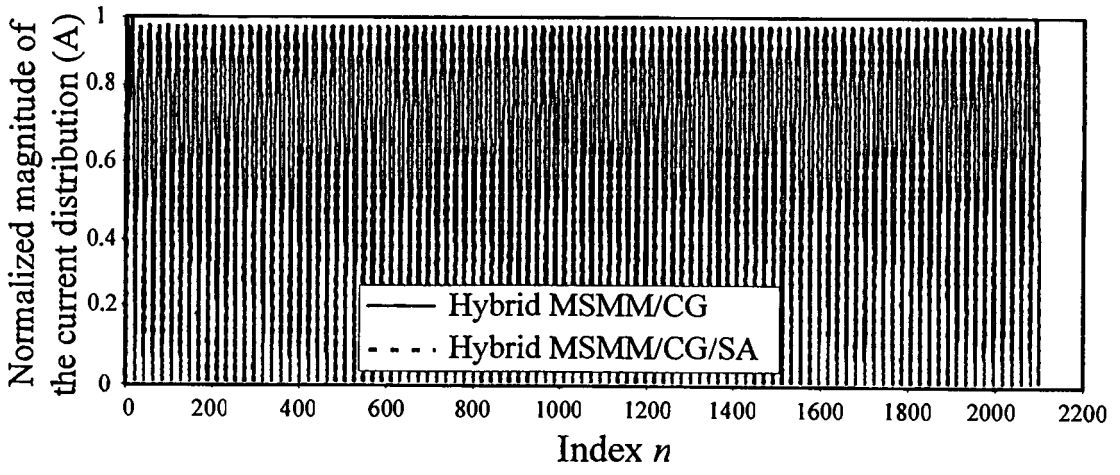

(a)

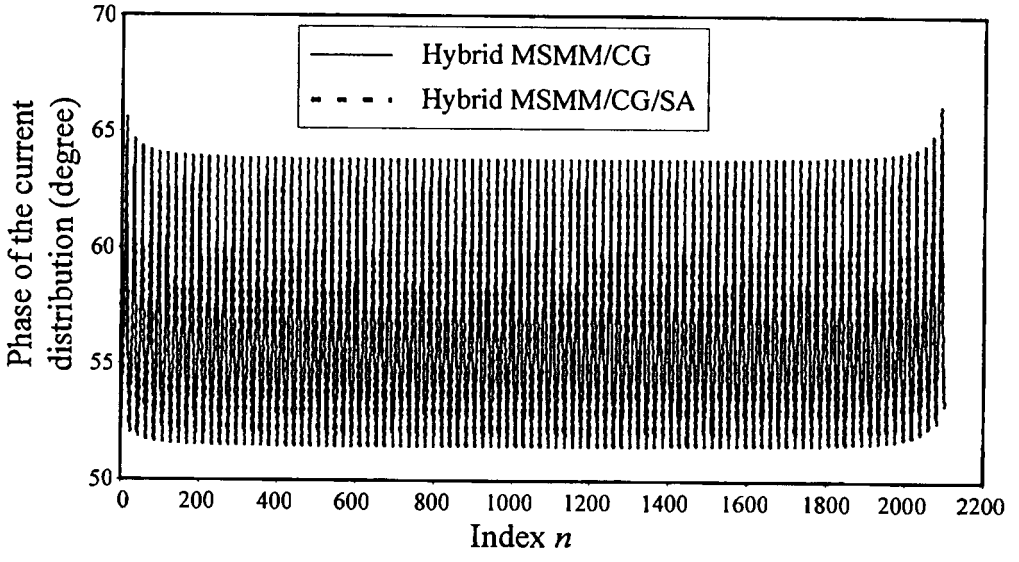

(b)

Figure 4.26 Current distribution of the uniform collinear dipole antenna array of 100 elements. (a) Normalized magnitude of the current distribution, and (b) Phase of the current distribution.

4.4.2 Uniform Planar Dipole Antenna Array

For uniform planar array, consider the 21×4 uniform planar dipole antenna array in free space. The array parameters are given as follows: $L_{x,j} = 0.5\lambda$, $L_{z,k} = 0.5\lambda$ and $l = 0.5\lambda$ with radius of 0.005λ. Twenty-one PWL basis functions for each dipole element are employed resulting in N = 1,764 and each element is excited by 1 Volt at the center. Figure 4.27 shows the compared the RMS error between hybrid MSMM/CG and the hybrid MSMM/CG/SA methods, where they are

converged within 6 iterations. However, the RMS error of the hybrid MSMM/CG/SA method is more than RMS error of the hybrid MSMM/CG method, which it can be accepted in the engineering practice. Moreover, the normalized magnitude and the phase of the current distribution are shown in Fig. 4.28, where both hybrid MSMM/CG/SA and hybrid MSMM/CA methods provide identical results.

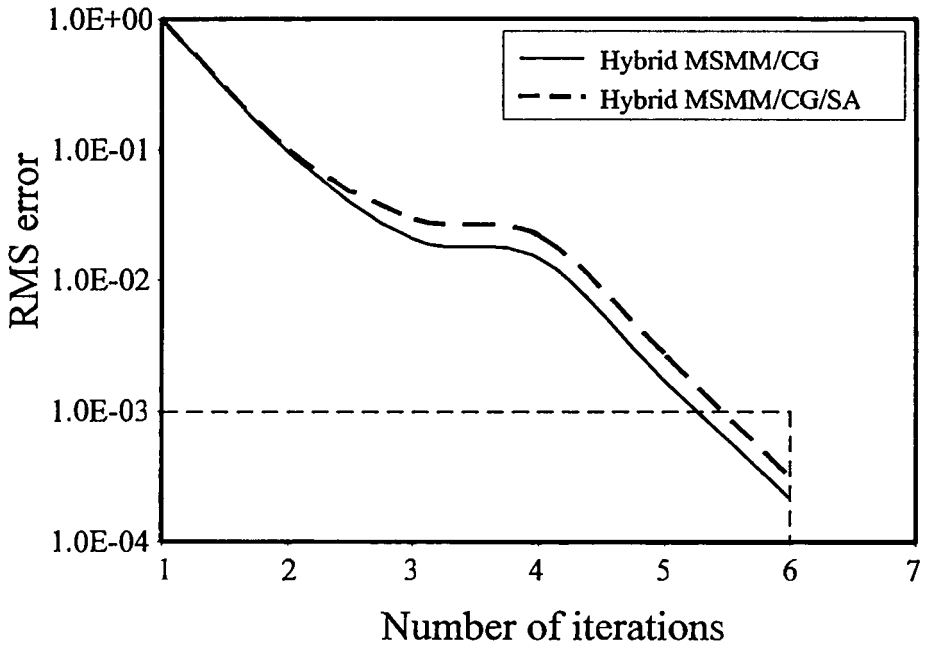

Figure 4.27 The RMS error of the hybrid MSMM/CG and the hybrid MSMM/CG/SA methods for uniform collinear dipole antenna arrays of 100 elements.

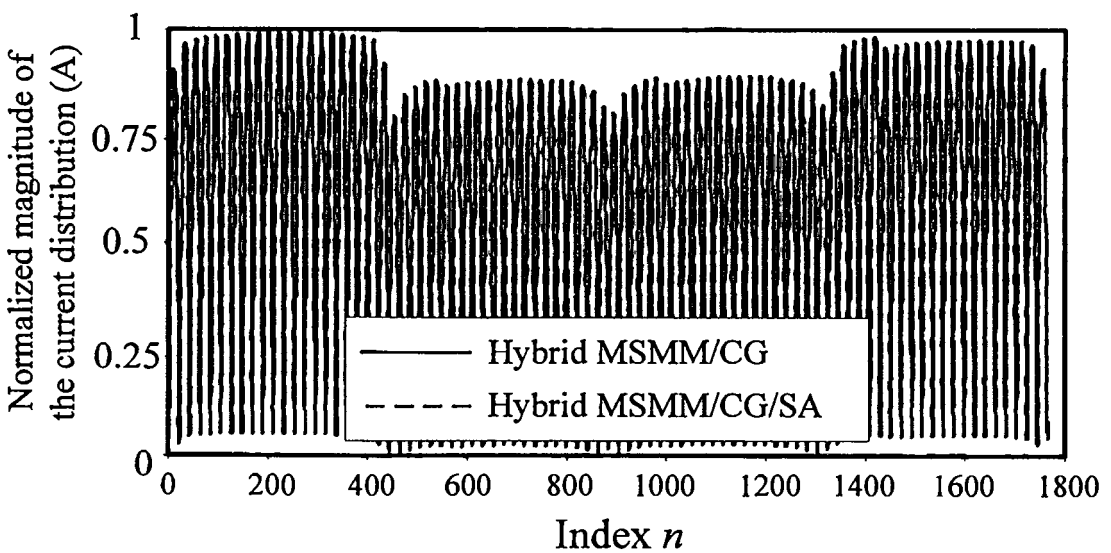

(a)

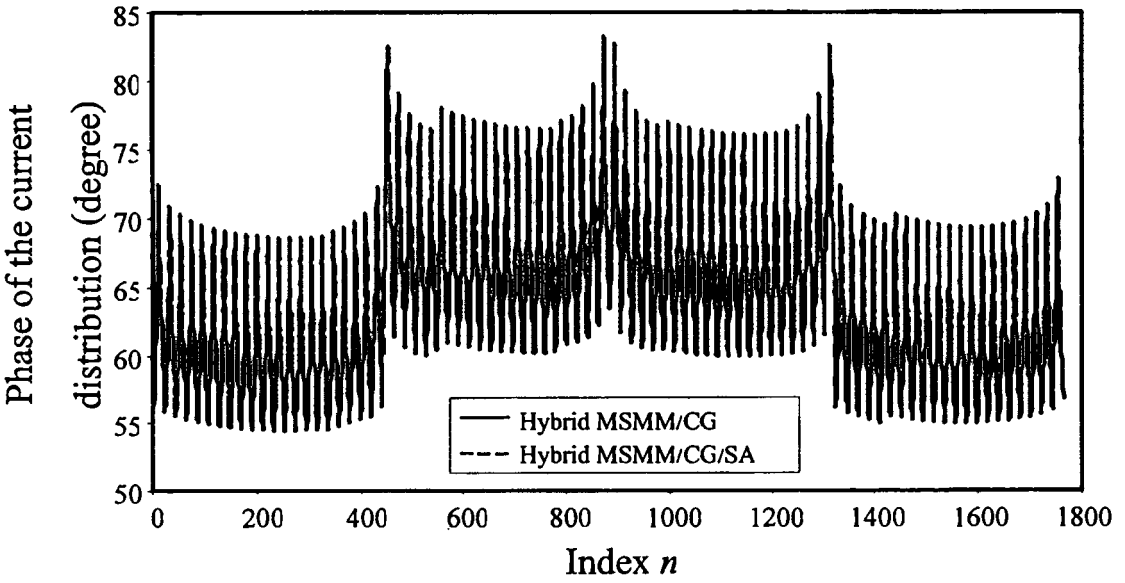

(b)

Figure 4.28 Current distribution of the uniform collinear dipole antenna array of 100 elements. (a) Normalized magnitude of the current distribution, and (b) Phase of the current distribution.

4.4.3 Non-uniform Collinear Dipole Antenna Array

For the 26 elements non-uniform collinear dipole antennas, the array parameters are given as $l = 0.5\lambda$ with radius of 0.005λ, and the distance between each elements are given in Table. 4.7. Only 13 elements are shown due to its symmetrical structure. Twenty-one PWL basis functions for each element are used resulting in $N = 546$ and each element is excited by 1 Volt at the center. Figure 4.29 shows the compared the RMS error between hybrid MSMM/CG and hybrid MSMM/CG/SA methods, which they are converged within 7 iterations with a little fluctuation, when the RMS error of 10^{-3} is employed. However, the RMS error of the hybrid MSMM/CG/SA method is more than RMS error of the hybrid MSMM/CG method, which can be accepted in the engineering practice. Moreover, the normalized magnitude and the phase of the current distribution are shown in Fig. 4.30, which it is found that the hybrid MSMM/CG/SA and the hybrid MSMM/CA methods are identical.

Table 4.7 Distance between each element of the non-uniform collinear dipole antenna array of 26 elements.

Parameters	Distance (λ)
$L_{z,1}$	1.406
$L_{z,2}$	1.177
$L_{z,3}$	1.005
$L_{z,4}$	1.392
$L_{z,5}$	0.739
$L_{z,6}$	1.036
$L_{z,7}$	0.233
$L_{z,8}$	1.398
$L_{z,9}$	0.522
$L_{z,10}$	0.892
$L_{z,11}$	0.732
$L_{z,12}$	0.423
$L_{z,13}$	0.424

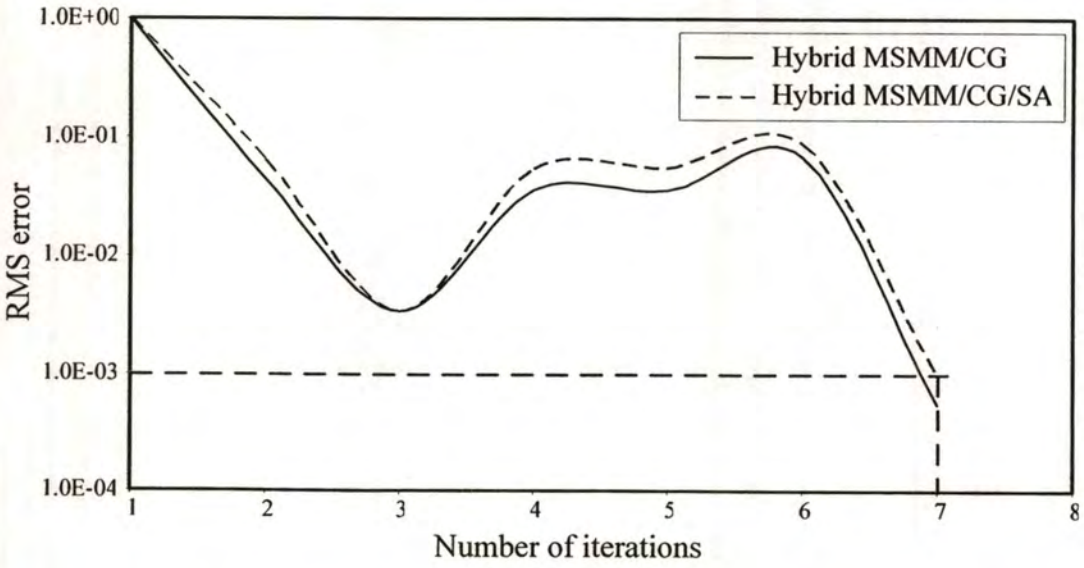

Figure 4.29 The RMS error of the hybrid MSMM/CG and the hybrid MSMM/CG/SA methods for the non-uniform collinear dipole antenna array of 26 elements.

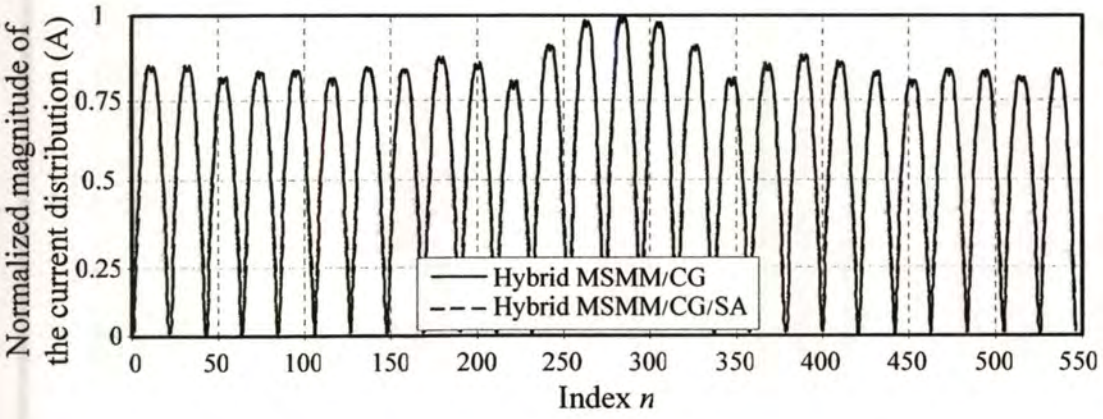

(a)

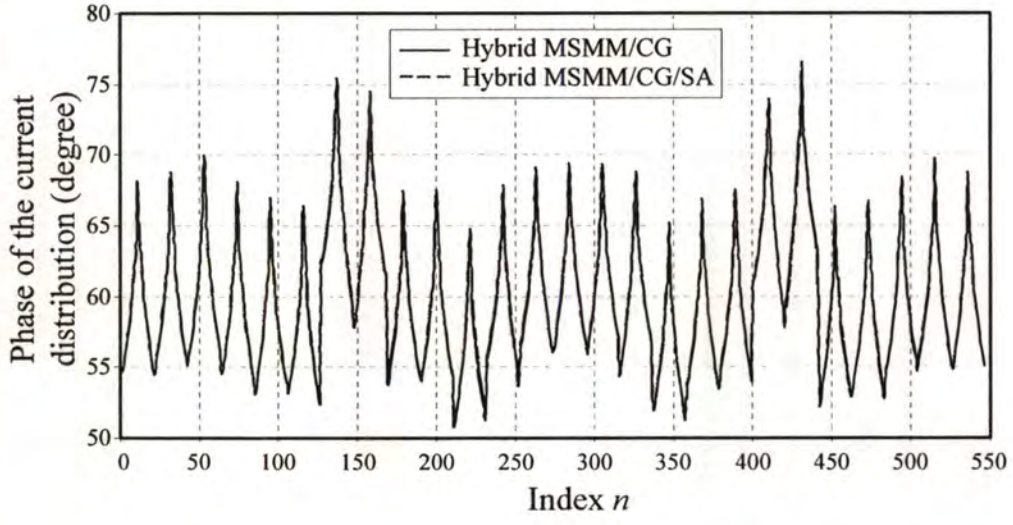

(b)

Figure 4.30 Current distribution of the non-uniform collinear dipole antenna array of 26 elements. (a) Normalized magnitude of the current distribution, and (b) Phase of the current distribution.

4.4.4 Non-uniform Planar Dipole Antenna Array

For this section, a non-uniform planar dipole antenna array of 24×3 elements is analyzed, which was used to reduce the Side Lobe Level (SLL). The array parameters are given as follows: $l = 0.5\lambda$ with radius of 0.005λ, and the distances between each element are shown in Table 4.8. Only 12 elements are shown due to its symmetrical structure. Twenty-one PWL basis functions for each element are employed resulting in $N = 1{,}512$, and each element is excited by 1 Volt at the center.

Table 4.8 Distance between each element of 24×3 non-uniform planar dipole antenna array.

Parameters	Distance (λ)
$L_{x,1}, L_{z,1}$	0.375
$L_{x,2}, L_{z,2}$	0.125
$L_{x,3}, L_{z,3}$	0.620
$L_{x,4}, L_{z,4}$	0.370
$L_{x,5}, L_{z,5}$	0.750
$L_{x,6}, L_{z,6}$	0.785
$L_{x,7}, L_{z,7}$	1.050
$L_{x,8}, L_{z,8}$	1.245
$L_{x,9}, L_{z,9}$	1.545
$L_{x,10}, L_{z,10}$	1.890
$L_{x,11}, L_{z,11}$	2.386
$L_{x,12}, L_{z,12}$	2.893

Figure 4.31 shows the comparison of the RMS error between hybrid MSMM/CG and the hybrid MSMM/CG/SA methods, where both are converged within 8 and 9 iterations with a little fluctuation, respectively. However, the RMS error of the hybrid MSMM/CG/SA method is more than RMS error of the hybrid MSMM/CG method, which can be accepted in the engineering practice. Moreover, the normalized magnitude and the phase of the current distribution are shown in Fig. 4.32, which it is found that the hybrid MSMM/CG/SA and the hybrid MSMM/CG methods are identical.

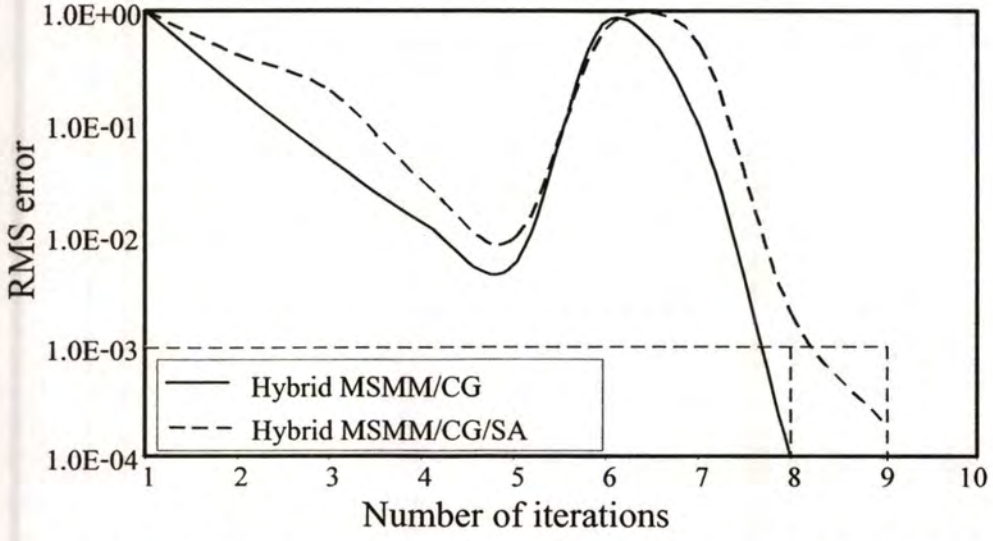

Figure 4.31 The RMS error of the hybrid MSMM/CG and the hybrid MSMM/CG/SA methods for 24×3 non-uniform planar dipole antenna arrays.

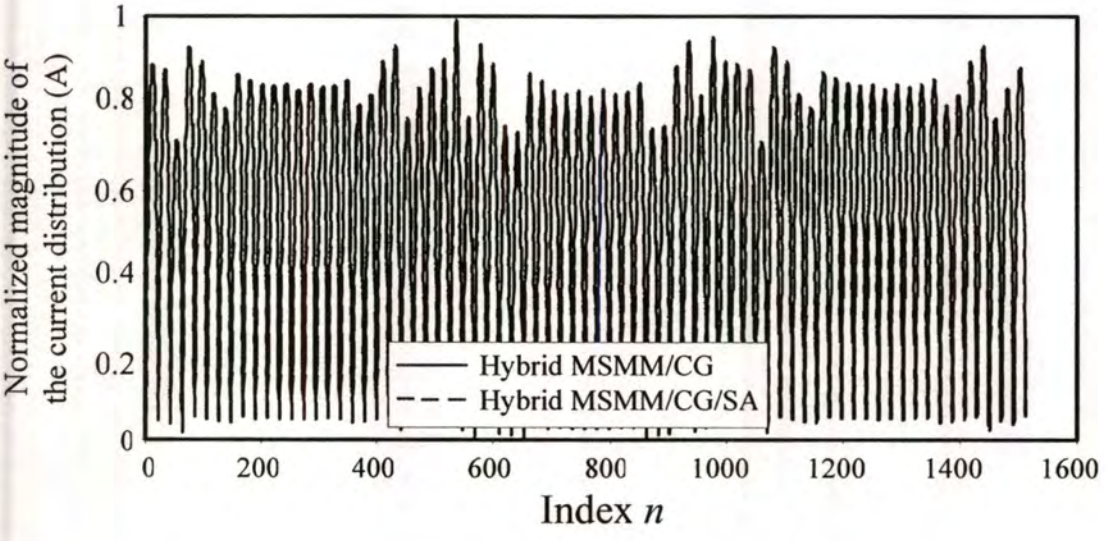

(a)

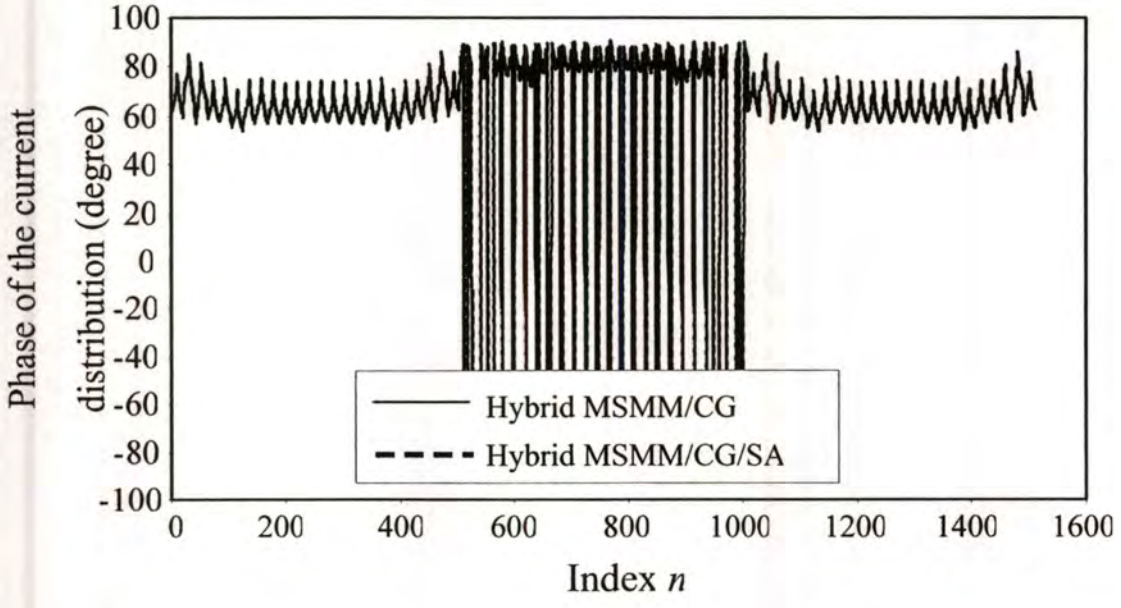

(b)

Figure 4.32 Current distribution of the 24×3 non-uniform planar dipole antenna array. (a) Normalized magnitude of the current distribution, and (b) Phase of the current distribution.

4.4.5 Computational Time and Memory Requirement

In this section, the computational time and the memory requirement of the SA algorithm for the collinear and planar dipole antenna arrays are considered. Figure 4.33 shows the computational time of the collinear dipole antenna array with $D_y = 0.005\lambda$, and $L_s = 3\lambda$, which is found that the computational time for this case is tend to $O(N)$. In addition, the computational time for the planar dipole antenna array with $D_y = 3\lambda$, and $L_s = 7\lambda$ are shown in Fig. 4.34. It is obvious that the hybrid MSMM/CG/SA method is still tend to $O(N)$, when the dimension of the planar dipole antenna array is tend to be rectangular planar array. Moreover, the memory requirement is found that it is also $O(N)$ as shown in Fig. 4.35.

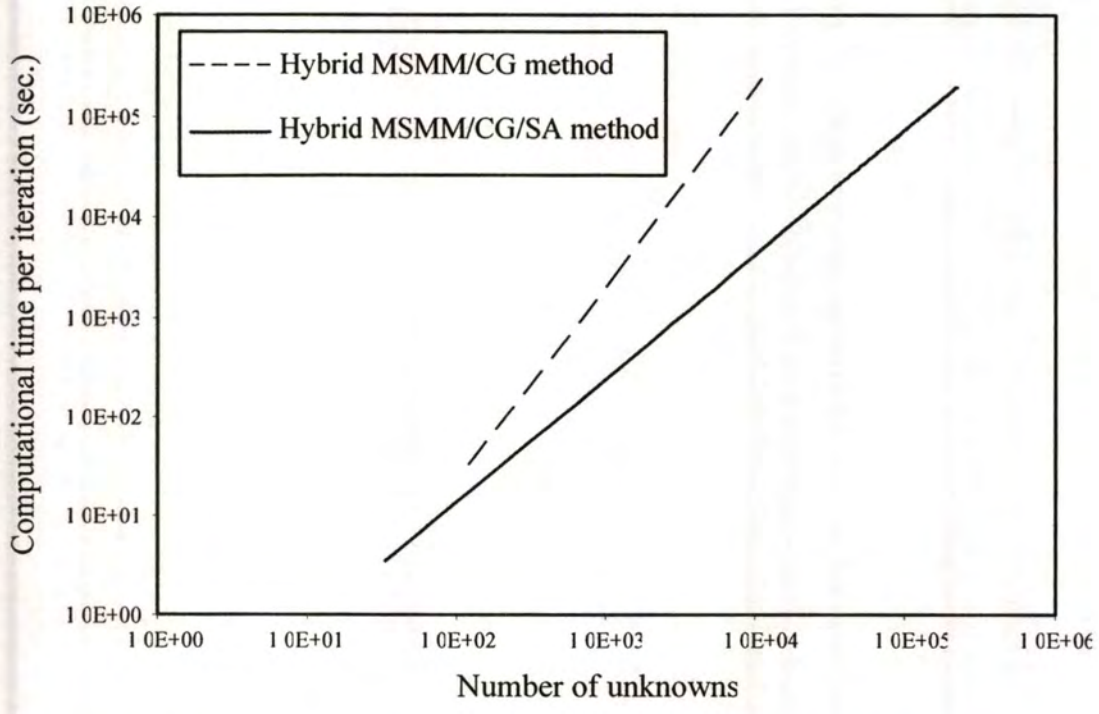

Figure 4.33 The computational time of the collinear dipole antenna array.

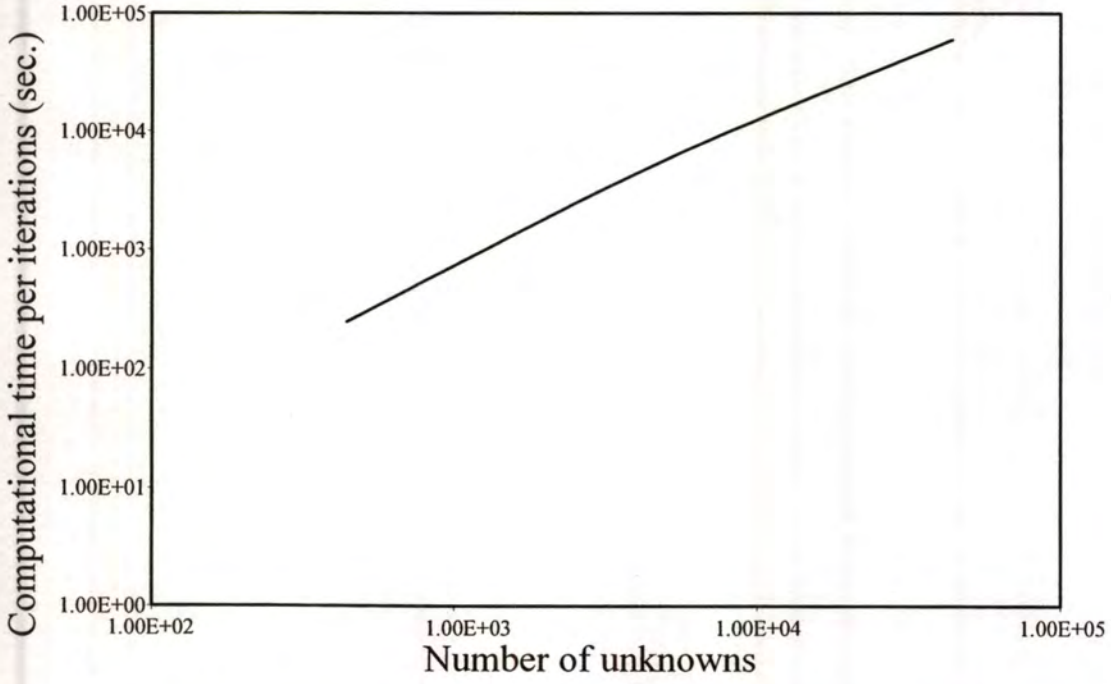

Figure 4.34 The computational time of the planar dipole antenna array.

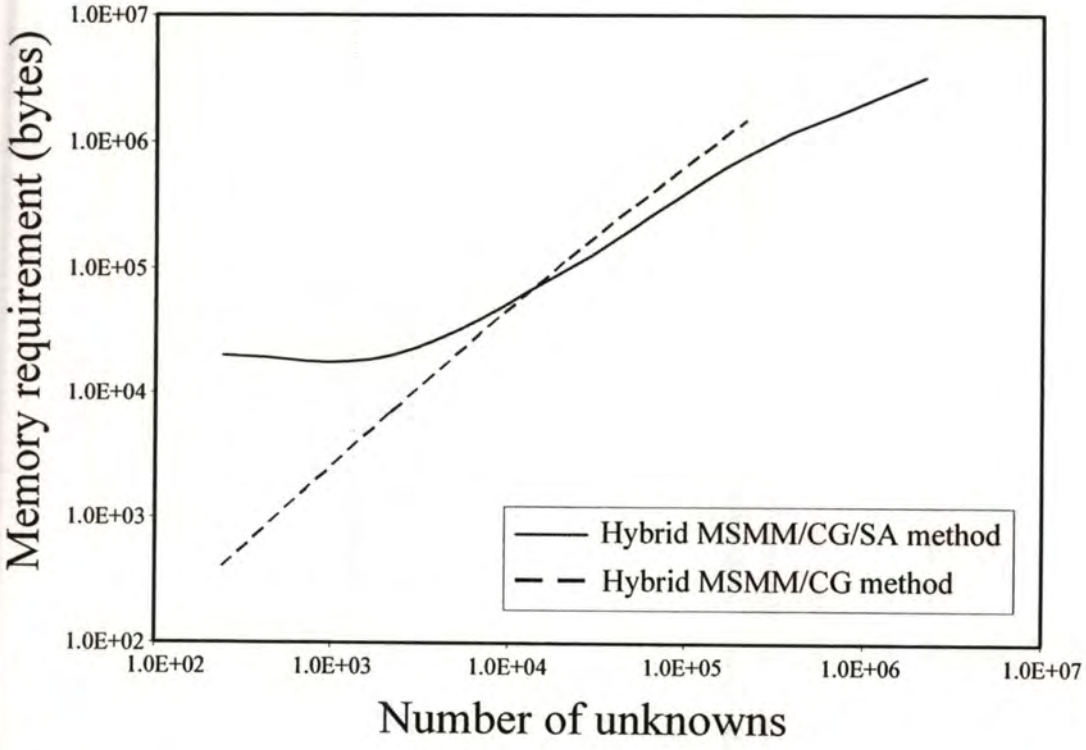

Figure 4.35 The memory requirement of the hybrid MSMM/CG/SA method.

4.5 Conclusions

The hybrid MSMM/CG/SA method can be efficiently applied to analyze an electrically large uniform and non-uniform dipole antenna arrays in free space. Moreover, the GA can be applied to optimize the SA parameters to the minimum error and the minimum computational time. Numerical results are presented to demonstrate the accuracy and efficiency of the hybrid MSMM/CG/SA method. For both uniform and non-uniform dipole antenna arrays, it shows the accuracy and efficiency of the SA algorithm for large uniform and non-uniform dipole antenna array. In addition, it is obvious that the computational time per iteration of the hybrid MSMM/CG/SA method tends to be $O(N)$ with the array increment in one direction, while that of the hybrid MSMM/CG method tends to be $O(N^2)$.

CHAPTER 5
THE MSMM/SA/GA DESIGN OF COLLINEAR DIPOLE ANTENNA ARRAYS

5.1 Introduction

In this chapter, the MSMM with the Spectral Acceleration (SA) algorithm and the Genetic Algorithm (GA) optimization is proposed to design uniform and non-uniform spacing collinear dipole antenna arrays in free space. As discussed in details in Chapter 4, the SA algorithm is employed to accelerate the MSMM to be $O(N)$, and the GA is incorporated to find optimum array parameters, where N is the total number of unknowns. Under this appropriate combination, numerical results are presented to demonstrate the accuracy and efficiency of the MSMM/SA/GA method for electrically large uniform and non-uniform spacing collinear dipole antenna arrays in free space.

5.2 Antenna Structure

One of the interesting electrically large EM problems is antenna arrays due to their several applications such as radar, microwave terrestrial, satellite and cellular communications [4]-[6]. Many techniques have been applied to design antenna arrays [4]-[6]. Yuan *et al.* proposed the design and analysis of phased antenna arrays using the precorrected Fast Fourier Transform (FFT) method to accelerate the entry computational process [49]. Moreover, the GA, Memetic Algorithm (MA) and Tabu Search Algorithm (TSA) optimization techniques are proposed to design both uniform and non-uniform spacing linear antenna arrays. The optimum spacing can be determined for the minimum side lobe level (SLL) of linear antenna arrays [61]. In this chapter, uniform and non-uniform spacing collinear dipole antenna arrays are designed by the MSMM with the SA algorithm and the GA, called the MSMM/SA/GA method. The antenna structure is shown in Fig. 5.1. For uniform spacing collinear dipole antenna array, the distances between each element ($L_{z,k}$) are equal to each other. The MSMM/SA method is applied to compute the exact current distributions on each element of collinear dipole antenna

arrays in free space, including exact radiation patterns. In addition, antenna array parameters are optimized by the GA to minimize the SLL.

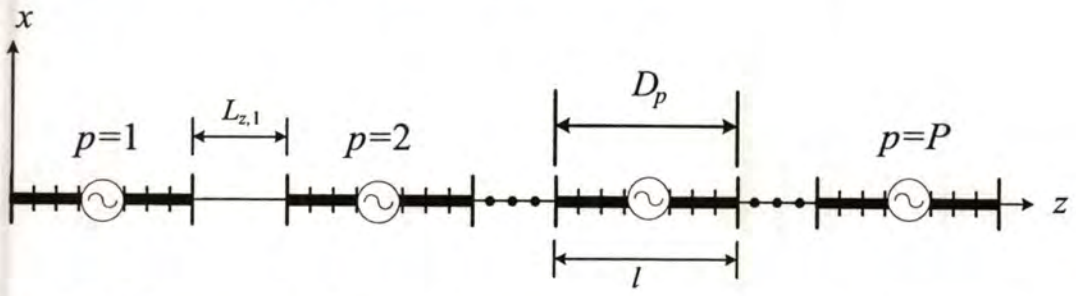

Figure 5.1 Geometry of a collinear dipole antenna array of P elements of identical length l in free space.

5.3 Design Procedure

5.3.1 The MSMM/GA Design Procedure

In this section, the MSMM/GA design procedure is discussed for collinear dipole antenna arrays in free space. Using the advantages of the MSMM and the GA, the MSMM is employed to provide good estimation of the exact current distributions on each element of collinear dipole antenna arrays, and the GA is employed to determine the optimum array parameters. Figure 5.2 shows the flow chart of the MSMM/GA antenna design procedure. The design procedure starts with the initial array parameters, and computes the current distribution on each section ($\overline{I}_{p,est}$) by the first few MSMM sweeps since it contains dominant and higher-order radiation/scattering mechanisms. The radiation pattern is then estimated by $\overline{I}_{p,est}$. Subsequently, the array parameters are adjusted by the GA until the optimum parameters are determined to achieve a desired goal. In this chapter, the simple GA is used, which consists of the roulette-wheel selection, cross over operator and mutation operator [62]-[64]. In the next section, numerical results are presented to demonstrate the accuracy and efficiency of the MSMM/GA antenna design procedure.

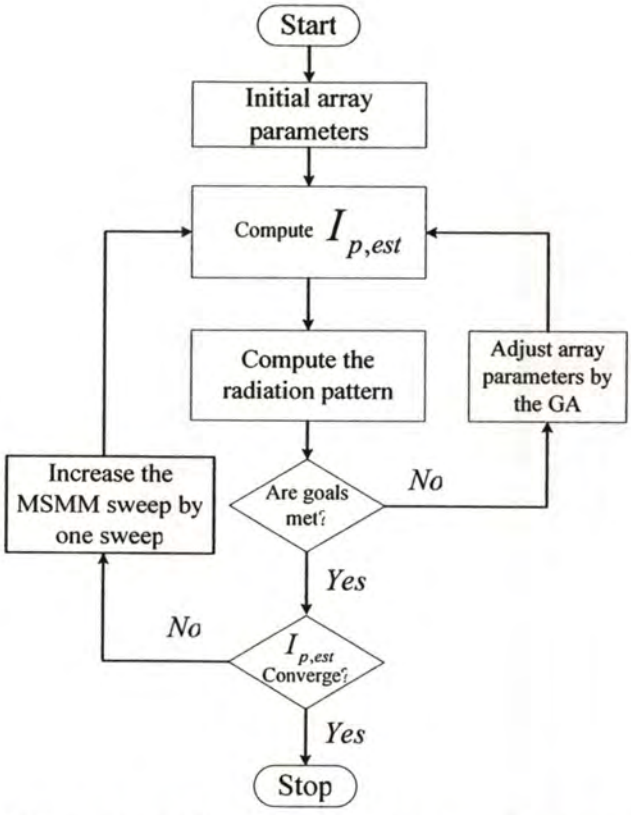

Figure 5.2 Flow chart of the MSMM/GA antenna design procedure.

5.3.2 The MSMM/GA/SA Design Procedure

For more efficiency, the SA algorithm is employed to accelerate the MSMM to be $O(N)$, called the MSMM/SA/GA method. The MSMM/SA/GA antenna array design procedure is also discussed for collinear dipole antenna arrays in free space. The MSMM and the SA algorithm are employed to compute the exact current distributions on each element of collinear dipole antenna arrays, including exact radiation patterns, and the GA is employed to determine the optimum array parameters. The design procedure starts with the initial array parameters, and estimates the current distribution on each section ($I_{p,est}$) by first using the first few sweeps (t = 3) since it contains dominant and higher-order radiation/scattering mechanisms. The radiation pattern is also estimated by using $I_{p,est}$. Subsequently, the parameters of antenna arrays are adjusted by the GA until the optimum parameters are determined to achieve desired goals. Then, the estimated current distribution $I_{p,est}$ is checked for convergence to ensure its accuracy. If it is not converged,

the number of the MSMM/SA sweeps is increased by one sweep, and the array parameters are optimized again as shown in Fig. 5.3. In the next section, numerical results are presented to demonstrate the accuracy and efficiency of the MSMM/SA/GA antenna design procedure.

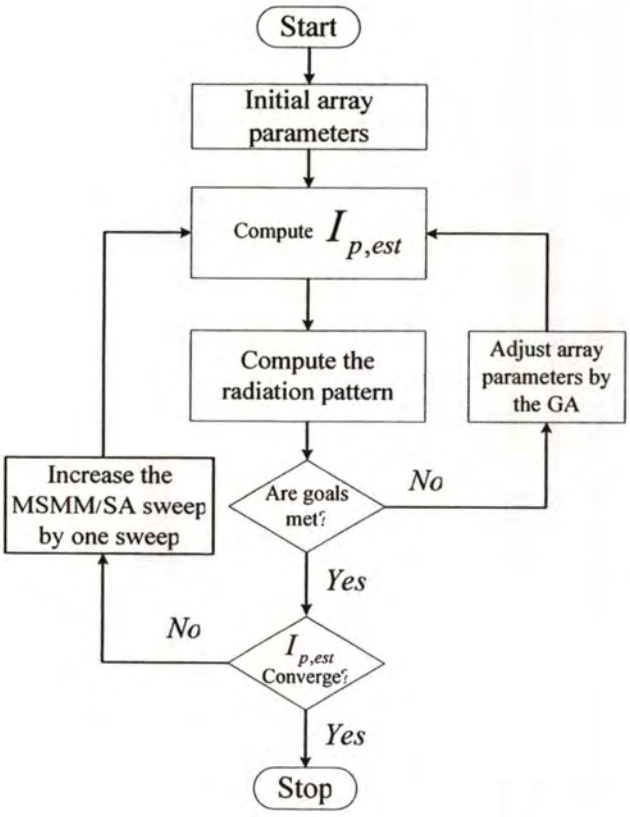

Figure 5.3 Flow chart of the MSMM/SA/GA antenna array design procedure.

5.4 Numerical Results

5.4.1 Uniform Spacing Collinear Dipole Antenna Array

5.4.1.1 MSMM/GA Method

A uniform spacing collinear dipole antenna arrays with 25 elements in free space with $l = 0.5\lambda$ is considered for MSMM/GA method, and $L_{z,k}$ is optimized by the GA. Nine PWS basis functions for each dipole element with the radius of 0.05λ are employed, and each element is excited by the 1 Volt at the center. In this study, 20 populations, the

crossover of 80%, the mutation of 5% and the elitism with 5 best populations are employed to optimize the spacing of each array element to achieve the minimum SLL.

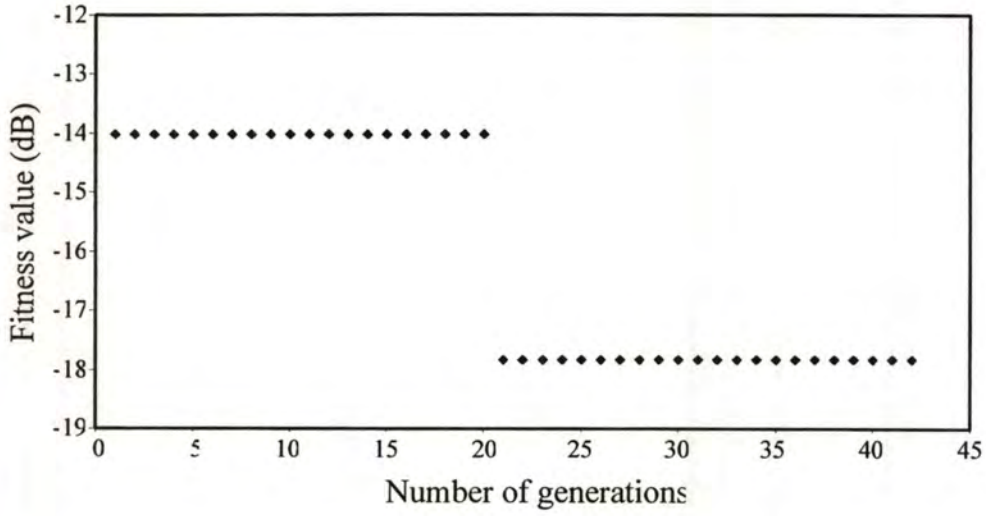

Figure 5.4 The convergence of the best fitness value of the GA of the uniform spacing collinear dipole antenna array of 25 elements.

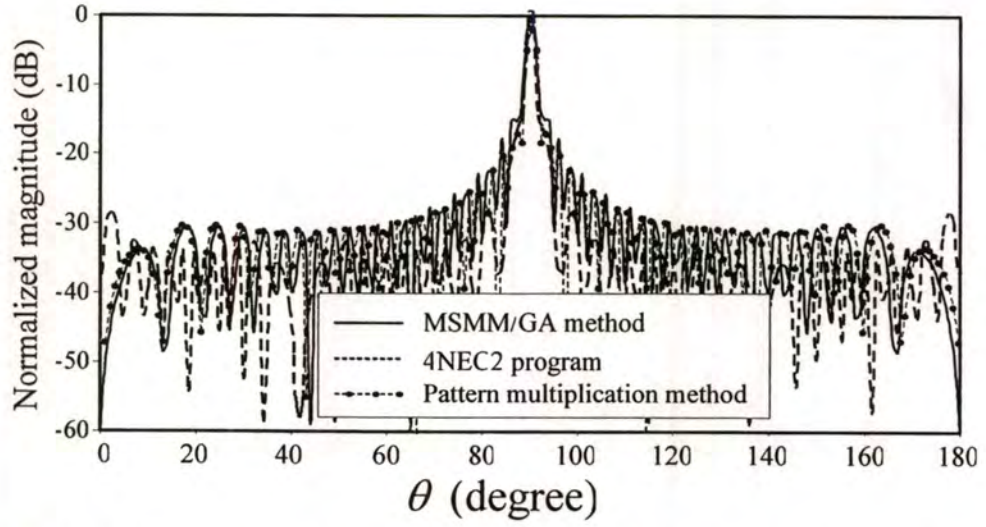

Figure 5.5 The *E*-plane radiation patterns of the optimum uniform spacing collinear dipole antenna array of 25 elements of the MSMM/GA method, the 4NEC2 program and the pattern multiplication method.

Figure 5.4 shows the best fitness value for each generation of the GA. It is found that the GA is converged rapidly during the 1st generation to the 20th generation. Then, the convergence of the GA is slow down. It is found that the minimum fitness value (or the minimum SLL) at the 44th generation is equal to -17.45 dB. The optimum spacing of each array element is 0.446λ. Moreover, Fig. 5.5 shows the E-plane radiation pattern of the optimum 25 elements of uniform spacing collinear dipole antenna array in free space, compared between the MSMM/GA method with 3 MSMM sweeps, the 4NEC2 program [65], and the pattern multiplication method. It should be pointed out that the 4NEC2 program and the pattern multiplication method employ the optimum spacing obtained from the MSMM/GA method. It is found that the radiation pattern of the MSMM/GA method (3 MSMM sweeps) is quite in good agreement with that of the 4NEC2 program.

5.4.1.2 MSMM/SA/GA method

A larger uniform spacing collinear dipole antenna arrays with 100 elements in free space is considered for MSMM/SA/GA method, where $l = 0.5\lambda$ and $L_{z,p}$ is optimized by the GA. Nine PWL basis functions for each dipole element with the radius of 0.005λ are employed, and each element is excited by the 1 Volt at the center. In this study, 20 populations, the crossover of 80%, the mutation of 5% and the elitism with 5 best populations are employed to optimize the spacing of each array element to achieve the minimum SLL.

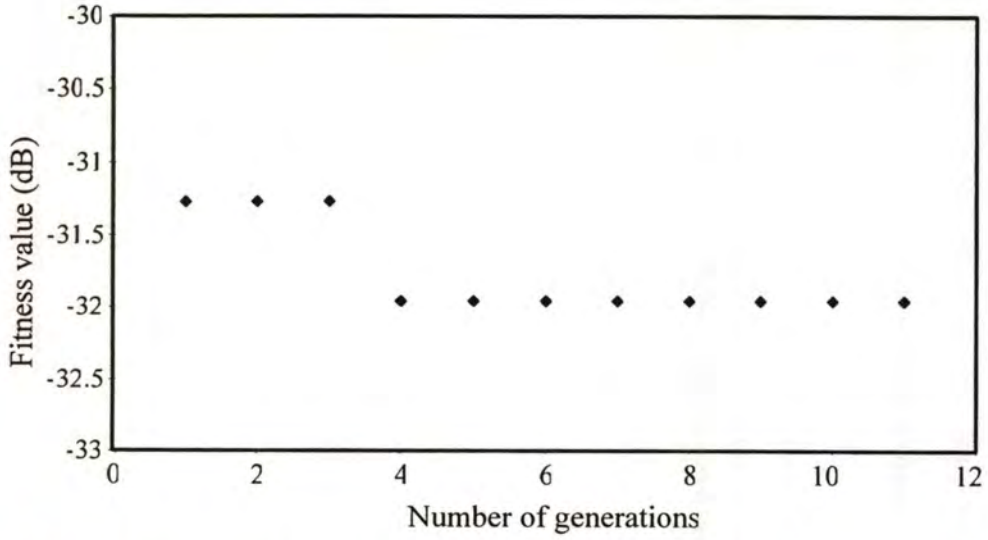

Figure 5.6 The convergence of the best fitness value of the GA of the uniform spacing collinear dipole antenna array of 100 elements.

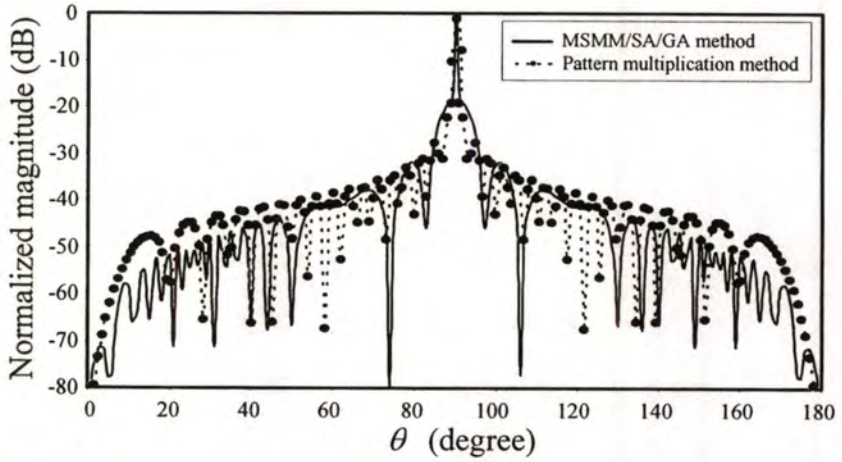

Figure 5.7 The *E*-plane radiation patterns of the optimum uniform spacing collinear dipole antenna array of 100 elements of the MSMM/SA/GA method, the 4NEC2 program and the pattern multiplication method.

5.4.2 Non-uniform Spacing Collinear Dipole Antenna Array

5.4.2.1 MSMM/GA Method

A non-uniform spacing collinear dipole antenna array with 12 elements in free space with $l = 0.5\lambda$ is considered as the first example for the MSMM/GA method, where

$L_{z,p}$ is optimized by the GA. Five PWS basis functions for each dipole element with the radius of 0.05λ are employed, and each element is excited by the 1 Volt at the center. In this study, 20 populations, the crossover of 80%, the mutation of 5% and the elitism with 5 best populations are employed to optimize the spacing of each array element to achieve the minimum SLL.

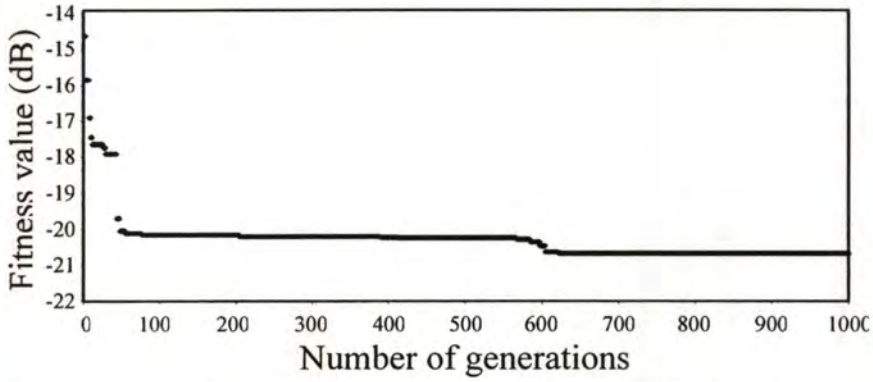

Figure 5.8 The convergence of the best fitness value of the GA of the uniform spacing collinear dipole antenna array of 12 elements.

Figure 5.8 shows the best fitness value for each generation of the GA. It is found that the GA is converged rapidly during the 1st generation to the 50th generation. Then, the convergence of the GA is slow down. It is found that the minimum fitness value (or the minimum SLL) at the 1,000th generation is equal to -20.68 dB. The optimum spacing of each array element is shown in Table 5.1.

Table 5.1. The optimum spacing of the non-uniform spacing collinear dipole antenna array of 12 elements obtained by the MSMM/GA method.

Parameters in λ	$L_{z,1}$	$L_{z,2}$	$L_{z,3}$	$L_{z,4}$	$L_{z,5}$	$L_{z,6}$	$L_{z,7}$	$L_{z,8}$	$L_{z,9}$	$L_{z,10}$	$L_{z,11}$
	0.53	0.42	0.18	0.02	0.18	0.14	0.04	0.20	0.35	0.37	0.56

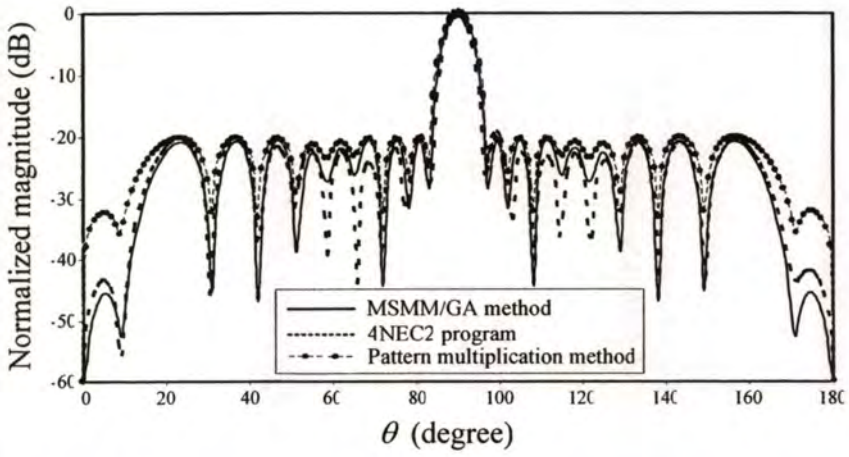

Figure 5.9 The *E*-plane radiation patterns of the optimum non-uniform spacing collinear dipole antenna array with 12 elements of the MSMM/GA method, the 4NEC2 program and the pattern multiplication method.

Figure 5.9 shows the *E*-plane radiation pattern of the optimum 12-element non-uniform spacing collinear dipole antenna array in free space, compared between the MSMM/GA method with 3 MSMM sweeps, the 4NEC2 program, and the pattern multiplication method. It should be pointed out that the 4NEC2 program and the pattern multiplication method employ the optimum spacing shown in Table 5.1. as well. It is found that the radiation pattern of the MSMM/GA method (3 MSMM sweeps) is quite in good agreement with that of the 4NEC2 program. In addition, the pattern multiplication method provides reasonable result compared with that of the 4NEC2 program except for some side lobes. However, the MSMM/GA method provides more accurate radiation pattern than the pattern multiplication method due to the fact that dominant and higher-order radiation/scattering mechanisms are included in the first few MSMM sweeps. In addition, Fig. 5.10 shows the normalized magnitude of the current distribution of each element of the optimum array. It is demonstrated that the current of the MSMM includes the mutual coupling from other array elements. This result confirms that the MSMM is more accurate than the pattern multiplication method.

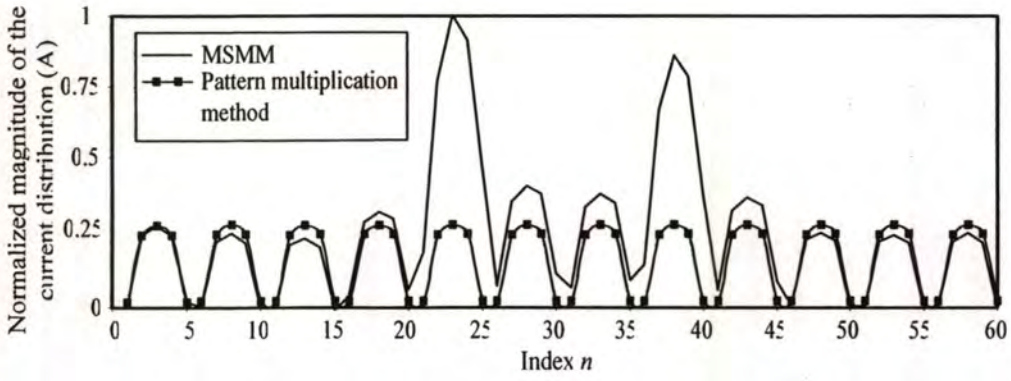

Figure 5.10 Current distribution of the optimum non-uniform spacing collinear dipole antenna array of 12 elements of the MSMM and the pattern multiplication method.

For the second example, a larger non-uniform spacing collinear dipole antenna arrays of 22 elements in free space with $l = 0.5\lambda$ is considered, where $L_{z,k}$ is optimized by the GA. Like the first example, Five PWS basis functions for each dipole element with the radius of 0.005λ are employed, and each element is excited by the 1 Volt at the center. The GA can be used to determine the optimum array parameters for the minimum SLL within 500 generations as shown in Fig. 5.11. The optimum spacing of each array element are shown in Table 5.2. The SLL is found to be -18.37 dB. In Fig. 5.2, the *E*-plane radiation patterns of the optimum array compared between the MSMM/GA method with 3 MSMM sweeps, the 4NEC2 program, and the pattern multiplication method. Similar observations are found as in the first example.

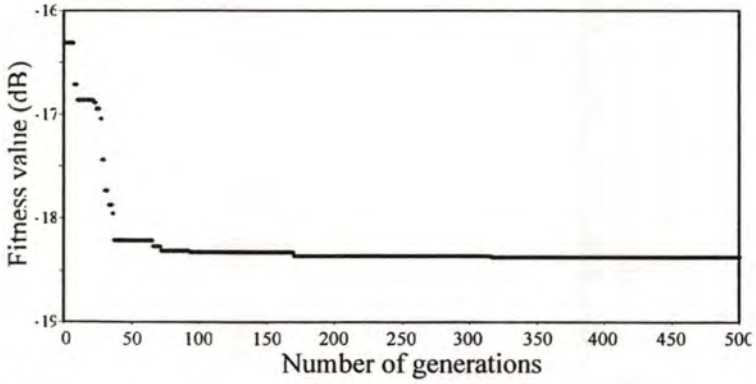

Figure 5.11 The convergence of the best fitness value of the GA of the non-uniform spacing collinear dipole antenna array of 22 elements.

Table 5.2 The optimum spacing of the non-uniform spacing collinear dipole antenna array of 22 elements obtained by the MSMM/GA method.

Parameters in λ					
$L_{z,1}$	0.96	$L_{z,8}$	0.47	$L_{z,15}$	0.48
$L_{z,2}$	0.28	$L_{z,9}$	0.39	$L_{z,16}$	0.07
$L_{z,3}$	0.80	$L_{z,10}$	0.19	$L_{z,17}$	0.80
$L_{z,4}$	0.70	$L_{z,11}$	0.51	$L_{z,18}$	0.74
$L_{z,5}$	0.39	$L_{z,12}$	0.18	$L_{z,19}$	0.67
$L_{z,6}$	0.55	$L_{z,13}$	0.03	$L_{z,20}$	0.27
$L_{z,7}$	0.25	$L_{z,14}$	0.31	$L_{z,21}$	0.47

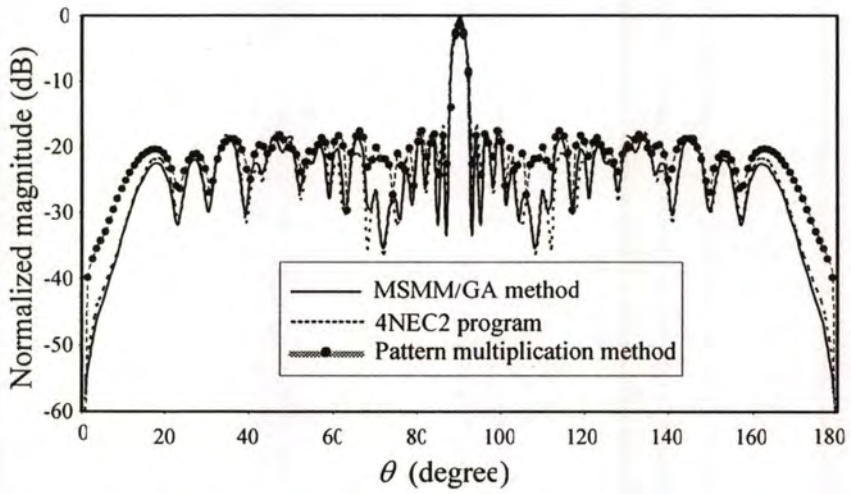

Figure 5.12 *E*-plane radiation patterns of the optimum non-uniform spacing collinear dipole antenna array of 22 elements of the MSMM/GA method, the 4NEC2 program and the pattern multiplication method.

5.4.2.2 MSMM/SA/GA Method

A larger non-uniform spacing collinear dipole antenna array with 500 elements in free space with $l = 0.5\lambda$ is considered, where $L_{z,k}$ is optimized by the GA. Five PWL functions for each dipole element with the radius of 0.005λ are employed, and each

element is excited by the 1 Volt at the center. Note that these PWC functions are sufficient for estimate the radiation pattern of the collinear dipole antenna array. In this study, the MSMM/SA method first few sweeps are equal to 3 sweeps (t = 3), 50 populations, the crossover of 80%, the mutation of 5% and the elitism with 5 best populations are employed to optimize the spacing of each array element to minimize the SLL. It is found that the GA can be converged to the optimum array parameters within the 50 iterations. The best fitness value of each iteration is shown in Fig. 5.13, which the minimum SLL is equal to -33.81 dB.

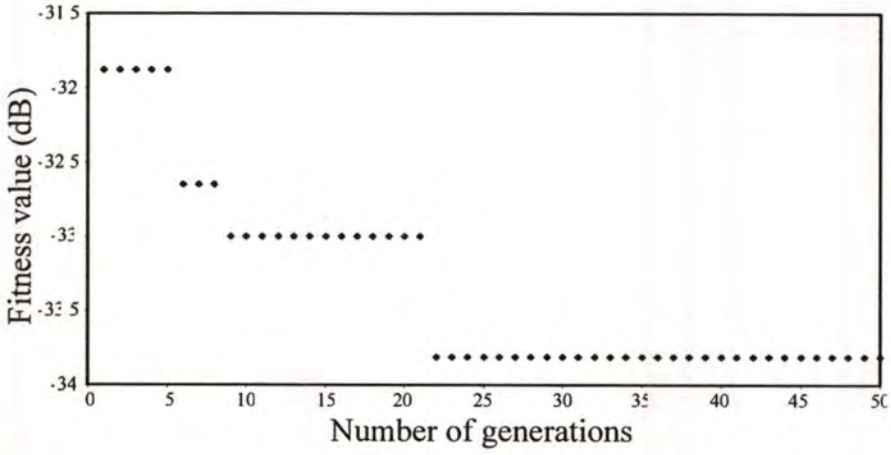

Figure 5.13 The convergence of the best fitness value of the GA of the non-uniform spacing collinear dipole antenna array of 500 elements.

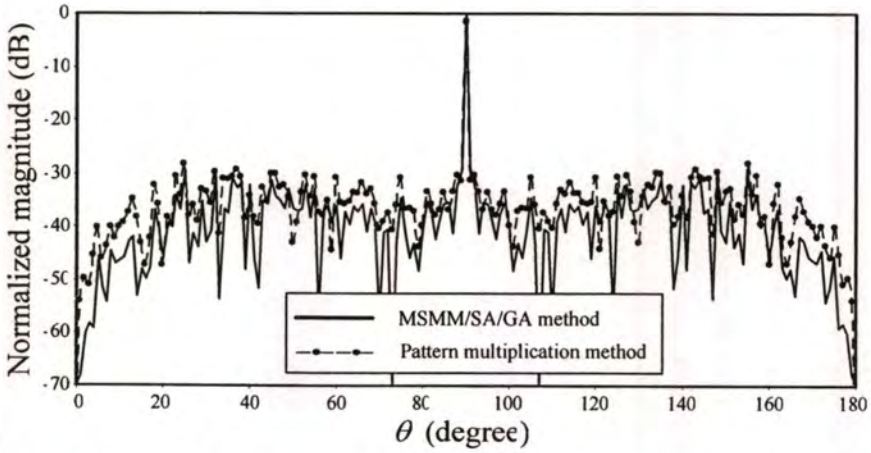

Figure 5.14 *E*-plane radiation patterns of the non-uniform spacing collinear dipole antenna array of 500 elements of the MSMM/SA/GA method and the pattern multiplication method.

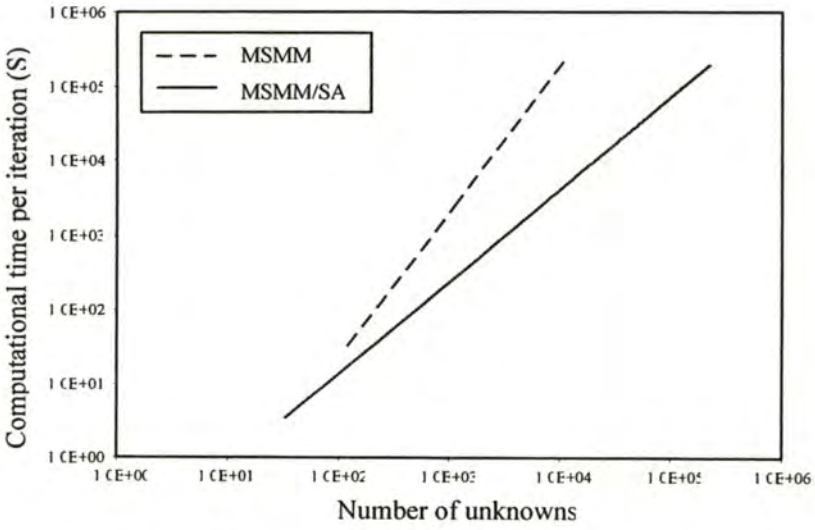

Figure 5.15 The computational time per iteration of the MSMM and MSMM/SA methods.

In addition, the *E*-plane radiation patterns of the 500-element non-uniform spacing collinear dipole antenna array in free space, compared between the MSMM/SA/GA method and the pattern multiplication method, are shown in Fig. 5.14. It should be pointed out that the pattern multiplication method employs the optimum spacing as used in the MSMM/SA/GA method. In Fig. 5.14, it is found that the MSMM/SA/GA method provides more accurate radiation pattern than the pattern multiplication method due to the fact that the exact current distributions on each array element are used in the former one. In addition, Fig. 5.15 shows the computational time per iteration of the MSMM/SA method compared with the MSMM for a collinear dipole antenna array with l=0.5λ, L_s =3λ, and appropriate SA parameters [60]. It is obvious that the computational time per iteration of the MSMM/SA method tends to be $O(N)$ with the array increment in one direction, while that of the MSMM tends to be $O(N^2)$.

5.5 Conclusions

The MSMM/GA method can be efficiently applied to design uniform and non-uniform spacing collinear dipole antenna arrays in free space. For the considered arrays, the MSMM/GA antenna design procedure yields the optimum array parameters with the minimum SLL. In addition, the MSMM/GA method provides more accurate radiation

pattern than the pattern multiplication method, especially at side lobes. Moreover, the SA algorithm is incorporated into the MSMM/GA method to accelerate the computational time for electrically large collinear dipole antenna arrays. The MSMM/SA/GA method can be efficiently applied to design electrically large uniform and non-uniform spacing collinear dipole antenna arrays in free space. Numerical results are presented to demonstrate the design procedure, including the accuracy and efficiency of the MSMM/SA/GA method. In addition, it is found that the MSMM/SA/GA method provides more accurate radiation pattern than the pattern multiplication method.

CHAPTER 6
CONCLUSIONS

6.1 Summary of the Thesis

In this thesis, the efficient hybrid method is proposed. The hybrid method appropriately combines the MSMM and the CG method, called the hybrid MSMM/CG method, yielding better convergence rate. After that, the SA algorithm is incorporated with the hybrid MSMM/CG method to improve its efficiency to be $O(N)$ for both of the computational time and memory requirement. Moreover, uniform and non-uniform dipole antenna arrays are considered as examples.

In Chapter 2, the MSMM can be effectively applied to analyze both uniform and non-uniform collinear and planar dipole antenna arrays with collinear and planar configurations in free space, which usually provides relatively fast convergence rate with additional physical insight into radiation/scattering mechanisms. The row and sawtooth MSMM sweeps are proposed in this chapter. It is found that the latter is more efficient than the former because the associated number of unknowns for each section of the row sweep is relatively large. In addition, the latter exhibits faster convergent than the CG method without any fluctuation for the examples of interest. Furthermore, numerical MSMM results of both uniform and non-uniform dipole antenna arrays are in excellent agreement with those of the MM.

Chapter 3 presents the hybrid MSMM/CG method to achieve the convergence rate benefits. The method is effectively employed to analyze both uniform and non-uniform dipole antenna arrays with collinear and planar configurations in free space with relatively fast convergence rate. Several numerical results are presented to validate the hybrid approach. It is found that the results of the hybrid MSMM/CG method are in excellent agreement with those of the MM. It shows that the hybrid MSMM/CG method can improve the convergence rate of solutions without sacrificing accuracy.

Chapter 4 presents the basic theory of the SA algorithm and its conventional formulation. The SA's procedure is elucidated with the flow chart. For enhance the SA integration parameters, the GA optimization is employed to find the optimum SA integration parameters. It is found that the GA can be applied to optimize the SA integration parameter to the minimum percentage of error and minimum

computational time. Moreover, the SA algorithm is incorporated to the hybrid MSMM/CG method. The hybrid MSMM/CG/SA method can be efficiently applied to analyze an electrically large uniform and non-uniform spacing dipole antenna arrays in free space. In addition, it is obvious that the computational time per iteration of the hybrid MSMM/CG/SA method tends to be $O(N)$ with the array increment in one direction, while that of the hybrid MSMM/CG method tends to be $O(N^2)$.

Chapter 5 shows the MSMM/SA/GA method to automatically design collinear dipole antenna arrays. The MSMM/GA method can be efficiently applied to design uniform and non-uniform spacing collinear dipole antenna arrays in free space. For the considered arrays, the MSMM/GA antenna design procedure yields the optimum array parameters with the minimum SLL. In addition, the MSMM/GA method provides more accurate radiation pattern than the pattern multiplication method, especially at side lobes. Moreover, the SA algorithm is incorporated into the MSMM/GA method to accelerate computational time for electrically large collinear dipole antenna arrays. It is found that, the MSMM/SA/GA method can be efficiently applied to design electrically large uniform and non-uniform spacing collinear dipole antenna arrays in free space.

6.2 Remarks and Future Studies

In this thesis, the antenna arrays in free space are analyzed, which it can be a good example for the hybrid MSMM/CG/SA method. However, the EM problems have a lot of applications involving in other antenna structure and other environment. Therefore, the Hybrid/MSMM/CG/SA method will be extended for extremely large planar arrays for multilayer structures involving a spectral integral representation of the multilayer Green's function. In addition, a Graphic User Interface (GUI) for the computation of planar antenna arrays will be developed to be a useful educational tool for teaching students. The GUI is an important part of any software for attracting users. I will develop the GUI to be attractive and easy to use. Moreover, the Genetic Algorithm (GA) will be incorporated into the software for using in the automatic design of antenna arrays. In the literature, the GA has been successfully applied to several antenna design problems. In conclusion, the software will contain three parts; i.e., the GUI, the Hybrid/MSMM/CG/SA method for solving electrically large antenna arrays, and the GA for optimization purpose.

APPENDICES

APPENDIX A

A. Genetic Algorithm (GA) Optimization

The Genetic Algorithm (GA) is the optimization tool, which it is a robust search and global optimization. The GA has been presented to use with many applications in the EM problems. It is effective at solving complex problem. Table A.1 shows the GA optimization compared qualitatively to the CG and the random search. In this thesis, the simple GA is used for optimize the arrays parameter and the SA's parameter. The GA theory will be presented in the next section.

Table A.1 The comparison of qualitative characteristics between the GA, the CG and the random search optimization.

Method / Qualitative Characteristics	CG	Random	GA
Global Optimization			✓
Discontinuous Object Function		✓	✓
Non-differentiable Object Function		✓	✓
Convergence Rate	✓		

A.1 The GA procedure

The GA procedure is shown in Fig. A.1. It starts by the assign the optimize parameter and then the optimize parameter is defined to the gene and gene is combined to the chromosome. The chromosome group is called the population, which it is the initial value for the first generation. After the initial value of the population, each population is evaluated the fitness value. Then, the population group are selected by the selection algorithm for reproduce the new population and evaluate the fitness value of each population again. This procedure is repeated until the criterion is met. In general, a GA optimizer must be able to perform the basic steps as follows:

1. Encode the solution parameters as genes.
2. Create a string of the genes to form a chromosome.
3. Initialize a starting population by creating a set of specific chromosomes, usually in a randomized manner.
4. Evaluate and assign fitness values to individuals in the population.
5. Perform reproduction through the fitness-weighted selection of individuals from the population.
6. Perform recombination (crossover) and mutation to produce individuals of the next generation.

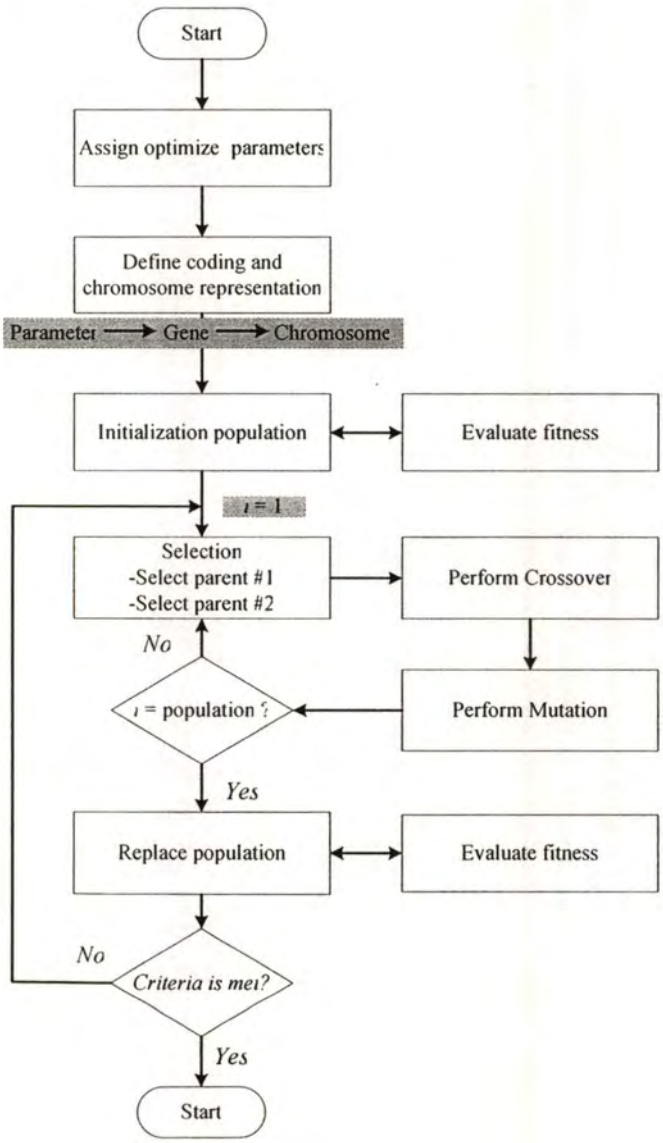

Figure A.1 The GA optimization procedure.

A.2 The GA operator

A.2.1 Selection operator

A.2.1.1 Roulette wheel selection

The most popular of the stochastic selection is the proportionate selection or roulette wheel selection. In this selection, the population are selected based on a probability of selection in (A.1), which $f(parent_i)$ is the fitness of the i^{th} parent:

$$p_{selection} = \frac{f(parent_i)}{\sum_i f(parent_i)} \tag{A.1}$$

The probability of selecting an individual from the population is a function of the relative fitness value of the individual. The individual with high fitness value will participate in the production of the next generation more than the less fitness value of the individuals. This is the removal of the least fitness value and keep a good fitness value for subsequent generation. Figure A.2 shows the roulette wheel process, which the fitness value of each individual is assigned as the space in the wheel. Then, the wheel is spun and the individual is pointed at the end of the spin.

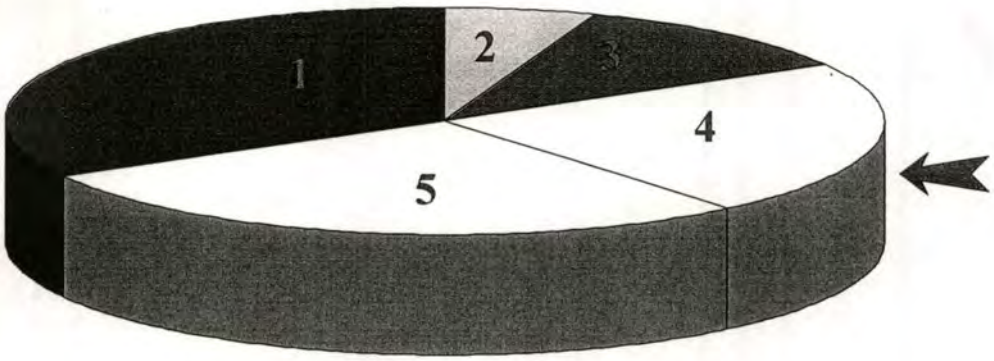

Figure A.2 The roulette wheel selection process.

A.2.1.2 Tournament selection

The tournament selection is one of the popular selection method, which it is depicted in Fig. A.3. In the tournament selection, the subpopulation of N individuals is chosen by random from the population. The individual of the subpopulation is competed on the basis of their fitness value. The individual in the subpopulation with

the highest fitness wins the tournament and becomes the selected individual. All of the subpopulation members are placed into the general population and the selecting process is repeated.

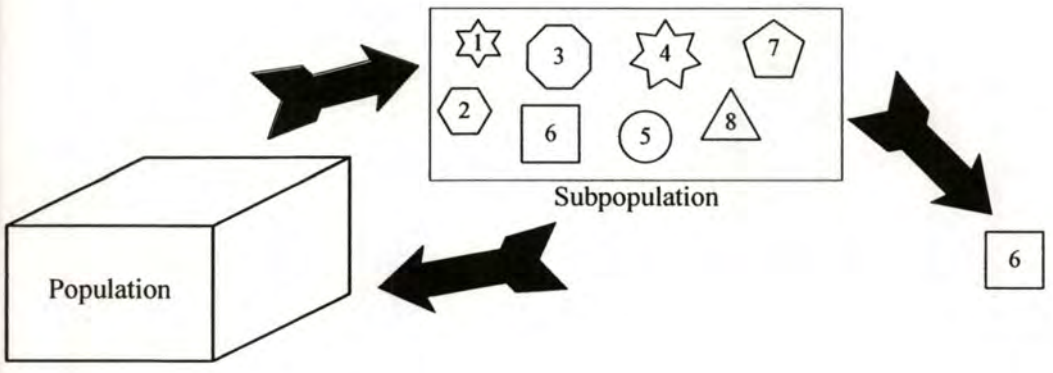

Figure A.3 The tournament selection process

A.2.2 Crossover operator

The crossover operator is the operator of the GA optimization for reproduce the new chromosome. It is process by using the selected two of the best chromosome and separate the both of chromosome by random point. Then, it will be swap the separated chromosome as shown in Fig. A.4.

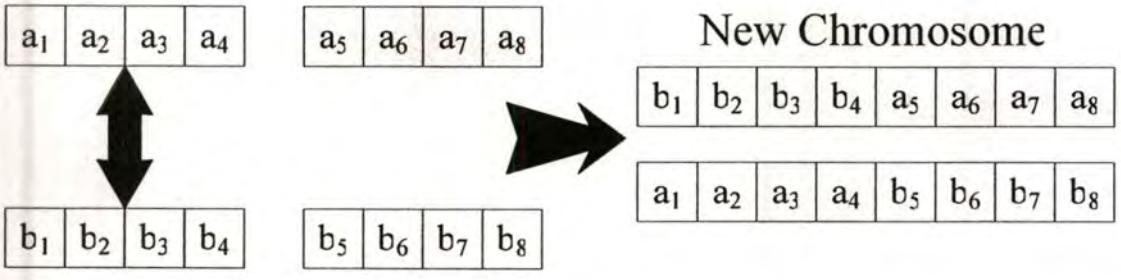

Figure A.4 The crossover operator process.

A.2.3 Mutation operator

The mutation operator provides a means for exploring portions of the solution surface. In mutation, an element in the string of the chromosome is randomly selected and changed. In the case of the binary coding, the selecting bit from the chromosome string is inverted such as from "1" to "0" or "0" to "1" as shown in Fig. A.5.

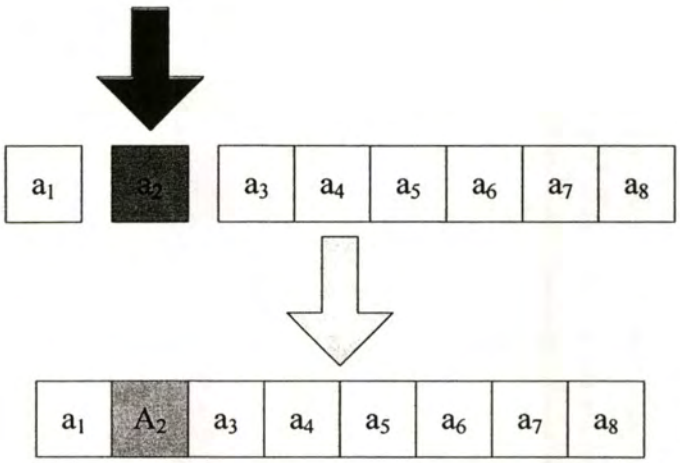

Figure A.5 The mutation operator process.

A.2.4 Fitness function

The fitness function is used to assign the fitness value to each of the individuals in the GA population, it is sometimes called "objective function". The fitness function is the function that connection between the physical problem and the genetic algorithm. In the GA, it is possible to have more than one fitness function, which called multi objective function.

APPENDIX B

B. Radiation Pattern

An antenna radiation pattern is defined as a mathematical function of the radiation properties of the antenna as a function of space coordinates. The field and power patterns are normalized with respect to their maximum value, yielding normalized field and power patterns. In this appendix, the radiated field of the half wave dipole is discussed in detail. One of the most commonly used antennas is the half-wavelength ($l = \lambda/2$) dipole. Because its radiation resistance is 73 ohms, which is very near the 50-ohm or 75-ohm characteristic impedances of the transmission lines. Because of its wide acceptance in practice, we will examine in a little more detail its radiation characteristics. The electric and magnetic field components of a half-wavelength dipole can be obtained as follows [6]:

$$E_\theta = j\eta \frac{I_0 e^{-jkr}}{2\pi r}\left[\frac{\cos(\frac{\pi}{2}\cos\theta)}{\sin\theta}\right] \tag{B.1}$$

$$H_\phi = j\frac{I_0 e^{-jkr}}{2\pi r}\left[\frac{\cos(\frac{\pi}{2}\cos\theta)}{\sin\theta}\right] \tag{B.2}$$

In the case of array, enlarging the dimensions of single elements often leads to more directive characteristics. Another way to enlarge the dimensions of the antenna, without necessarily increasing the size of the individual elements, is to form an assembly of radiating elements in an electrical and geometrical configuration. This new antenna, formed by multielements, is referred to as an array. Inmost cases, the elements of an array are identical. This is not necessary, but it is often convenient, simpler, and more practical. The individual elements of an array may be of any form (wires, apertures, etc.). Ideally this can be accomplished, but practically it is only approached. In an array of identical elements, there are at least five controls that can be used to shape the overall pattern of the antenna [6]. These are:

1. The geometrical configuration of the overall array (linear, circular, rectangular, spherical, etc.)
2. The relative displacement between the elements.
3. The excitation amplitude of the individual elements.
4. The excitation phase of the individual elements.
5. The relative pattern of the individual elements.

B.1 Two-element array

Let us assume that the antenna under investigation is an array of two infinitesimal horizontal dipoles positioned along the z-axis, as shown in Figure B.1(a). The total field radiated by the two elements, assuming no coupling between the elements, is equal to the sum of the two and in the y-z plane it is given by [6]

$$E_t = E_1 + E_2 = \hat{a}_\theta j\eta \frac{kI_0 l}{4\pi}\left\{\frac{e^{-j[kr_1-(\beta/2)]}}{r_1}\cos\theta_1 + \frac{e^{-j[kr_2-(\beta/2)]}}{r_2}\cos\theta_2\right\} \quad \text{(B.3)}$$

where β is the difference in phase excitation between the elements. The magnitude excitation of the radiators is identical. Assuming far field observations and referring to Figure B.1(b),

$$\theta_1 \approx \theta_2 \approx \theta \quad \text{(B.4)}$$

$$r_1 \approx r - \frac{d}{2}\cos\theta \quad \text{(B.5)}$$

$$r_1 \approx r + \frac{d}{2}\cos\theta \quad \text{(B.6)}$$

$$r_1 \approx r_2 \approx r \quad \text{(B.7)}$$

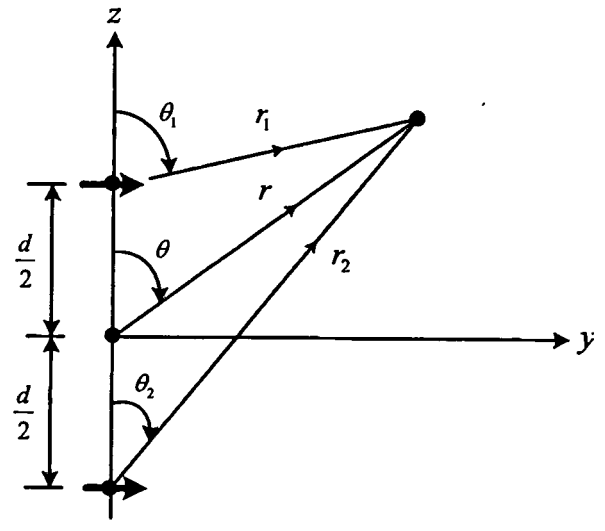

(a)

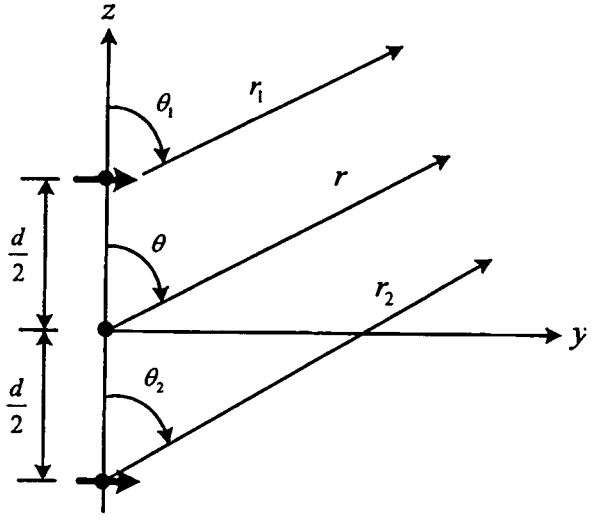

(b)

Figure B.1 Geometry of a two-element array positioned along the z-axis [6]. (a) Two infinitesimal dipoles, and (b) Far-field observations.

(B.3) reduces to

$$E_t = \hat{a}_\theta j\eta \frac{kI_0 le^{-jkr}}{4\pi r}\cos\theta\left[e^{+j(kd\cos\theta+\beta)/2} + e^{-j(kd\cos\theta+\beta)/2}\right]$$

$$E_t = \hat{a}_\theta j\eta \frac{kI_0 le^{-jkr}}{4\pi r}\cos\theta\left\{2\cos\left[\frac{1}{2}(kd\cos\theta+\beta)\right]\right\} \qquad \text{(B.8)}$$

It is apparent from (B.8) that the total field of the array is equal to the field of a single element positioned at the origin multiplied by a factor which is widely referred to as the array factor. Thus for the two-element array of constant amplitude, the array factor is given by [6]

$$AF = 2\cos\left[\frac{1}{2}\left(kd\cos\theta + \beta\right)\right] \tag{B.9}$$

which in normalized form can be written as

$$\left(AF\right)_n = \cos\left[\frac{1}{2}\left(kd\cos\theta + \beta\right)\right] \tag{B.10}$$

It has been illustrated that the far-zone field of a uniform two-element array of identical elements is equal to the product of the field of a single element, at a selected reference point (usually the origin), and the array factor of that array. That is,

$$E(total) = \left[E(\text{single element at refernce point})\right] \times \left[\text{array factor}\right] \tag{B.11}$$

This is referred to as pattern multiplication for arrays of identical elements, and it is analogous to the pattern multiplication for continuous sources. Although it has been illustrated only for an array of two elements, each of identical magnitude, it is also valid for arrays with any number of identical elements which do not necessarily have identical magnitudes, phases, and/or spacings between them [6].

REFERENCES

[1] D. Colak, "The Multiple Sweep Method of Moments (MSMM) Analysis of Three Dimensional Radiation and Scattering Problems," Dissertation of the Degree Doctor of Philosophy, Graduate School of The Ohio State University, 2000.

[2] CST Microwave Studio, 2006.

[3] [Online] Available : http://www.mst.nerc.ac.uk

[4] Constantine A. Balanis, **Advanced Engineering Electromagnetics**, New Jersey : John Wiley & Sons, 1989.

[5] Matthew N. O. Sadiku, **Numerical Techniques in Electromagnetics**, 2nd ED. New York : CRC Press LLC, 2001.

[6] Constantine A. Balanis, **Antenna Theory Analysis and Design**, 3rd ED. New Jersey : John Wiley & Sons, 2005.

[7] T. Sarkar, K. Siarkiewicz and R. Stratton, "Survey of Numerical Methods for Solution of Large Systems of Linear Equations for Electromagnetic Field Problems," *IEEE Transactions on Antennas and Propagation*, vol. 29, no. 6, pp. 847-856, 1981.

[8] C. T. Tai, "An Iterative Method of Solving a System of Linear Equations and Its Physical Interpretation from the Point of View of Scattering Theory," *IEEE Transactions on Antennas and Propagation*, vol. 29, no. 6, pp. 713-714, 1970.

[9] D. Holliday, J. L. L. Deraad, and G. J. St-Cyr, "Forward-Backward: A New Method for Computing Low-Grazing Angle Scattering," *IEEE Transactions on Antennas and Propagation*, vol. 44, pp. 722-729, 1996.

[10] D. Holliday, J. L. L. Deraad, and G. J. St-Cyr, "Forward-Backward Method for Scattering from Imperfect Conductors," *IEEE Transactions on Antennas and Propagation*, vol. 46, pp. 101-107, 1998.

[11] A. Iodice, "Forward–Backward Method for Scattering from Dielectric Rough Surfaces," *IEEE Transactions on Antennas and Propagation*, vol. 50, no. 7, pp. 901-911, 2002.

[12] C. S. Heng and D. Torrungrueng, "An Application of the Forward-Backward (FB) Method for Capacitance Extraction Problems of Planar Structures," *TENCON 2004 Conference*, vol. 4, pp. 332-335, 2004.

[13] B. Babu, C. Brennan and M. condon, "Block Forward Backward Method for Computation of Electromagnetic Wave Scattering from a Collection of Inhomogeneous Bodies," *ICEAA 2007. International Conference*, pp. 944-947, 2007.

[14] M. Mullen, C. Brennan and T. Downes, "Improved Buffered Block Forward Backward Method Applied to 3D Scattering Problems," *Computation in Electromagnetics International Conference*, pp. 32-33, 2008.

[15] H.-T. Chou and H.-K. Ho, "A Generalized Forward-Backward Method for the Efficient Analysis of Large Array Problems," *Antennas and Propagation Society International Symposium*, vol. 3, pp. 40-43, 2001.

[16] M. R. Pino, L. Landesa, J. L. Rodriguez, F. Obelleiro and R. J. Burkholder, "The Generalized Forward-Backward Method for Analyzing the Scattering from Targets on Ocean-Like Rough Surfaces," *IEEE Transactions on Antennas and Propagation*, vol. 47, no. 6, pp. 961-969, 1999.

[17] J. C. West and J. M. Sturm, "On Iterative Approaches for Electromagnetic Rough-Surface Scattering Problems," *IEEE Transactions on Antennas and Propagation*, vol. 47, no. 8, pp. 1281-1288, 1999.

[18] R. J. Adams and G. S. Brown, "A Combined Field Approach to Scattering from Infinite Elliptical Cylinders Using the Method of Ordered Multiple Interactions," *IEEE Transactions on Antennas and Propagation*, vol. 47, no. 2, pp. 364-375, 1999.

[19] C. L. Rino, K. J. Doniger and J. R. Martinez, "The Method of Ordered Multiple Interactions for Closed Bodies," *IEEE Transactions on Antennas and Propagation*, vol. 51, no. 9, pp. 2327-2334, 2003.

[20] D. Colak, R. J. Burkholder, and E. H. Newman, "Multiple Sweep Method of Moments Analysis of Electromagnetic Scattering from 3D Targets on Ocean-Like Rough Surfaces," *Microwave and Optical Technology Letter*, vol. 49, no. 1, pp. 241-247, 2007.

[21] J. I. H.-Herruzo, A. V. Nogueira and M. F. Bataller, "Optimization Technique for Linearly Polarized Radial-Line Slot-Array Antennas Using the Multiple Sweep Method of Moments," *IEEE Transactions on Antennas and Propagation*, vol. 52, no. 4, pp. 1015-1023, 2004.

[22] D. Torrungrueng and E. H. Newman, "The Multiple Sweep Method of Moments (MSMM) Analysis of Electrically Large Bodies," *IEEE Transactions on Antennas and Propagation*, vol. 45, no. 8, pp. 1252-1258, 1997.

[23] D. Colak and E. H. Newman, "Thye Multiple Sweep Method of Moments (MSMM) Design of Wide-Band Antennas," *IEEE Transactions on Antennas and Propagation*, vol. 46, no. 9, pp. 1365-1371, 1998.

[24] D. Torrungrueng, "The Multiple Sweep Method of Moments (MSMM) Analysis of Electrically Large Bodies," MSc thesis, Ohio State University, Columbus, OH, June 1996.

[25] T. K. Sarkar, "The Conjugate Gradient Method as Applied to Electromagnetic Field Problems," *IEEE Antennas and Propogation Society Newletter*, pp. 4-14, 1986.

[26] K. Nayanthara, S. M. Rao, and T. K. Sarkar, "Analysis of Two-Dimensional Conducting and Dielectric Bodies Utilizing the Conjugate Gradient Method," *IEEE Transactions on Antennas and Propagation*, vol. AP-35, no. 4, pp. 451-453, 1987.

[27] R. Devayya and D. J. Wingham, "The Numerical Calculation of Rough Surface Scattering by the Conjugate Gradient Method," *IEEE Transactions on Geoscience and Remote Sensing*, vol. 30, no. 3, pp. 645-648, 1992.

[28] V. V. Sanjaynath, N. Balakrishnam, and G. R. Nagabhushana, "Application of Conjugate Gradient Method for Static Problems Involving Conductors of Arbitrary Shape," *IEEE Transactions on Antennas and Propagation*, vol. 42, no. 7, pp. 1028-1033, 1994.

[29] H. Harada, D. J. N. Wall, T. Takenaka, and M. Tanaka, "Conjugate Gradient Method Applied to Inverse Scattering Problem," *IEEE Transactions on Antennas and Propagation*, vol. 43, no. 8, pp. 784-792, 1995.

[30] P. M. Van Den Berg, E. Korkmaz, and A. Abubakar, "A Constrained Conjugate Gradient Method for Solving the Magnetic Field Boundary Integral Equation," *IEEE Transactions on Antennas and Propagation*, vol. 51, no. 6, pp. 1168-1176, 2003.

[31] C. F. Smith, A. F. Peterson, and R. Mittra, "The Biconjugate Gradient Method for Electromagnetic Scattering," *IEEE Transactions on Antennas and Propagation*, vol. 38, no. 6, pp. 938-940, 1990.

[32] X. Xu, Q. H. Liu, and Z. Q. Zhang, "The Stabilized Biconjugate Gradient Fast Fourier Transform Method for Electromagnetic Scattering," *Antennas and Propagation Society International Symposium*, vol. 2, pp. 614-617, 2002.

[33] A. P. C. Fourie and D. C. Nitch, "Comparing the Sparse Iterative Method (SIM) with the Banded Jacobi and Conjugate Gradient Techniques," *Antennas and Propagation Society International Symposium*, vol. 2, pp. 1181-1184, 1994.

[34] R. L. Dreyer and A. R. Clark, "Preliminary Results for Simply Sparse as a Preconditioner to SIM," *Antennas and Propagation Society International Symposium*, vol. 2, pp. 238-241, 2002.

[35] A. R. Clark, A. P. C. Fourie, and D. C. Nitch, "Stationary, Nonstationary, and Hybrid Iterative Method of Moments Solution Schemes," *IEEE Transactions on Antennas and Propagation*, vol. 49, no. 10, pp. 1462-1469, 2001.

[36] B. Dembart and E. Yip, "The Accuracy of Fast Multipole Methods for Maxwell's Equations," *IEEE Computational Science & Engineering*, vol. 5, no. 3, pp. 48-56, 1998.

[37] Z. Zhao, J. Liu, and X. Cui, "The Fast Multipole Method for Analysis of Electromagnetic Scattering from Thin-wire Antennas," *WAC Automation Congress*, pp. 1-4, 2008.

[38] J. M. Song and W. C. Chew, "Fast Multipole Method Solution of Three Dimensional Integral Equation," *Antennas and Propagation Society International Symposium*, vol. 3, pp. 1528-1531, 1995.

[39] N. Geng, A. Sullivan, and L. Carin, "Fast Multipole Method for Scattering from an Arbitrary PEC Target Above or Buried in a Lossy Half Space," *IEEE Transactions on Antennas and Propagation*, vol. 49, no. 5, pp. 740-748, 2001.

[40] Y. Takahashi and S. Wakao, "Large-Scale Analysis of Eddy-Current Problems by the Hybrid Finite Element-Boundary Element Method Combined with the Fast Multipole Method," *IEEE Transaction on Magnetics*, vol. 42, no. 4, 2006.

[41] Y. Takahashi, S. Wakao, K. Fujiwara, and S. Fujino, "Large-Scale Magnetic Field Analysis of Laminated Core by Using the Hybrid Finite Element and Boundary Element Method Combined with the Fast Multipole Method," *IEEE Transactions on Magnetics*, vol. 43, no. 6, 2007.

[42] K. Sertel, and J. L. Volakis, "Multilevel Fast Multipole Method Solution of Volume Integral Equations Using Parametric Geometry Modeling," *IEEE Transactions on Antennas and Propagation*, vol. 52, no. 7, pp. 1686-1692, 2004.

[43] D. Z. Ding, R. S. Chen, and Z. H. Fan, "An Efficient Sai Preconditioning Technique for Higher Order Hierarchical MLFMM Implementation," *Progress in Electromagnetic Research*, PIER 88, pp. 255-273, 2008.

[44] P. L. Rui, R. S. Chen, Z. W. Liu, and Y. N. Gan, "Schwarz-Krylov Subspace Method for MLFMM Analysis of Electromagnetic Wave Scattering Problems," *Progress in Electromagnetic Research*, PIER 82, pp. 51-63, 2008.

[45] D. Z. Ding, R. S. Chen, and Z. H. Fan, "SSOR Preconditioned Inner-Outer Flexible GMRES Method for MLFMM Analysis of Scattering of Open Objects," *Progress in Electromagnetic Research*, PIER 89, pp. 339-357, 2009.

[46] T. K. Sarkar, E. Arvas, and S. M. Rao, "Application of FFT and the Conjugate Gradient Method for the Solution of Electromagnetic Radiation from Electrically Large and Small Conducting Bodies," *IEEE Transactions on Antennas and Propagation*, vol. AP-34, no. 5, pp. 635-640, 1986.

[47] X. M. Xu, and Q. H. Liu, "The BCGS-FFT Method for Electromagnetic Scattering from Inhomogeneous Objects in a Planarly Layered Medium," *IEEE Antennas and Wireless Propagation Letters*, vol. 1, pp. 77-80, 2002.

[48] N. Yuan, T. S. Yeo, X.-C. Nie, and L. W. Li, "A Fast Analysis of Scattering and Radiation of Large Microstrip Antenna Arrays," *IEEE Transactions on Antennas and Propagation*, vol. 51, no. 9, pp. 2218-2226, 2003.

[49] Y. Shi and C.-H. Liang, "Application of the Spatial-Spectral CG-FFT Method for the Solution of Electromagnetic Scattering by Buried Flat Metallic Objects," *IEEE Geoscience and Remote Sensing Letters*, vol. 4, no. 1, 2007.

[50] H.-T. Chou, H.-K. Ho, P. H. Pathak, P. Nepa and O. A. Civi, "Efficient Hybrid Discrete Fourier Transform-Moment Method for Fast Analysis of Large Rectangular Arrays," *IEE Proceedings Microwave Antennas Propagation*, vol. 149, no. 1, 2002.

[51] H.-T. Chou, and H.-K Ho, "Implementation of a Forward-Backward Procedure for the Fast Analysis of Electromagnetic Radiation/Scattering from Two-Dimensional Large Phased Arrays," *IEEE Transactions on Antennas and Propagation*, vol. 52, no. 2, pp. 388-396, 2004.

[52] H.-T. Chou, "Extension of the Forward-Backward Method Using Spectral Acceleration for the Fast Analysis of Large Array Problems," *IEE Proceedings Microwave Antennas Propagation*, vol. 47, no. 3, 2000.

[53] C. S. Heng, and D. Torrungrueng, "Fast Capacitance Extraction for Planar Structures in Free Space Using the Novel Spectral Acceleration Algorithm," *Asia Pacific Microwave Conference*, pp. 1-4, 2005.

[54] H. T. Chou and J. T. Johnson, "Formulation of Forward-Backward Method Using Novel Spectral Acceleration for the Medeling of Scattering from Impedance Rough Surfaces," *IEEE Transactions on Geoscience and Remote Sensing*, vol. 38, no. 1, pp. 605-607, 2000.

[55] D. Torrungrueng, H. T. Chou, and J. T. Johnson, "A Novel Acceleration Algorithm for the Computation of Scattering from Two-Dimensional Large-Scale Perfectly Conducting Random Rough Surfaces with the Forward-Backward Method," *IEEE Transactions on Geoscience and Remote Sensing*, vol. 38, no. 4, pp. 1656-1668, 2000.

[56] D. Torrungrueng and J. T. Johnson, "Numerical Studies of Backscattering Enhancement of Electromagnetic Waves from Two-Dimensional Random Rough Surfaces with the Forward-Backward/Novel Spectral Acceleration Method," *J. Opt. Soc. Am. A*, vol. 18, no. 10, 2001.

[57] M. R. Pino, R. J. Burkholder, and F. Obelleiro, "Spectral Acceleration of the Generalized Forward-Backward Method," *IEEE Transactions on Antennas and Propagation*, vol. 50, no. 6, pp. 785-797, 2002.

[58] C. D. Moss, T. M. Grzegorczyk, H. C. Han, and J. A. Kong, "Forward-Backward Method with Spectral Acceleration for Scattering from Layered Rough Surfaces," *IEEE Transactions on Antennas and Propagation*, vol. 54, no. 3, pp. 1006-1016, 2006.

[59] C. Lertsirimit and D. Torrungrueng, "Fast Capacitance Extraction for Finite Planar Periodic Structures using the Generalized Forward-Backward and Novel Spectral Acceleration Method," *Progress in Electromagnetic Research*, PIER 96, pp. 251-266, 2009.

[60] D. Torrungrueng, "Applications of the Novel Spectral Acceleration (NSA) Algorithm for the Computation of Scattering from Rough Surfaces," Dissertation of the Degree Doctor of Philosophy, Graduate School of The Ohio State University, 2000.

[61] Y. Cengiz and H. Tokat, "Linear Antenna Array Design with Use of Genetic, Memetic and Tabu Search Optimization Algorithms," *Progress In Electromagnetics Research C*, vol. 1, pp. 63-72, 2008.

[62] Supakit Kawdungta, "Genetic Algorithm Optimization of Loop Antenna for Radio Frequency Identification (RFID) System at Low Frequency Band," Master Thesis, King Mongkut's Institute of Technology Ladkrabang, 2008.

[63] J.J. Grefenstette, "Optimization of Control Parameters for Genetic Algorithms," *IEEE Trans. on System, Man and Cybernetics*, vol. 16, no.l, pp.122-128, 1986.

[64] K. F. Man, K. S. Tang and S. Kwong, "Genetic Algorithms : Concepts and Application," *IEEE Trans. on Industrial Electronics*, vol. 43, no.5, pp.519-534, 1996.

[65] G. J. Burke and A. J. Poggio. Numerical Electromagnetics Code (NEC) Method of Moment, Part I-III. Lawrence LiverMore Nat. Lab., Livermore, CA, 1981.

[66] F. Hodjat, and S. A. Hovanessian, "Nonuniformly Spaced Linear and Planar Array Antennas for Sidelobe Reduction," *IEEE Transactions on Industrial Electronics*, vol. AP-26, no. 2, pp.198-204, 1978.

RELATED PUBLICATIONS

[1] Supakit Kawdungta, Chuwong Phongcharoenpanich and Danai Torrungrueng, "An Analysis of Electrically Large Planar Dipole Antenna Arrays with An Efficient Hybrid MSMM/CG Method," *J. of Electromagn. Waves and Appl.*, Vol. 25, pp. 189-202, 2011.

[2] Supakit Kawdungta, Chuwong Phongcharoenpanich and Danai Torrungrueng, "A Novel Analysis of Planar Dipole Antenna Arrays in Free Space with the Multiple-Sweep Method of Moments," *Electromagnetics*, Vol. 31, Issue 4, pp. 258-272, 2011.

[3] Supakit Kawdungta, Chuwong Phongcharoenpanich and Danai Torrungrueng, "The MSMM/SA/GA Design of Non-Uniform Spacing Collinear Dipole Antenna Arrays," *ECTI-CON 2011*, pp. 216-219, May 2011.

[4] Supakit Kawdungta, Chuwong Phongcharoenpanich and Danai Torrungrueng, "The MSMM/GA Design of Non-Uniform Spacing Collinear Dipole Antenna Arrays," *the 2011 IEEE AP-S International Symposium on Antennas and Propagation*, pp. 208-211, 2011.

AUTHOR BIOGRAPHY

Supakit Kawdungta was born in Chaing Mai, North of Thailand. He received B. Eng (First Class Honors) and M. Eng. degrees in Telecommunication Engineering from King Mongkut's Insititute of Technology Ladkrabang (KMITL), Thailand, in 2006 and 2008, respectively. Between 2009 to 2011, he was a Ph.D. student supported by a scholarship from the Commission on Higher Education (CHE) in Thailand and the Thailand Research Fund through The Royal Golden Jubilee (RGJ) program. During the time period between April and September, 2010 he was a visiting scholar in the Ohio State University, Columbus, Ohio, United States of America. His research interests are in the areas of antenna engineering, electromagnetic engineering and microwave engineering.